UNIVERSITÀ DI PISA

DIPARTIMENTO DI INGEGNERIA CHIMICA

CHIMICA INDUSTRIALE E SCIENZA DEI MATERIALI

Ph. D. Candidate in

Ingegneria "Leonardo da Vinci" - Ingegneria Impianti Chimici

ING-IND/25

MATHEMATICAL MODELING OF MASS TRANSFER AND REACTION IN AN INNOVATIVE SOLID OXIDE FUEL CELL

Author: Tengjiao Ou

Supervisor: Prof. Ing. Cristiano Nicolella

Prof. Ing. Nicolaos Vatistas

Academic Year 2008-2010

Abstract

IDEAL-Cell is an innovative concept of a solid oxide fuel cell (SOFC), which is supposed to possess some advantages over conventional SOFCs by building an independent compartment to evacuate water that normally is present either at the anode in ACFCs or at the cathode in PCFCs.

The namely advantages have been demonstrated by thermodynamic analysis in Chapter 1 that IDEAL cell can potentially provide 15% higher Nernst potential than PCFCs and 30% higher Nernst potential than ACFCs at high fuel utilizations. Modelling activities in this innovative fuel cell are mainly concentrated on its peculiar feature: dual membrane which consists of two dense electrolytes and central membrane in the middle. This particular design brings many challenges for describing complex phenomenon of mass transfer and mechanism of ionic recombination reaction, whose understanding requires dedicated experimental and theoretical work.

In this thesis, a series of mathematic models for characterizing mass transfer in dense electrolyte (Chapter 2), mass transfer in porous composite central membrane (Chapter 3), and kinetic reaction in central membrane (Chapter 4) have been built and preliminarily validated by experimental results. These models enable one to theoretically explain electrochemical processes, to indicate technique difficulties confronted in processing and to predict steady-state response of the IDEAL-Cell under varying operating conditions (temperatures and gas atmospheres). In the presence of more effective data to validate and modify, these models are useful to support the design of materials, components and IDEAL-Cell prototype as well.

Keywords: IDEAL-Cell, Central Membrane, Mathematic Modelling, Complex Ionic Conduction, Ionic Recombination Reaction

Contents

Chapter 1 General introduction

1.1 Fuel cell

Fuel Cell is a kind of device which can directly convert chemistry energy of fuels into electricity energy. It is widely expected to be the alternative for the energy supply in the new century due to many advantages could be brought by the application of fuel cell, which is summarized as high efficiency, simplicity, low emissions, and silence. The first demonstration of a fuel cell was by William Grove in 1839, afterwards six types of fuel cells (Figure 1.1) have been developed to approach commercialization during continuous explorations on material processing and equipment manufacture, which are Alkaline Fuel Cell (AFC), Proton Exchange Membrane Fuel Cell (PEMFC), Direct Methanol Fuel Cell (DMFC), Phosphoric Acid Fuel Cell (PAFC), Molten Carbonate Fuel Cell (MCFC) and Solid Oxide Fuel Cell (SOFC). These fuel cells fabricated with different materials and operated under different temperature ranges are able to generate power by stack cell from 1-10MW. Small scale power generator (i.e. DMFC) is suitable for portable electronics equipment such as mobile phone or computers. Medium scale power generators (i.e. AFC and PEMFC) can be applied in the field of transportation vehicles such as cars or boats. The large scale power generators (i.e. MCFC, SOFC and PAFC) are possible to meet the residential demands of electricity. From this point of view, the application ranges of fuel cells to satisfy a variety of needs from domesticity to industry are quite versatile than any other type of energy converter. Nevertheless, some fuel cells have been developed almost maturely and are nearly approaching to market, while some are still remained with crucial difficulties to overcome in the future.

Typical application	Portable electronics equipment			Cars, boats and domestic CHP		Distributed power generation ,CHP, also buses		
Power in Watts	1	10	100	1 k	10 k	100 k	1 M	10 M

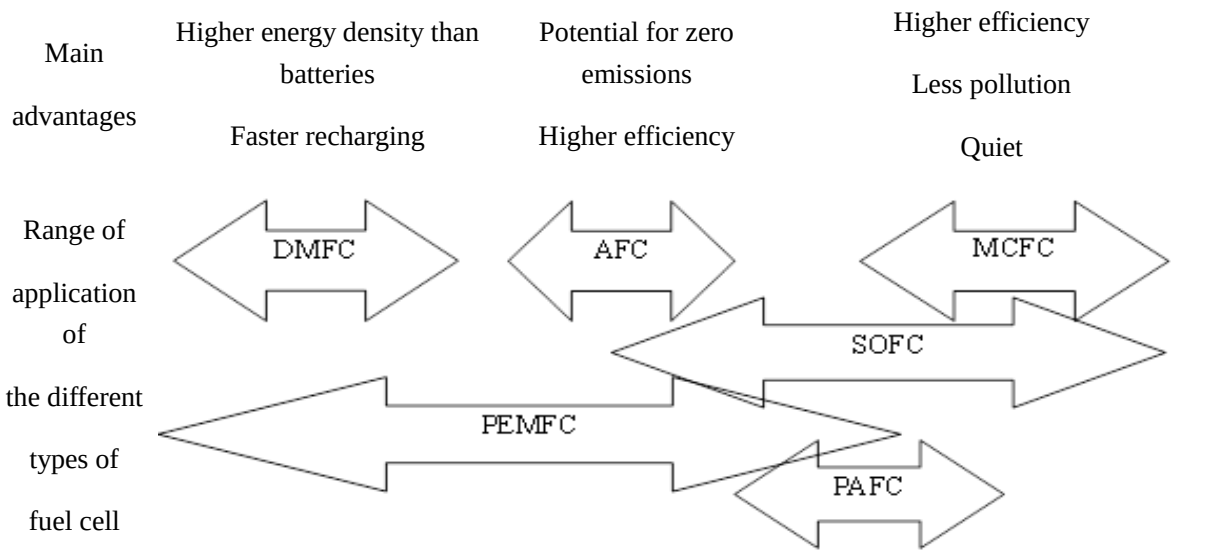

Fig.1.1 Chart to summarize the applications and main advantages of fuel cell [1]

1.2 SOFC

The first SOFC could be traced back in the end of 19th century when Nernst found that solid oxide could also act as electrolyte at high temperature and considerable investigations focused on the SOFC were started from 1980s[2]. The preferable conversion efficiency of SOFC system is 35-50%, if SOFC is combined with Gas Turbine (namely hybrid SOFC-GT system), the efficiency could possibly reach as high as 60-70%. One of benefits of SOFC is that a wide range of fuels can be chosen such as hydrogen, hydroxyl, ammonia[3] and dimethyl ether[4], etc. As development of materials and technologies, fuels can be directly fed into anode to take reaction which is named direct internal reforming SOFC[5]. This kind of fuel supply offers simplest and economic design for SOFC system and in principle provides greatest system efficiency with least loss of energy. The alternative feed pattern is indirect internal reforming[6] which integrates reforming step in SOFC stack upstream of the anode. This feeding pattern although less efficiency, is much easier to control.

Traditional SOFCs usually compose of three compartments: anode, electrolyte and cathode. Electrodes provide the places for reaction such as charge transfer, ionization. While the electrolyte is responsible for transporting charged species from one electrode to the other (see Figure 1.2). The first generation of SOFC system are required to operate around 1000℃ in order to realize the ion conduction in electrolytes which are made of ceramic oxides and perform as insulators at low temperatures and become available medium for ions

conduction above 500℃. During the conductive temperature ranges, the higher temperature generally enables the higher conductivity attributed to lower activation energy of ionic movements in electrolyte. For instance, Yttria– stabilized-zirconia (YSZ) which is a typical oxide ion conducting electrolyte material is able to exhibit the conductivity of 0.02 S/cm at 500℃ and 1.7 S/cm at 900℃[7].

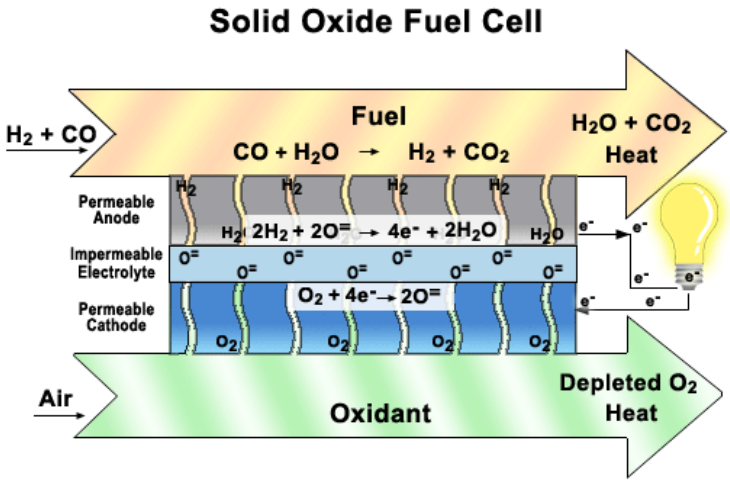

Fig. 1.2 Chart of phenomenon in a typical SOFC operation[8]

Nonetheless, high temperature demanded for running a SOFC system on one hand depletes large quantity of heat supply by equipment set-ups, on the other hand accelerates the aging of materials as well as instruments. Consequently, it inevitably brings the problems of short life SOFC system and also high cost of materials and manufacturing technologies, which are some of the bottlenecks for the commercialization of SOFC. Nowadays, many scientific activities[9, 10] focus on developing more suitable advanced materials, optimizing constitutions and microstructures, designing SOFC cells and stacks for the purpose of bringing down SOFC working temperature to 500-700℃ levels.

1.3 Intermediate temperature SOFC

Intermediate temperature application (500-700℃) indicates to sacrifice system efficiency (especially for oxygen ion conducting SOFC) for long life time and reduced cost of total system[11]. Efforts are mainly spent on searching more advanced materials, designing SOFC concept, etc. No matter what improvements have been made or are going to make, the working mechanism particularly the internal ion transportation are unchangeable, which

only two charged species (protons and oxygen ions) can be conducted in electrolytes. Based on the types of charged species transferred, SOFCs are classified into two basic sorts: the one conducting protons is named protonic conducting SOFC (shorted as PCFC), the other one which is able to transport oxygen anions is given the name of anionic conducting SOFC (shorted as ACFC). The features of these two sorts SOFC are presented in Figure 1.3:

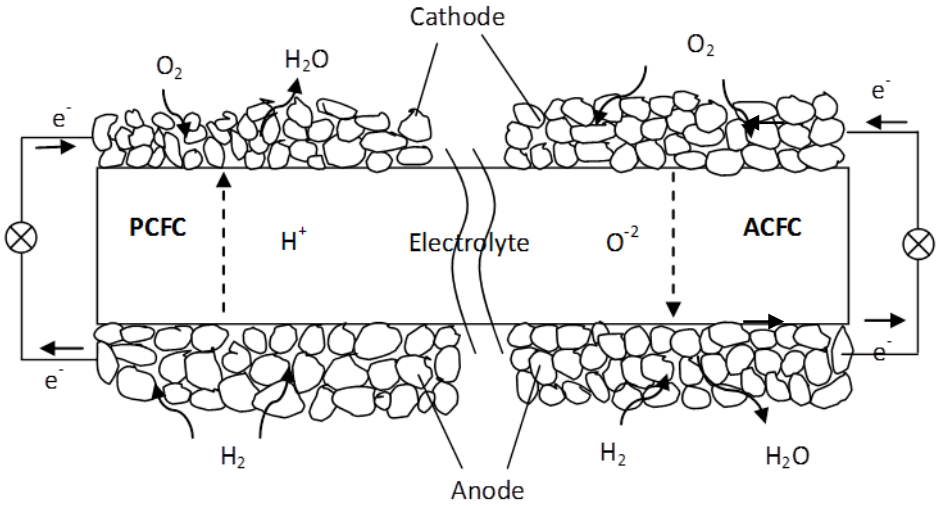

Fig.1.3 Schematic presentation of the features in PCFC (left part) and ACFC (right part)

A few of similarities between PCFC and ACFC can be observed from Figure 1.3. First of all, to form an electrical circuit outside, it is necessary to supply fuel (typically hydrogen) to the anode and oxidant (air or pure oxygen) to the cathode separately. Consequently, charge transfer processes namely as electrode reactions including hydrogen oxidization at anode and oxygen reduction at cathode take place in the meantime. The numbers of species involved in the reaction which are specified in table 1.1.

Table 1.1 Electrode reactions involved in conventional SOFCs

	Anode	Cathode	Overall
PCFC	$H_2 \leftrightarrow 2H^+ + 2e^-$	$2H^+ + \frac{1}{2}O_2 + 2e^- \leftrightarrow H_2O$	$H_2 + \frac{1}{2}O_2 \leftrightarrow H_2O$
ACFC	$H_2 + O^{2-} \leftrightarrow H_2O + 2e^-$	$\frac{1}{2}O_2 + 2e^- \leftrightarrow O^{2-}$	

The ACFCs are more commonly investigated than PCFCs since they have been developed longer and more maturely for decades. Figure 1.4 shows a collection of power densities obtained from PCFCs and ACFCs in range of 500-800℃, which can be seen that ACFCs perform better than PCFCs according to existing developments.

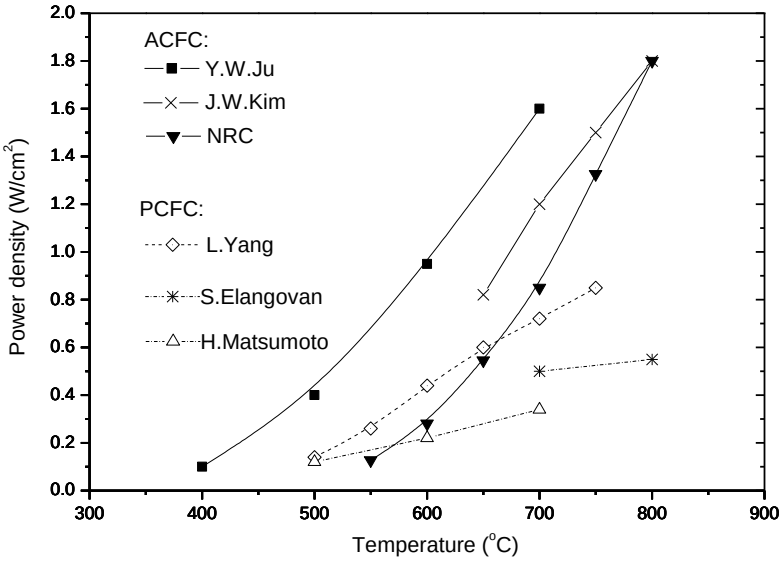

Fig. 1.4 Collection of cell performances of PCFCs and ACFCs [12-17]

The mechanisms of ions conduction in electrolytes are attributed to the oxide defects in structures by doping cations with different valences. The materials used for this kind of electrolytes are normally rare earth doped ceramic oxides, such as notable Yttria Stabilized Zirconia (YSZ [18]), etc. The choices for oxygen ion conducting electrolytes are wider such as fluorite-structure oxides, zirconia- based structure oxides, and ceria based oxides[19] which are developed recently and found to be applicable at intermediate temperatures. The electrons are usually carried by electrodes which are made by different materials compared with electrolyte. And reactants and products in electrode reaction are usually gases, which requires electrode to be made porous. As a consequence, the electrode reaction is believed to take place only at the boundary of electronic conductor (electrode), ionic conductor (electrolyte) and gas diffusion channel (pores), which is noted as three phase boundary (shorted as TPB)[20]. This concept is very important physical parameter for understanding electrode reaction and also chemical reaction in CM which are going to be introduced later.

The SOFCs especially ACFCs are almost approaching to commercialization with some unresolved difficulties such as stability, resistibility to corrosion, and also high price of metal catalysts. Some problems could be resolved by exploring more suitable materials with higher activity and compatibility and by lowering working temperature to intermediate temperature for prolonging the durability. However, some problems like the presence of water at either anode or cathode which brings gas consumption mentioned above and also causes severe corrosion on both electrodes and interconnect are impossible to be avoided at beginning designs of PCFCs and ACFCs, which produce water at cathode and anode separately.

1.4 Proposal of IDEAL cell

In order to solve problem mentioned above, a new conceptual SOFC with special design is proposed by Association de Recherché des écoles des MINES in Paris[21]. In this concept, it is proposed that an anode and the PCFC electrolyte are connected with the ACFC electrolyte and a cathode through a central membrane (shorted as CM) which is composite of proton-conducting and anion-conducting compartment (see Figure 1.5). This new conceptual SOFC is given the name of Innovative Dual Membrane Fuel Cell (abbreviated as IDEAL cell). Among assembled five layers, three of them are supposed to be composite porous layers (e.g. anode, cathode and CM) while two electrolytes are suggested to be dense layers. In a functioning IDEAL cell, protons are formed by electrochemical oxidation of hydrogen at the anode and subsequently migrate through the protonic electrolyte to the CM, where they react with oxygen anions migrated from the cathode through the anionic electrolyte to produce water. The movements of ions are thought to be driven by concentration gradient and potential gradient.

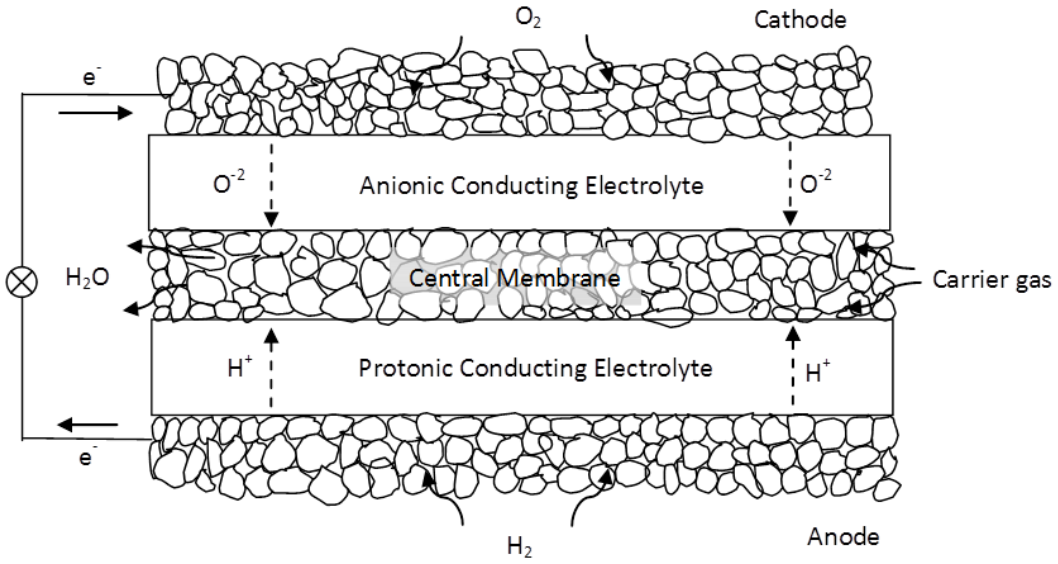

Fig. 1.5 Schematic features of IDEAL cell with five layers

The physical and chemical processes in IDEAL cell are specified in table 1.2, which includes electrochemical charge transfer reactions in electrodes, chemical recombination of charged ions in CM and transportation of ions in dual membrane. Overall reaction remains as same with conventional SOFCs indicating that the Nernst potential of IDEAL cell keeps unchanged at same conditions with conventional SOFCs. The most noticeable feature observed from Figure 1.5 refers to the fact that water cannot permeate dense electrolytes to contact with the fuels at electrodes. As a consequence, the produced water is evacuated by pressure gradient due to accumulation of resultants. The design of water evacuation from independent compartment (CM) makes sure that vapor does not dilute the fuels and does not interfere with the electrochemical activity of catalyst at the electrodes.

Table 1.2 Reactions involved in IDEAL cell

Anode	CM	Cathode	Overall
$H_2 \leftrightarrow 2H^+ + 2e^-$	$2H^+ + O^{2-} \leftrightarrow H_2O$	$\frac{1}{2}O_2 + 2e^- \leftrightarrow O^{2-}$	$H_2 + \frac{1}{2}O_2 \leftrightarrow H_2O$

The IDEAL Cell project proposes an innovative and competitive design of an intermediate temperature SOFC, aiming at operating in the range of 500 - 700 ℃. The concept offers a

new and original approach for enhancement of the power efficiency and performance stability, which cannot be obtained through the existing concepts of SOFCs and stacks. The novel design proposed in the project offers a unique solution to existing problems, which is beyond the state of the art technique. The introduction of three independent chambers for gas evacuations of hydrogen, oxygen and water approximates the fuel cell to an internal combustion engine and thus ensures optimized operating conditions:

1. The fuel is not diluted;
2. Water does not inhibit the catalytic activity of the electrodes;
3. No gas counter-flow is needed to sweep water away from electrodes;
4. No highly corrosive high temperature oxygenized water is produced (as it is at the cathode side of a PCFC system);
5. Every element of the cell plays a singular role, and therefore can be fully optimized for one specific purpose;
6. The oxygen and hydrogen chambers are approximately "closed", which offers the possibility of applying pressure independently on both sides in order to optimize the operating conditions;
7. The heat of the water evaporating from the central membrane is easily recovered via a heat exchange system, since it is not diluted with gases;
8. The highly purified water produced in the central membrane can be re-used for hydrogen production by electrolysis or in a vapor-reforming stage.

1.5 Polarizations

All physical and chemical processes occurred in conventional or non-conventional SOFCs are driven by concentration gradient and potential gradient (interrelated) leading to consumption of driving force which is manifested as voltage losses during cell operation, Voltage losses are namely polarizations, which are the evaluation of cell performances. When the cell is under unpolarized conditions (i.e. open circuit), the driving force could

reach maximum which is well-known as open circuit voltage (OCV) and is relevant with the temperature and concentrations (i.e. pressures) of participants. When the cell is loaded with current, the output voltage starts to drop from OCV due to polarizations taking effect. Three contributions to total polarizations are classified as activation polarization η_{act} in electrodes, ohmic polarization η_{ohm} in electrolyte and concentration polarization η_{conc} in electrodes. The sum of output voltage with total polarizations is equal to Nernst potential.

$$E = V(i) + \eta(i) \tag{1.1}$$

$$\eta(i) = \eta_{act}(i) + \eta_{ohm}(i) + \eta_{conc}(i) \tag{1.2}$$

Where E is the Nernst voltage of cell calculated by Nernst equation 1.3, and presented in Figure 1.6 (drawn by blue dashed line), all polarizations are relevant with current densities. Normally, higher current density gives rise to higher polarizations of all contributions. When current density approaches to zero, total polarization is null, output cell voltage $V(0)$ equals to OCV, which can be calculated by Nernst equation 1.3:

$$E = \frac{-\Delta G^0}{2F} + \frac{R_g T}{2F} \ln\left(\frac{p_{H_2} p_{O_2}^{1/2}}{p_{H_2O}}\right) \tag{1.3}$$

Where ΔG^0 is the Gibbs free energy of overall reaction at temperature T and standard pressure conditions, in addition, Nernst potential is also a function of temperature and partial pressure of hydrogen, oxygen and water. OCV is the theoretical cell voltage estimated without any electrochemical reaction occurring. While Nernst potential refers to the theoretical output cell potential if the cell is under reversible conditions. However, for a real operating SOFC, the partial pressure of all gases vary along the flowing channel, which indicates that real Nernst potential should also be variable along with gas flow.

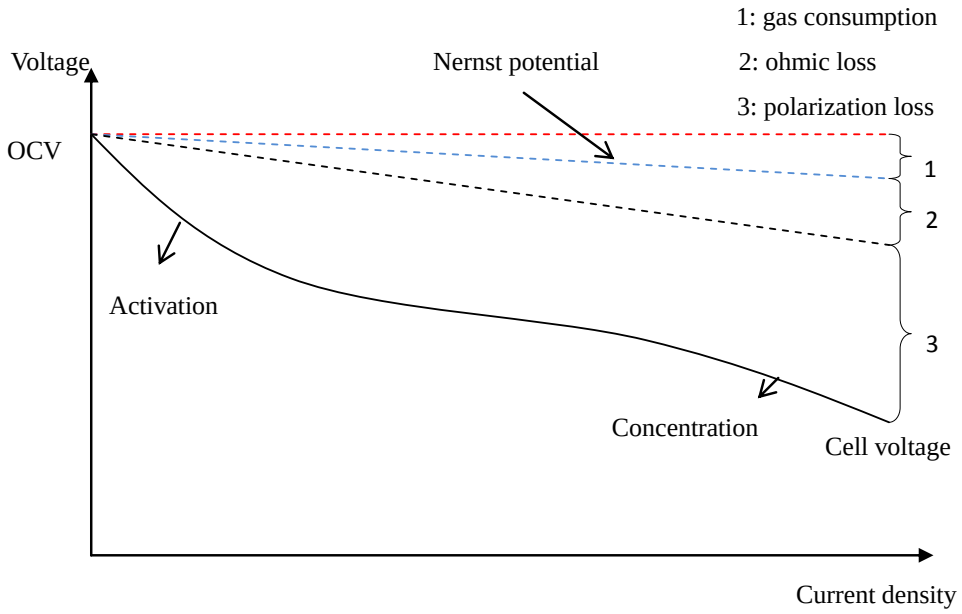

Fig. 1.6 Typical voltage profile as a function of current density of SOFC obtained from reference[2]

The factors of three contributing polarizations can be summarized as: materials, morphology, temperature, atmosphere and current density, which play a different role in the different extent current densities and are featured in Figure 1.6. When at small current density, cell voltage loss is mainly controlled by activation polarizations. The drop of voltage is proportional to current density. In the media scale of current density, voltage drop turns into mild, which is dominated by Ohmic polarization. When current density goes to large scale, concentration polarization becomes significant in the total polarizing contribution. The difference between theoretical OCV with Nernst potential $E_{OCV} - E_{\text{Nernst}}$ is viewed as gas composition due to the influence of mixed flow either at cathode of PCFC or at anode of ACFC, which is mainly due to dilution of feeding inert gases and produced water. This part of contribution cannot be ignorable at high current density and must be accounted for the overall polarizations.

1.6 Thermodynamic analysis

Many researchers claimed that PCFCs could potentially perform better than ACFCs under similar operating conditions (temperature and gas composition). For instances, M. Ni[22] found that at a fuel utilization of 80% and an oxygen utilization of 20%, the efficiency of ammonia fed PCFC was 11% higher than that of ACFC at 800℃. The efficiency difference

between PCFC and ACFC becomes more significant at higher fuel utilizations and higher temperatures. W. Jamsak[23] investigated the SOFCs with C_2H_5OH / H_2O fed as fuel and found that the maximum efficiency of ACFC was limited by the ratio of C_2H_5OH / H_2O which was also the limit for carbon formation. However, the maximum efficiency of PCFC showed no limitation of that. He concluded that, at the temperature range of 700-900℃ and optimum conditions, PCFC was the more promising SOFC system. A.Demin[24] applied wet hydrogen as fuel during 700 and 1000℃ and concluded that the maximum efficiency of PCFC could exceed 80% which was significant higher than ACFC. The mixture H_2/CH_4 fed as fuel was also studied by A.K. Demin[25]. The results revealed that the maximum efficiency of PCFC was around 15% higher than that of ACFC under 600-1000℃ as the mole ratio of H_2/CH_4 reached 2.6.

The possible explanations for PCFCs which are claimed to be theoretically more promising than ACFCs, on one hand are due to the fact that protons are the smallest charges to easily jump between oxides in the lattice, or in other word, mobility of proton is higher than oxygen ion. On the other hand, the overall reaction stoichiometrically requires twice moles of hydrogen with one mole oxygen. From this standpoint of view, the dilution at anode takes more negative effects than the dilution at cathode. The progress beyond the state of the art in IDEAL Cell is essentially linked to a significant increase in fuel cell power efficiency by isolating water from electrodes. To prove this viewpoint, thermodynamic analysis is applied, which is the useful tool to predict SOFC system efficiency by concerning only the concentrations or partial pressures of reactants and temperatures [22, 24-26].

In this analysis, the cell efficiency and Nernst cell voltage calculated on PCFC, ACFC and IDEAL cell are taken to compare simultaneously. The operating temperature is chosen between 500-700℃ which are the desirable temperature ranges for the future SOFC developments. Total pressures of fuels (system pressure) can vary from atmosphere to several bars. The SOFC system efficiency is introduced as combination of three contributing parts which are expressed in equation 1.4-1.17:

$$\varepsilon_{cell} = \varepsilon_R \varepsilon_V \varepsilon_U \tag{1.4}$$

$$\varepsilon_R = \frac{\Delta G}{\Delta H^0} \tag{1.5}$$

$$\varepsilon_V = \frac{E_{cell}}{E_{rev}} \tag{1.6}$$

$$\varepsilon_U = 1 - \frac{\sum x_i^{out} m_i^{out}}{\sum x_i^{in} m_i^{in}} \tag{1.7}$$

Where ε_{cell} is the cell system efficiency, ε_R is the reversible efficiency depending on the temperature and species that applied, ε_V is the voltage efficiency related with the composition of fuels and mass flow rates, ε_U is the fuel utilization (some papers refer as U_f). The definition of fuel utilization is the ratio of the amount of consumed hydrogen with the amount of fed hydrogen, which can be expressed by the mass flow rate of hydrogen between inlet and outlet of channel (equation 1.7). If the system pressure is fixed at 1 atm, the ε_U could be simplified as a function of partial pressure in equation 1.8 for PCFC and equation 1.9 for ACFC:

PCFC: $$\varepsilon_U = \frac{P_{H_2,in} - P_{H_2,out}}{P_{H_2,in}(1 - P_{H_2,out})} \tag{1.8}$$

ACFC: $$\varepsilon_U = \frac{P_{H_2,in} - P_{H_2,out}}{P_{H_2,in}(1 + P_{H_2,out})} \tag{1.9}$$

IDEAL cell: $$\varepsilon_U = \frac{p_{H_2,in} - p_{H_2,out}}{p_{H_2,in}(1 - p_{H_2,out})} \tag{1.10}$$

From these definitions, it is not difficult to estimate PCFC as well as IDEAL cell could provide higher fuel utilization than ACFC at same outlet hydrogen pressure, the relationship of which is drawn in Figure 1.7. The fuel utilization of ACFC approaches 1 only when outlet hydrogen partial pressure is all consumed. While in case of PCFC and IDEAL cell, even hydrogen partial pressure is 0.9 atm, 70% fuel utilization indicates most of hydrogen have participated in reaction. If the fuel utilization is kept at 100% and the cell voltage lies

at ideal conditions (reversible conditions), the maximum cell efficiency (equation 1.4) can be written as:

$$\varepsilon_{\max} = \varepsilon_R \varepsilon_V \varepsilon_U = \frac{\Delta G}{\Delta H^0} \times 1 \times 1 = \frac{\Delta G^0 - R_g T \ln(p_{H_2} p_{O_2}^{1/2} / p_{H_2O})}{\Delta H^0} \quad (1.11)$$

Where R_g is gas constant, F is faraday constant, ΔH^0 is the lower heating value of fuel at standard conditions (-285.8 kJ/mol), ΔG^0 is the free Gibbs energy of overall reaction at temperature T and standard pressures, the values of which are listed in table 1.3.

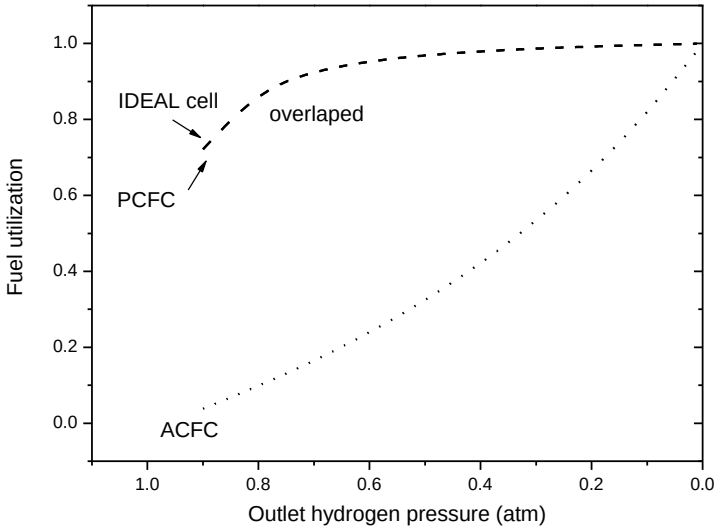

Fig. 1.7 Fuel utilization against outlet hydrogen partial pressure

Table 1.3 Thermodynamic data[27] of participants in overall reaction at standard pressure

Species	G (kJ/mol, 500℃)	G (kJ/mol, 600℃)	G (kJ/mol, 700℃)
H_2	-108.4	-124.3	-140.8
O_2	-166.4	-190.1	-214.1
H_2O	-402.4	-425.4	-449.0
G^0	-210.8	-206.0	-201.2

In the calculation of maximum efficiency, the fuel utilization is taken with 99% (100% value makes the second term of Nernst equation divergent). In addition, the maximum

efficiency of heat engine is also taken to compare with SOFCs in the extended temperature ranges. The calculation of efficiency heat engine is by method of Carlo cycle:

$$\varepsilon_T = \frac{T_{high} - T_{low}}{T_{high}} \tag{1.12}$$

As long as those factors are ascertained, the maximum SOFC efficiency that could be theoretically reached are possible to be derived in Figure 1.8, the comparison of SOFCs with heat engine shows that the differences of maximum efficiencies among three SOFCs are slight because 99% fuel utilization lessen the effects of dilution. It is found above 800℃ SOFCs are inferior than heat engine indicating SOFCs, from efficiency point of view, are only competitive with heat engine at the intermediate temperature ranges or even lower temperatures.

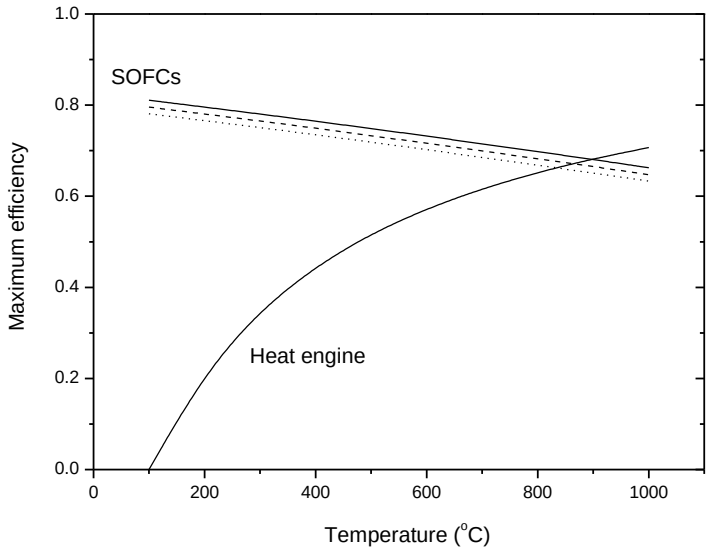

Fig. 1.8 Theoretical maximum efficiency of heat engine plus SOFCs at 99% fuel utilization, line: IDEAL cell, dashed line: PCFC, dotted line: ACFC

The type of gas flow within channel can be classified into two ideal types, plug flow and mixed flow. The former is characterized by the fact that the gas mixture moves orderly through the channel with no element of the gas mixing with any other element ahead or behind, whereas with mixed flow the contents are well-mixed and uniform throughout. In

the plug flow mode, the average electromotive force changes along the SOFC channel due to the changes of gas composition in both anode and cathode sections. Most typical SOFCs are operated under a condition close to the plug flow mode. It is proved that plug flow mode provides more efficient SOFC that mixed flow mode which although can be realized by using a high recycle process. For the sake of simplicity, the calculation of Nernst potential of SOFCs only considers hydrogen as fed fuel and pure oxygen as oxidant. The gases flows are treated with mixed flow which assumes that gases reach equilibrium composition along flowing. The Nernst cell potentials are calculated by equation 1.3 and results are presented in Figure 1.9.

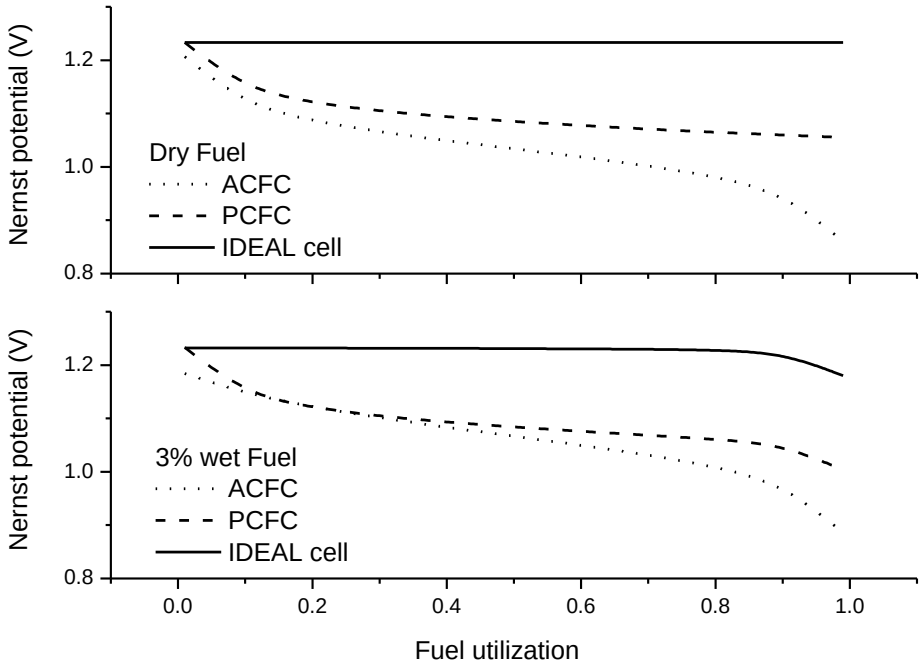

Fig. 1.9 Comparison of 3 SOFCs: Nernst potential at 600℃ against fuel utilization

The results clearly show that three SOFCs start from same OCVs at 0% fuel utilization. When fuel utilization rises, the Nernst potentials of PFCF and ACFC reduce rapidly during 20% fuel utilizations. As ε_U is superior to 20%-90%, PCFC slowly descends while ACFC continues to drop although in smaller slope compared with the one in range of 0-20% fuel utilizations. This is the proof that many researchers claim PCFC could be more efficient than ACFC. In all range of fuel utilizations, the Nernst potential of IDEAL cell remains the

unchanged in dry fuel fed situation and appears a slight decadence in wet fuel fed situation, which based on this thermodynamic consideration proposes IDEAL cell could be most efficient in SOFC systems. This calculation results also reminds us the advantages of IDEAL cell can be embodied at high fuel utilizations, where IDEAL cell is supposed to provide 0.2V more than PCFC and almost 0.4V than ACFC.

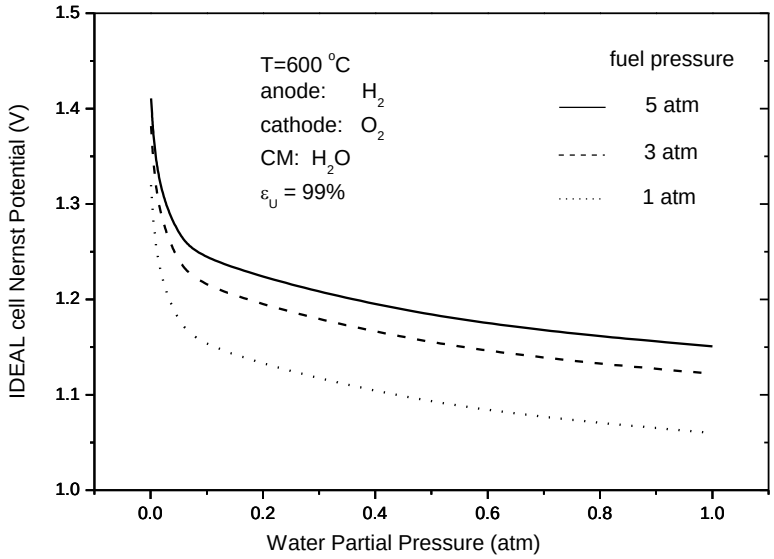

Fig. 1.10 Cell Nernst potential under water partial pressure in CM of IDEAL cell

In this calculation, the water pressure in CM is set to be 0.01 atm. This is one of the benefits from IDEAL cell concept which builds an independent compartment for evacuating water and makes it possible to manipulate the partial pressure of water. Under this acknowledge, the Nernst potential of IDEAL cell is governable in some extent by controlling the water pressure, the relation of which is presented in Figure 1.10. When the pressure of water is less than 0.1atm, Nernst potential increases dramatically. This rapid rise could give us the hints that lower CM pressure helps to obtain larger output potential and is also in favor of producing water.

1.7 Modeling Objective and Strategy

Above discussions on the advantages of IDEAL cell give the significance of this research. In the progress of IDEAL cell project, we are responsible for the theoretical modeling

descriptions and providing instructions for cell design. The main tasks of modeling work are to study the nature of phenomenon and correspondingly to offer reasonable explanations and above all to provide reliable prediction on the cell or stack performances. In detail, the emphasis of scientific activities in this thesis is on following:

i. Calculations of mass transfer (e.g. electrolyte conductivities, CM effective conductivities, water evacuation)

ii. Kinetic description of (electro-)chemical reactions (e.g. hydrogen oxidization at anode, oxygen reduction at cathode, water combination in CM)

iii. Cell design support(e.g. geometry, morphology)

The mentioned modeling activities stretch different approaches from surface level, electrode level to cell level. Surface level modeling is mainly to study elementary kinetics of (electro-) chemical reaction with resolution of chemistry into elementary step reactions coupling to continuum models of transport processes. Take the typical oxygen reduction for instance, the overall reaction $2H^+ + O^{2-} = H_2O(g)$ may be divided into 4 possible steps as depicted in Figure 1.11. The one of them may be the controlling step which is the key to be found and to be optimized.

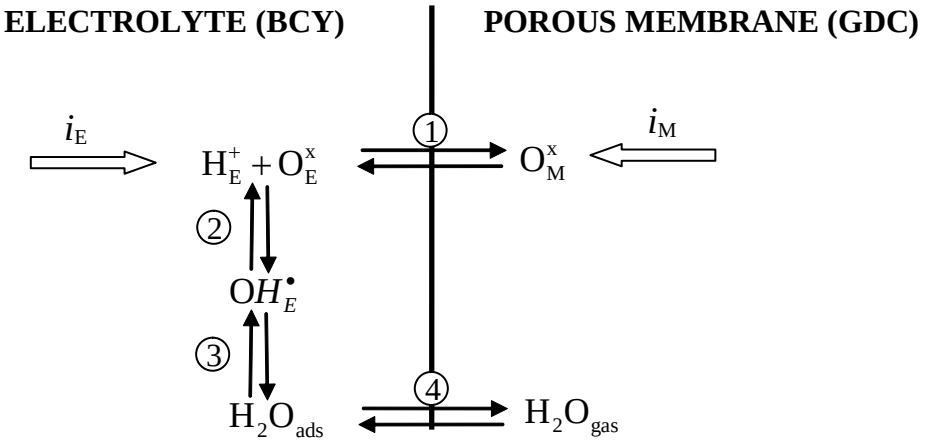

Fig. 1.11 Elementary steps of reaction at interface between electrolyte and cathode, picture is abstracted from C.Nicolella[28]

Electrode level modeling is applied to investigate morphology (2D and 3D) of membranes (e.g. electrodes, CM). 3D morphology is more complicate usually requires assistance from professional software. The simpler method is to build a 2D morphology (Figure 1.12) by empirical model based on assumptions. By understanding the effect of morphology on membrane properties (e.g. effect conductivity), it helps us to design a desirable membrane.

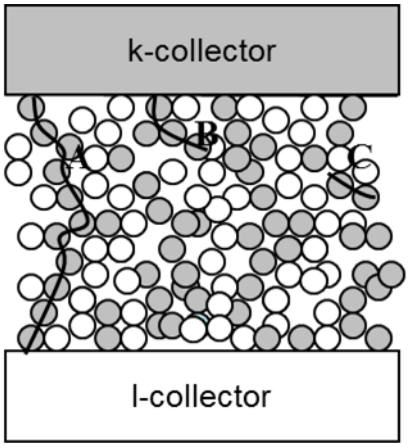

Fig. 1.12 A two dimensional picture of morphology of typical composite porous membrane, picture is abstracted from B.Antonio[29]

Cell level modeling treats IDEAL-Cell layers as continuum media and concerns general electrochemical description on basis of mass, charge and energy balances across the IDEAL-Cell by using effective properties (materials, kinetics, and transport) linked to morphology. For example, the way of mass transportation in CM of charged species (protons and oxygen ions) are thought to be straight pathways (see Figure 1.13) and the reaction possible occur throughout the whole flowing paths. This assumption requires accurate effective properties to acquire descriptions close to reality.

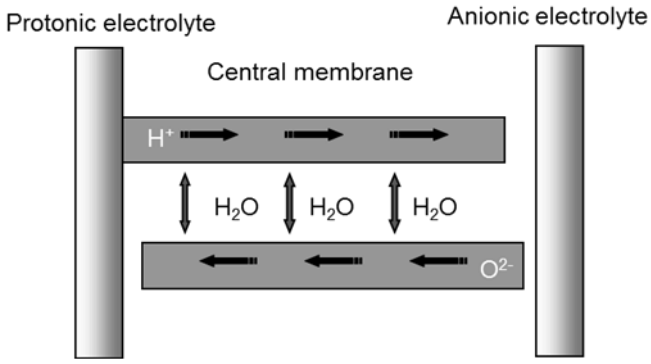

Fig. 1.13 Continuum media treatments in cell level modeling

No matter what kind of model is applied, variables concerned with are nothing more than current, potential, mass flow conditions temperature, gas composition, partial pressure. These variables are correlated with individual sample or measurement to integrate and to validate the relations between conditions and properties, which in return will help us to optimize and design those conditions.

1.8 Conclusions

In this chapter, a detailed introduction on the background of this modeling work has been made. To prove the original attempts of designing IDEAL cell, thermodynamic analysis has been done to demonstrate the effect of dilution on the Nernst potential. The result of calculation state that IDEAL cell is potentially best among three kinds of SOFCs. At the intermediate temperature ranges and high fuel utilizations, IDEAL cell could provide the Nernst potential 15% higher than PCFC, which is expected to output the Nernst potential 15% higher than ACFC as well. To take advantages of benefits of IDEAL cell, it is advised to operate IDEAL cell under high fuel utilization and low partial pressure of water in CM, and if possible, to employ high system pressure.

However, thermodynamic investigations mentioned above are only an ideal and theoretical way to predict potential performance of SOFCs. The results of analysis may provide us a general vision on existing and conceptual SOFCs. The common polarizations such as Ohm polarization and activation polarization take primary effect when it comes to the choice of materials, morphologies and geometries of SOFCs. Since ACFCs have been developed much longer and more maturely than PCFCs[30], it is not surprising that ACFCs exhibit more powerful performances than PCFCs from current developments.

IDEAL cell is a complex system which is expected to minimize the gas consumption at cost of adding two extra layers. The risk exists and it is worth exploring for scientific attempts. The tasks of this thesis are to provide as reliable explanations as possible to a variety of phenomenon and to make reasonable prediction and practical suggestions for fabricating IDEAL cell.

References

1. James Larminie, A.D., *Fuel Cell Systems Explained*. Second Edition ed. 2003: WILEY.
2. Singhal, S.C. and K. Kendall, *High temperature solid oxide fuel cells : fundamentals, design, and applications*. 2003, Oxford ; New York: Elsevier. xvi, 405.
3. Adam Wojcik, H.M., Ioannis Damopoulos, et al, *Ammonia as a fuel in solid oxide fuel cells.* Journal of Power Sources, 2003. **118**(1-2): p. 342-348.
4. A. Tatemi, S.W., T. Ishihara, H. Nishiguchi, and Y. Takita, in *The Electrochemical Society Proceedings*, S.C.S.a.M. Dokiya, Editor. 2003: Pennington. p. 1260.
5. Dicks, A.L., *Hydrogen generation from natural gas for the fuel cell systems of tomorrow.* Journal of Power Sources, 1996. **61**(1-2): p. 113-124.
6. Laosiripojana, N. and S. Assabumrungrat, *Catalytic steam reforming of dimethyl ether (DME) over high surface area Ce-ZrO_2 at SOFC temperature: The possible use of DME in indirect internal reforming operation (IIR-SOFC).* Applied Catalysis A: General, 2007. **320**: p. 105-113.
7. Carpanese, M.P., *Electrochemical Investigation of Composite Cathodes for SOFCs: Experimental and Theoretical Study*. 2008, UNIVERSITY OF GENOVA: Genova.
8. Available from: http://www.nasa.gov/.
9. Bert Rietveld, F.v.B., Ye Zhang Steenwinkel, et al. *The integrated project SOFC600 development of low temperature SOFC*. in *ECS Transactions*. 2009. Vienna.
10. Available from: www.hfpeurope.org.
11. Huijsmans, J.P.P., F.P.F. van Berkel, and G.M. Christie, *Intermediate temperature SOFC - a promise for the 21st century.* Journal of Power Sources, 1998. **71**(1-2): p. 107-110.
12. Elangovan, S., et al., *Planar solid oxide fuel cell integrated system technology development.* Journal of Power Sources, 1998. **71**(1-2): p. 354-360.
13. Kim, J.W., et al., *Polarization effects in intermediate temperature, anode-supported solid oxide fuel cells.* Journal of the Electrochemical Society, 1999. **146**(1): p. 69-78.
14. Lei Yang, C.Z., Shizhong Wang, et, al, *A Novel Composite Cathode for Low-Temperature SOFCs Based on Oxide Proton Conductors.* Adanced Materials, 2008. **20**(17).

15. Matsumoto, H., et al., *Intermediate-temperature solid oxide fuel cells using perovskite-type oxide based on barium cerate.* Solid State Ionics, 2008. **179**(27-32): p. 1486-1489.

16. Available from: http://www.nrc-cnrc.gc.ca/eng/programs/ifci/ high temperature fuel cells /latest-developments.html.

17. Y.W.Ju, H.E., T.Inagaki, T.Ishihara, *High Power SOFC Using LSGM Film on NiFe Porous Bi-metal Substrate,* in *ECS Transactions*, H.Y. S.C.Singhal, Editor. 2009: Vienna.

18. Barnett, S.A., *A new solid oxide fuel cell design based on thin film electrolytes.* Energy, 1990. **15**(1): p. 1-9.

19. H.L.Tuller, A.S.N., journal of electrochemical society, 1975. **122**: p. 255.

20. T. Kenjo, S.O., K. Fujikawa., journal of electrochemical society, 1991. **138**: p. 349.

21. 2008; Available from: http://www.ideal-cell.eu/content/index.php.

22. Meng Ni, D.Y.C.L., Michael K.H. Leung, *Thermodynamic analysis of ammonia fed solid oxide fuel cells: Comparison between proton-conducting electrolyte and oxygen ion-conducting electrolyte.* Journal of Power Sources, 2008. **183**: p. 682-686.

23. W. Jamsak, S.A., P.L. Douglas, et al, *Theoretical performance analysis of ethanol-fuelled solid oxide fuel cells with different electrolytes.* Chemical Engineering Journal, 2006. **119**: p. 11-18.

24. Anatoly Demin, P.T., *Thermodynamic analysis of a hydrogen fed solid oxide fuel cell based on a proton conductor.* International Journal of Hydrogen Energy, 2001. **26**: p. 1103-1108.

25. A.K. Demin, P.E.T., V.A. Sobyanin,et al., *Thermodynamic analysis of a methane fed SOFC system based on a protonic conductor.* Solid State Ionics, 2002. **152-153**: p. 555-560.

26. Zhu, H., *Thermodynamics of SOFC efficiency and fuel utilization as functions of fuel mixtures and operating conditions.* Journal of Power Sources, 2006. **161**: p. 957–964.

27. Available from: http://www.sandia.gov/HiTempThermo/.

28. Cristiano Nicolella, N.V., Wolfgang G. Bessler, *A mathematical model of mass and charge transport and reaction in the central membrane of the IDEAL-Cell*. 2009, Pisa University: Pisa.

29. Bertei, A., *MATHEMATICAL MODELLING OF AN INNOVATIVE SOLID OXIDE FUEL CELL*, in *Faculty of Engineering*. 2009, University of Pisa: Pisa.

30. W. Jamsak, S.A., P.L. Douglas, et al, *Performance of ethanol-fuelled solid oxide fuel cells: Proton and oxygen ion conductors.* Chemical Engineering Journal, 2007. **133**: p. 187-194.

Chapter 2 Mathematic modeling of dual membrane: Part 1 conductivities

As introduced in Chapter 1, the IDEAL cell functionally consists of five layers which are anode, PCFC electrolyte, ACFC electrolyte, cathode, and above all central membrane sandwiched in the middle. The characteristic two electrolytes plus central membrane are namely dual membrane which is supposed to play a key role on performances of this novel SOFC. To interpret working principal of dual membrane, it is necessary to understand unique features of this dual membrane compared to PCFCs and ACFCs, which are summarized as:

1) The dual membrane is responsible not only for transporting charged species as electrolyte does, but also for reaction and water evacuation. This complex phenomenon requires extensive comprehensions and descriptions.

2) The existence of five layers compared to three layers of conventional SOFCs increases technological difficulties for material preparation and layers sintering with high adhesion and compatibility. Although the reaction layer (i.e. central membrane) is proposed to be composition of two dense electrolytes, the presences of pores and water pressures inside central membrane bring about uncertainties in real operations.

3) The mechanism of ionic combination reaction (proton and oxygen ion) at solid phase and high temperature has never been studied in any other fields so far. Although the combination of two reverse electrical charges is supposed to be fast and exothermic process, the overall process involving the mass transfers of three species (proton, oxygen ion and water) are actually linked to the properties of PCFC electrolyte and ACFC electrolyte, respectively.

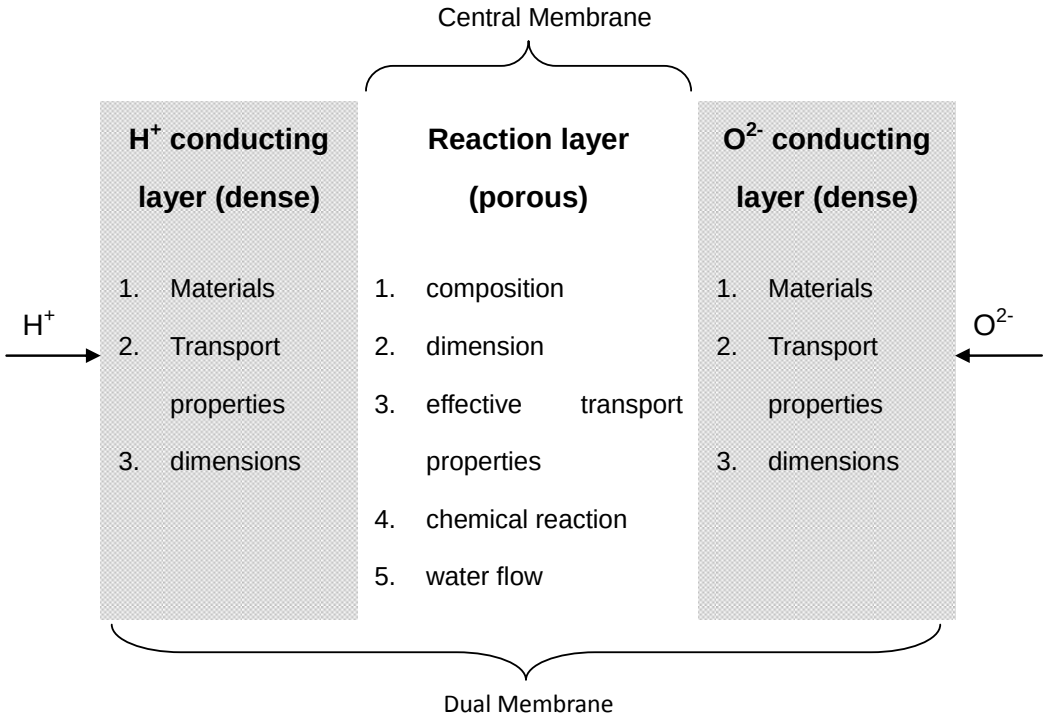

Fig. 2.1 Highlights of scientific activities on dual membrane

Above all, material properties are prerequisites for understanding phenomenon occurring in dual membrane. The highlights of our modeling activities are presented in Figure 2.1 which includes material selection and theoretical description of transport properties influenced by temperature and atmospheres. Although the effects of extended range of temperatures have been studied by other researchers, the latter one (atmosphere) on the proton conducting materials is more complicated than thought and the peculiar working atmosphere (between wet hydrogen and water) has never been investigated before. Finally, transport properties could give us the hints for fabricating duel membrane with suitable dimensions.

2.1. Materials

2.1.1. PCFC membrane

The first discovery of proton existing in some oxides as minority charges was traced to 1960s when researchers originated to study the oxide ion conductivity. However, the proton conductivity was rather small without intriguing too much attention. Until the perovskite oxides were found by Iwahara [1] to have high proton conductivity under some conditions in 1980s, proton conductors as electrolytes for SOFC have been paid more and more

attentions. More systematic work on the proton conducting oxides has been done by Kreuer[2] who analyzed by theoretical calculations on proton conducting materials varying from polymers to ceramic oxides between low temperature (200℃) and extended high temperature (1800℃) under humidified atmosphere. It was found that aliovalent-doped perovskites (ABO_3), such as $BaZrO_3$, $BaCeO_3$, $BaThO_3$, and $SrCeO_3$ exhibiting highest proton conductivities between 0.01 ～ 0.03 S/cm during intermediate temperature (500-1000℃) among other oxides, which seem very promising candidates for IDEAL cell applications.

In the case of aliovalent-doped perovskites ABO_3, the dopant C with low valence is added to substitute B to create oxygen ion vacancies ($V_O^{\cdot}$) in the bulk of perovskite structure, which is written as $AB_{1-x}C_xO_{3-\delta}$. Normally, the valence of A could be from 1 to 3, which decides that the valence of B varies from 3 to 5. The conductivity of material (written in Arrhenius equation 2.1) is as the function of temperature and activation energy E_a of proton transport.

$$\sigma = \frac{\sigma^0}{T} e^{-\frac{E_a}{RT}} \tag{2.1}$$

Where σ^0 is the standard conductivity at standard temperature T^0, T is working temperature and R is Avogadro constant. Lower temperature and smaller values of E_a benefit the movement of protons in lattice as a result of high conductivities. The physical meaning of this activation energy is the electrostatic repulsion between protons and B ions which are correlated with both base materials and doping elements. Generally speaking, the activation energy E_a of ideal cubic perovskites follows A(ⅢB(ⅢO$_3$ < A(ⅡB(ⅣO$_3$ < A(ⅠB(ⅤO$_3$ [3] and doping radii of elements. However, few A(Ⅲ)B(Ⅲ)O_3 materials have a perovskite structure. And the activation energy E_a resulting from doping elements is found to be much more complicated than previous thoughts which has been explained by Kreuer[2]. In sum, the understanding of this gives us the directions for searching suitable candidates of materials. A collection of available data from references has been presented in Figure 2.2 to compare the proton conductivities of barium cerate doping with Y, Nd, Gd, Ln and Ca respectively in the range of 500-900℃[4-8].

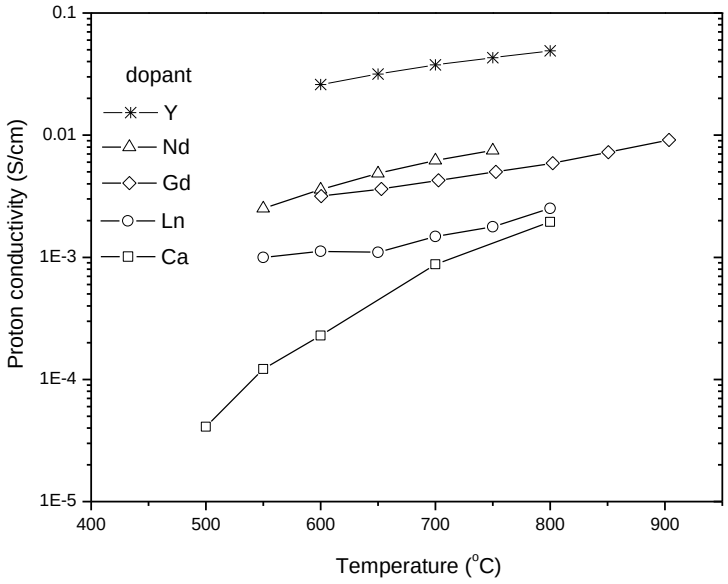

Fig. 2.2 Proton conductivities of doped $BaCeO_3$ in ranges of 500-900℃

As observed, Yttrium-doped $BaCeO_3$ presents highest proton conductivities among perovskites oxides at same temperatures. Since the target of future SOFC applicable temperatures is oriented to 500-800℃, in the scope of IDEAL cell project, the attentions are only paid on the material performances during these temperature ranges. Furthermore, mature preparation technology of doped material is preferable to realize IDEAL cell design. To fulfill these requirements, common perovskite compound $BaCeO_3$ based material seems very attractive due to higher proton conductivity than other oxides. Although it is reported [9-12] that $BaCeO_3$ decomposes in the presence of acidic gases (CO_2, SO_3) and below 800℃, the problem does not exist in the concept of IDEAL cell, which is under operation with only hydrogen, oxygen and small amount of vapor produced in CM. Therefore, Yttrium doped $BaCeO_3$ (shorted as BCY) is selected as PCFC membrane.

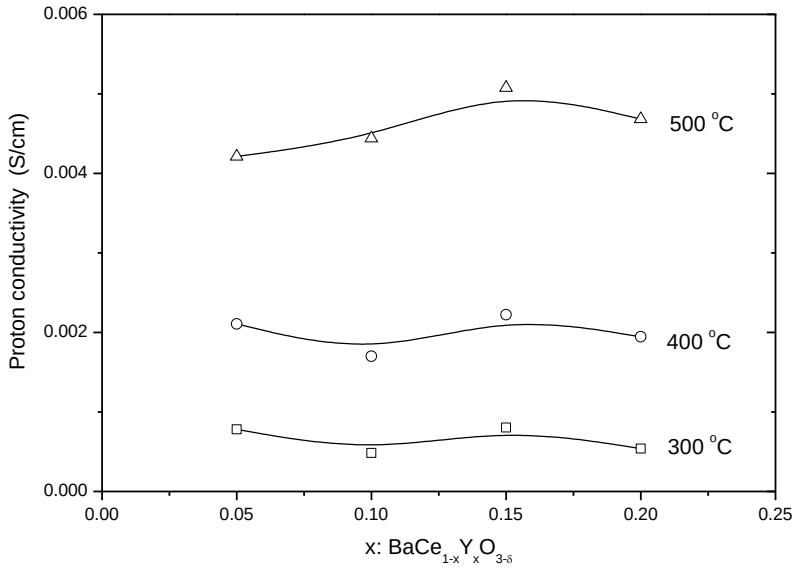

(a)

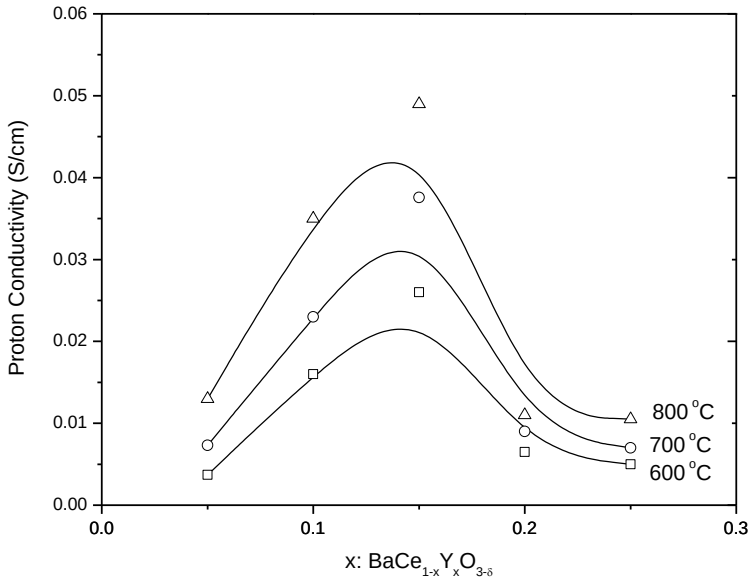

(b)

Fig. 2.3 Proton conductivities of BCY as a function of yttrium doping concentrations at (a)low temperature [13] and (b)intermediate temperature [14-18]

In addition to the effects of doping elements, the doped level (namely dopant concentration) also is the crux for material selection. The doped element introduces oxygen vacancy which plays a critical role in both proton conduction and oxygen ion conduction. The micro scale explanations to the dopant effect can be found in some references [3, 19, 20]. Here, we only rearranged a series of available results of proton conductivities measured on BCY by

different doping level from zero to 25% mole fraction which is presented in Figure 2.3. The conductivities of BCY between 300-500℃(Figure 2.3a) were from one sample while the values of BCY between 600-800℃(Figure 2.3b) were taken from several samples. However, the tendency of proton conductivity varies with dopant concentration is almost equivalent, in which highest proton conductivity of BCY appears at around 10-20% dopant concentration level. In a word, 10-20% mole fraction of yttrium doped $BaCeO_3$ is selected as PCFC membrane during the first stage investigations.

2.1.2. ACFC membrane

Zirconia-based materials were firstly discovered in ACFC application by the end of 19^{th} century. Since then, large scales of attentions have been paid to search new materials and improve their performances. For instance, Yttrium stabilized zirconia (YSZ) which has been intensively studied in the past decades can perform a conductivity of 0.14 S/cm at 1000℃ and 0.006 S/cm at 600℃[21]. After almost one hundred years' exploitation, Extended materials[22] have been developed as oxide ion conducting electrolyte so far for ACFC. It was found that YSZ is only the best oxide ion conductor above 1000℃. When temperature comes to 600 and 800℃, bismuth oxide composition emerges one order higher electrical conductivity than YSZ. But the problem is the non-ignorable electronic conduction contributing to total conduction. Rare earth (RE)-doped ceria are also another type of fluorite structure oxides which are considered to be best candidates in the range of intermediate temperature [23]. Pure ceria oxide has very low ionic conductivity, when it is introduced by appropriate amount of rare earth element, the structure of oxide lattice changes corresponding to the improvement of conductivity of compound. G.B.Balazs [24] studied the ionic conductivities in air of ceria doped with 10% mole rare earth oxides (Sc, Eu, La, Nd, Pr, Gd, Sm, Yb, Dy, Lu, Ho, Er, Tm, Tb, Y). The best performances were found by doping with Sm, Gd, and Y. M. Dudek [25] investigated the electrical conductivities of CeO_2 based electrolytes to exhibit 0.003～0.008 S/cm at 600℃ and 0.02～0.05 S/cm at 700℃. In addition to the fluorite structure oxides, there are other type oxides such as perovskite structure oxides suggested to be attractive candidate for SOFC applications. For example, $LaGaO_3$ based material[26] exhibits the maximum oxide ion conductivity of 0.13

S/cm at 700℃ and 0.04 S/cm at 600℃ which is higher than the typical YSZ or ceria based material. Furthermore, the pure oxide ion conductivity was observed almost over all partial pressure of oxygen on the $LaGaO_3$ based material which is different from ceria-based material that is reported to have purely high ionic conductivity at high oxygen partial pressure, but become partially reduced at low oxygen partial pressure.

Unlike proton conducting material, appropriate co doping can benefit oxide ion conductivity. S.Li[27] found that the addition of ZnO into YDC could effectively lower sintering temperature from 1500 to 1350℃ with the same thermal expansion remained and oxide ion conductivity improved (Figure 2.4). Y.Zheng[28] found that co-doping with appropriate ratio Strontium (Sr) into YDC could lead to improvements of oxide ion conductivity than pure YDC. For example, the 5% Sr co-doped YDC20 exhibits twice ionic conductivity than YDC20 at 750℃.

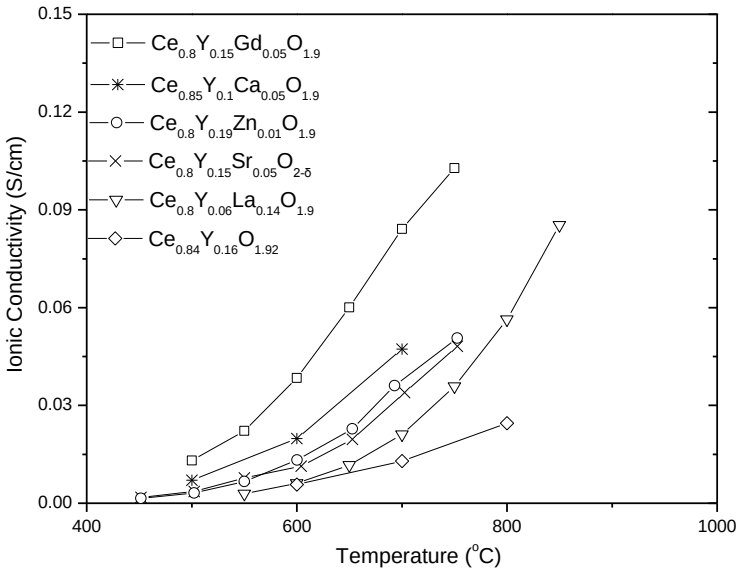

Fig. 2.4 Ionic conductivities of co-doping ceria materials on the basis of YDC

However, the desirable candidates for ACFC membrane in IDEAL cell should take into account not only electrical conductivity but also phase stability and thermal compatibility with both PCFC membrane and cathode materials, which actually are considered as the more important factors for fabricating central membrane. Since the Y-doped $BaCeO_3$ is chosen as first period attempts in IDEAL cell project, Y-doped ceria seems a judicious

choice among other Re-doped ceria oxides during first period attempts. The ionic conduction in YDC via diffusion or migration of oxygen vacancy is correlated with the mobility and concentration of vacancy. As we know, the vacancy is produced by substitution of Ce^{4+} with Y^{3+}. Theoretically, the more content of substitution (dopant concentration), the higher vacancy concentration could be expected. However, it is experimentally found that the ion conductivity does not always increase as doping concentration increases but reach a maximum value at about 15%-25% dopant concentration which is obviously presented in the Figure 2.5.

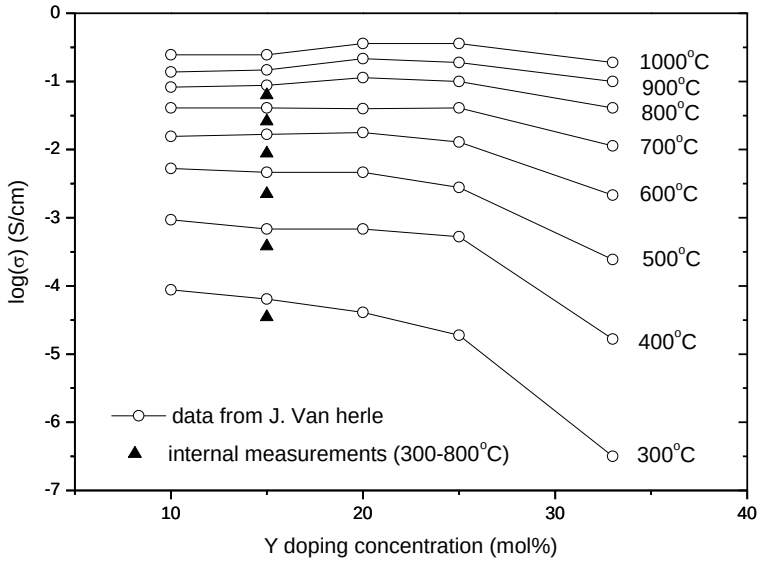

Fig. 2.5 Ionic conductivity of YDC measured in air as a function of dopant concentration

The data were collected from J. V. Herle[29] and also together with our measurements on YDC15, some small variations exists might be due to the differences of grain sizes. The ionic conductivity of YDC increased more quickly at 300-600℃ than above 700℃.All measured samples behaved similar tendencies of conductivities under Y concentrations. The nature of this phenomenon is still not very clear in detail. It is generally believed that defect interactions, clustering effects and/or the tendency for ordering play a role.

2.2. Conducting Phenomenon

In general, BCY (PCFC membrane) is a mixed conducting material both for protons and oxygen ions, while YDC (ACFC membrane) are only available for oxygen ion conduction. The mechanisms of conducing processes in both BCY and YDC are attributed to the presence of oxygen vacancies caused by doping effects. The conducting species in membrane especially in BCY vary with the conditions applied (e.g. temperatures and atmospheres). For instance, BCY is found to be pure protonic conducting material at the temperature below 500℃. When temperature is elevated to 500℃ to 800℃, mixed conductions including protons and oxygen ions can be observed in BCY. However, as the temperature exceeds 800℃, the numbers of proton transfer become a minority compared to oxygen ion transfer. BCY plays as same role as oxygen ion conducting materials. While the temperature effect on YDC is much simpler. From 600-1200℃, the higher temperature could possibly bring out higher oxygen ion conductivity during this conductible temperature ranges. In addition to the effects by temperatures, gas atmospheres play a more complicate role on conducting species and their conductivities. In the presence of hydrogen atmosphere, hydrogen reacts with oxygen ion in BCY lattice to form a proton and releases an electron, the process of which is written in Kröger-Vink notation 2.2:

$$\frac{1}{2}H_2 + O_O^x \leftrightarrow OH_O^{\bullet} + e^{-1} \tag{2.2}$$

The bonded proton with oxygen ion is namely proton defect, the transfer of which is viewed as the pattern of proton movement in lattice by either jumping to the neighboring oxygen ion or rotational diffusion of the unit [3]. Particularly, the participation of hydrogen also introduces the presence of electron in product leading to contribution of electron conduction to total conduction. As temperature raises, mobility of electron increases much faster than proton defects and oxygen ions signifying electron conductivity grows into the majority of total conductivity at high temperatures. Water has been found to have a positive effect on the proton conduction in BCY due to the hydration process of water into lattice which is written in Kröger-Vink notation 2.3. This reaction involves oxygen vacancy and lattice oxygen ion simultaneously by decomposing water into a hydroxide ion and a proton. The

hydroxide ion fills an oxygen vacancy while the proton is covalently bonded with oxygen ion which is similar to hydrogen reaction. Two proton defects are created stoichiometrically during hydration indicating the proton conduction could be possibly strongly influenced by water pressure.

$$H_2O + V_O^{\bullet\bullet} + O_O^x \leftrightarrow 2OH_O^{\bullet} \tag{2.3}$$

Although elevating temperature benefits moves of proton defects, hydration process is an exothermic process signifying high temperatures shift reaction 2.3 inversely and consequently weaken the protonic concentrations. It is found maximum protonic conductivity could be reached at approximate 700℃. Furthermore, since the hydration involves oxygen vacancy, it indicates the oxygen vacancy moving from bulk of perovskite to reaction sites to supply consumed vacancies during reaction. Although the species transported are proton defects in BCY, it could also be viewed as water transporting through electrolyte in the form of proton defects. In addition to proton defects, oxygen ions can also be conducted in both BCY and YDC due to oxygen vacancies exist in lattice. At high oxygen partial pressure, oxygen can dissolve into lattice to occupy one vacancy site and become an oxygen ion by liberating 2 electron holes. The reaction can be written in Kröger-Vink notation 2.4.

$$\frac{1}{2}O_2 + V_O^{\bullet\bullet} \leftrightarrow O_O^x + 2h^{\bullet} \tag{2.4}$$

At this high pressure area, oxygen ion conduction is accompanied by electron hole conduction which is famous as p-type conduction in the field of semiconductor. Oxygen Vacancies are believed as carriers for oxygen ions. Obviously, these species in pair are obligatory to counter-currently flow through electrolyte to balance local oxygen sites. From this understanding, oxygen ion conduction is equal to oxygen vacancy conduction. Therefore, it is more applicable to apply vacancy conduction instead of oxygen ion conduction because it is difficult to distinguish dissolved oxygen ions with lattice ions. One characteristic of conducting phenomenon in perovskite or fluorite is that the oxygen ion may separate itself from lattice to become oxygen atom and correspondingly create oxygen

vacancy and electrons when they are exposed in extremely oxygen partial pressures, which can be also written in Kröger-Vink notation 2.5:

$$O_O^x \leftrightarrow \frac{1}{2}O_2 + V_O^{\bullet\bullet} + 2e^- \tag{2.5}$$

At this low pressure area, electron conduction appears which is also called n-type conduction in comparison with p-type conduction. The oxygen ion conducting phenomenon is equivalent in both BCY and YDC, the differences of conductivities are mainly attributed to activation energies of oxygen vacancy diffusivity which leads to different conductivities. In sum, from above understanding of mass transfer phenomenon inside ceramic oxides, temperature mainly decides the conductivities. But types of transferred species are dependent on atmospheres which include hydrogen, oxygen and water.

2.3. Theory (Chemical defect model)

Among those reactions mentioned above, as long as associated concentrations are realized, it is theoretically possible to derive these conductivities under various temperature ranges and atmospheres. However, we are not going deep into a micro-scale theory on local concentrations. Conversely, an engineering approach based on chemical defect model is applied. As described, the conducting mechanism explains the reactions occur due to existing oxygen vacancies in lattice, which are actually the chemical defects that we concern. The chemical defect model assumes the concentrations of participants in reaction are on the steady state as long as temperature and gas composition are fixed, and the concentrations remaining uniform through electrolyte is also assumed by this model. Hence, the equilibrium constant which is the function of all involved concentrations is considered only as material and temperature dependent parameter. In this case, correlating equilibrium constant with constraints which are the oxygen sites conservation in lattice and neutralization of whole structure, it is possible to derive analytical expressions of each species at given conditions. The chemical defects of both BCY and YDC are aroused by doping trivalent yttrium to be in place of tetravalent cerium leading to one valence reduced, it creates an oxygen vacancy to electrically neutralize lattice. Since oxygen vacancy is

charged with bivalence, it indicates that 2 moles doped elements produce 1 mole oxygen vacancy in membrane without any conduction:

Without conduction: $S = 2C_V$

For instance, 10%Yttrium doped $BaCeO_3$ or CeO_2 could be expected to have maximum 5% mole fraction of oxygen vacancy in lattice. When conductions appear, the produced species are required to neutralize whole lattice which constitute following constraint:

With conduction: $S + \sum jC_{M^{-j}} = 2C_V + \sum iC_{M^{+i}}$

Negative Positive

Where *M* represents possible charged specie in conductions, the negative symbol *-j* signifies negative charged species (e.g. electron) are written on the left together with dopant concentration *S*. Correspondingly, positive symbol *+i* signifies positive charged species (e.g. proton defect and electron hole) which are written on the right with oxygen vacancy. This constraint is uniform in all incorporation reactions during conductions with only different specie types. In addition, oxygen sites conserve among oxygen ion, oxygen vacancy and proton defect (if present) in lattice which is expressed as:

Under p_w or p_{H2}: $[O_O^x] + [V_O^{\bullet\bullet}] + [OH^{\bullet}] = \delta$

Under p_{O2}: $[O_O^x] + [V_O^{\bullet\bullet}] = \delta$

Where δ is stoichiometric number of oxygen ion in oxides, for perovskite oxides (e.g. Yttrium doped $BaCeO_3$), δ is equal to 3. For fluorite oxides (e.g. Yttrium doped CeO_2), δ is equal to 2. Based on these constraints, we are able to derive expression of each concentration as following procedures.

2.3.1. In presence of only H_2O atmosphere

Equilibrium constant: $$K_w = \frac{C_{OH}^2}{p_w C_V C_O} \tag{2.6}$$

Oxygen site conservation: $$C_{OH} + C_O + C_V = 3 \tag{2.7}$$

Neutralization: $$S = 2C_V + C_{OH} \tag{2.8}$$

Combining 2.6-2.8, we obtain expressions:

$$C_{OH} = \frac{3\lambda_w - \sqrt{(3\lambda_w - S\lambda_w)^2 + \lambda_w(24S - 4S^2)}}{\lambda_w - 4} \tag{2.9}$$

$$C_V = \frac{S - C_{OH}}{2} \tag{2.10}$$

$$C_O = 3 - C_{OH} - C_V \tag{2.11}$$

Where $\lambda_w = K_w p_w$ is only variable in equation 2.9-2.11and it is also needed to be fitted with experimental results. Figure 2.6 presents the analytical solution of each concentration as a function of λ_w of BCY10.

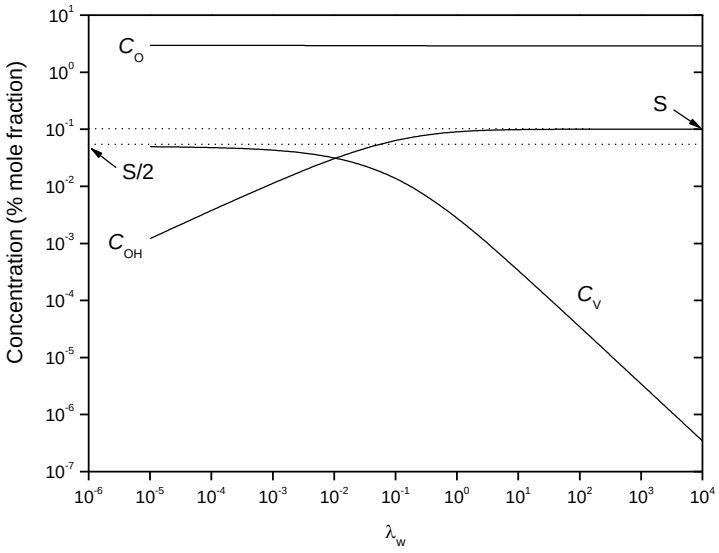

Fig. 2.6 Concentrations of proton defect, vacancy and oxygen ion in BCY10 against λ_w

As observed in Figure, upper limit of vacancy concentration (at extremely low λ_w indicating no hydration or little hydration takes place) is equal to half of doping concentration *S*. As hydration processes proceed leading to λ_w increasing, oxygen vacancies are converted to proton defect concentration until upper limit which is equal to doping concentration *S*. In this case, vacancy is null since they are all occupied by proton defects.

2.3.2. In presence of only H_2 atmosphere

Equilibrium constant: $$K_H = \frac{C_{OH}C_e}{p_{H_2}^{1/2}C_O} = \frac{C_{OH}^2}{p_{H_2}^{1/2}C_O} \quad (2.12)$$

Oxygen sites conservation: $$C_{OH} + C_O + C_V = 3 \quad (2.13)$$

Neutralization: $$S + C_e = 2C_V + C_{OH} \quad (2.14)$$

Combining with equation 2.12-2.14, we obtain following expressions:

$$C_{OH} = C_e = \frac{-\lambda_H + \sqrt{\lambda_H^2 + 4\lambda_H(3-S)}}{2} \quad (2.15)$$

$$C_V = S \quad (2.16)$$

$$C_O = 3 - C_{OH} - C_V \quad (2.17)$$

Where $\lambda_H = K_H p_H^{1/2}$ is similar to λ_w and is also required to be fitted, each concentration can be calculated based on equation 2.15-2.17 and is presented in Figure 2.7.

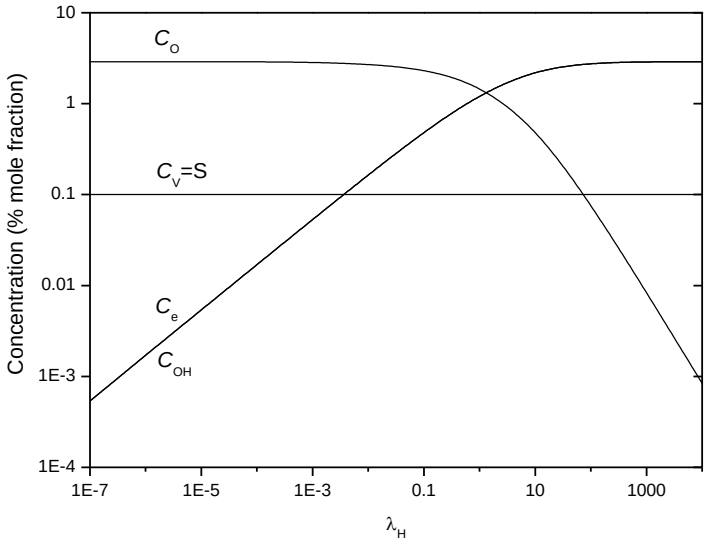

Fig. 2.7 Concentrations of proton defect, vacancy, electron and oxygen ion in BCY10 against λ_H

Oxygen vacancy is not involved in reaction which keeps constant during all range of λ_H. While proton defect as well as electron increases leading to decreasing of oxygen ion of

lattice. Theoretically speaking, upper limit concentration of proton defect and electron could reach 3-*S* which indicates all oxygen ion are bonded with hydrogen by reaction.

2.3.3. In presence of only O_2 atmosphere

1) High p_{O2} area (Forward reaction):

Equilibrium constant: $$K_O^+ = \frac{C_O C_h^2}{p_{O_2}^{1/2} C_V} \tag{2.18}$$

Oxygen conservation: $$C_O + C_V = \delta \tag{2.19}$$

Neutralization: $$S = 2C_V + C_h \tag{2.20}$$

2) Low p_{O2} area (Backward reaction):

Equilibrium constant: $$K_O^- = \frac{C_O}{p_{O_2}^{1/2} C_V C_e^2} \tag{2.21}$$

Oxygen conservation: $$C_O + C_V = \delta \tag{2.22}$$

Neutralization: $$S + C_e = 2C_V \tag{2.23}$$

δ is given 3 for BCY and 2 for YDC. By combining 2.18-2.20 and 2.21-2.23 and by denoting $\lambda_O^+ = K_O^+ p_O^{1/2}$ and $\lambda_O^- = K_O^- p_O^{1/2}$, we can obtain two complicated expressions of vacancy concentration at two pressure areas:

High p_{O2}: $$4C_V^3 - (4\delta + 4S)C_V^2 + (4\delta S + S^2 + \lambda_O^+)C_V - \delta S^2 = 0 \tag{2.24}$$

Low p_{O2}: $$4\lambda_O^- C_V^3 - 4\lambda_O^- S C_V^2 + (\lambda_O^- S^2 + 1)C_V - \delta = 0 \tag{2.25}$$

For these two cubic equations, it is possible to get analytical solution of vacancy concentration by applying a special discriminance as follows:

Step 1: to form a general form

$$ax^3 + bx^2 + cx + d = 0$$

Step 2: multiple roots discriminance:

$$A = b^2 - 3ac$$

$$B = bc - 9ad$$

$$C = c^2 - 3bd$$

$$\Delta = B^2 - 4AC$$

(1) If Δ> 0:

$$C_V = \frac{-b - \sqrt[3]{Y_1} - \sqrt[3]{Y_2}}{3a}$$

Where $Y_{1,2} = Ab + \frac{3a(-B \pm \sqrt{B^2 - 4AC})}{2}$

(2) If Δ= 0:

$$C_{V1} = -\frac{b}{a} + K$$

$$C_{V2} = C_{V3} = -\frac{K}{2}$$

Where $K = \frac{B}{A}$

(3) If Δ< 0:

$$C_{V1} = \frac{(-b - 2\sqrt{A}\cos\frac{\theta}{3})}{3a}$$

$$C_{V2} = \frac{(-b + \sqrt{A}(\cos\frac{\theta}{3} + \sqrt{3}\sin\frac{\theta}{3}))}{3a}$$

$$C_{V3} = \frac{(-b + \sqrt{A}(\cos\frac{\theta}{3} - \sqrt{3}\sin\frac{\theta}{3}))}{3a}$$

Where $\theta = \arccos T$, $T = (2Ab - 3aB) \big/ 2\sqrt{A^3}$, (A>0, -1<T<1)

To get reasonable resolution of oxygen vacancy, it requires vacancy concentration to be in following ranges:

High p_{O2}: $0 \le C_V \le \frac{S}{2}$

Low p_{O2}: $$\frac{S}{2} \le C_V \le S$$

By substituting parameters into equations 2.24 and 2.25, it is found Δ is less than zero. Together with the constraints mentioned above, it is concluded that C_{V2} is the solution of oxygen vacancy at high pressure area (forward reaction 2.4) while C_{V1} is the solution at low pressure area (backward reaction 2.5). All species concentrations are calculated by above expressions and collected in Figure 8 as a function of two variables λ_O^+ and λ_O^- respectively.

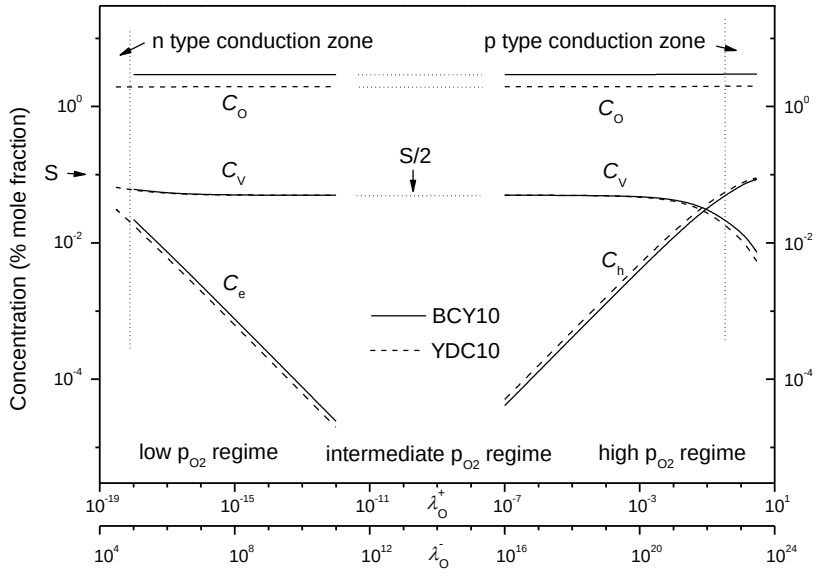

Fig. 2.8 Concentrations of vacancy, electron and oxygen ion in BCY10 and YDC10 against λ_O^+ and λ_O^-

At extremely high pressure, electron hole concentration is superior to vacancy concentration. Both BCY and YDC display p type conduction. In contrast, at extremely low pressure, electron concentration is close to vacancy concentration, which implies n type conduction existing at this area. Only at intermediate oxygen pressure area, vacancy concentration approximates to half of doping concentration *S* which is 3 orders higher than both electron or electron hole concentration. In this case, it is reliable to say pure oxygen ion conduction at this area. The electron concentration is believed to be reciprocal to electron hole concentration as follows:

$$K_{eh} = C_e C_h \tag{2.26}$$

Where this equilibrium constant K_{eh} is material dependent and can also be expressed by K_O^+ and K_O^-:

$$K_{eh} = (\frac{K_O^+}{K_O^-})^{1/2} \tag{2.27}$$

In general, equilibrium constants of incorporations are considered to be temperature dependent. As long as material and temperatures are ascertained, the conductivity of each charged specie can be predicted under all atmospheres.

2.4. Calculations and Discussions

In bulk of electrolyte, the concentration gradients are generally small, and the total current is carried mainly by migration. The conductivity actually can be written as the multiply of specie concentration and diffusivity (or mobility) by Nernst-Einstein equation 2.28. Total conductivity which can be obtained directly from measurements is sum of all contributions by equation 2.29.

$$\sigma_k = |z_k| F u_k C_k = \frac{z_k^2 F^2 D_k C_k}{R_g T} \tag{2.28}$$

$$\sigma_{tot} = \sum_k \sigma_k \tag{2.29}$$

Where *k* represents charged specie, *z* is the charger numbers carried by specie *k*, *u* is the mobility, *C* is concentration and *D* is diffusivity at temperature *T*. Among these, diffusivities are temperature and material dependent parameter. In addition to temperature, concentration is also dependent on atmosphere conditions. The values used in the following calculations of each species are listed in table 2.1.

Table 2.1 Diffusivities of charged species in BCY and YDC

T (℃)	D_{OH} ($\times10^{-5}$ cm^2/s, BCY)	D_V ($\times10^{-5}$ cm^2/s, BCY)	D_e ($\times10^{-5}$ cm^2/s, BCY)	D_h ($\times10^{-5}$ cm^2/s, BCY)	D_V ($\times10^{-5}$ cm^2/s, YDC)	D_e ($\times10^{-5}$ cm^2/s, YDC)
300	0.020	0.00057	0.0042	0.0038	0.0014	1.04
400	0.079	0.012	0.055	0.12	0.011	3.46

500	0.22	0.072	0.37	1.71	0.050	8.42
600	0.49	0.23	1.44	11.33	0.16	16.71
700	0.91	0.60	6.15	65.23	0.40	28.83
800	1.52	1.05	13	214.76	0.84	44.92

Transport number, which can also be indirectly estimated from experiments, is the ratio of conductivity of specie *k* to the total conductivity with the value ranging from zero to unity which can be written as equation 2.30:

$$t_k = \frac{|z_k| u_k C_k}{\sum_k |z_k| u_k C_k} = \frac{\sigma_k}{\sigma_{tot}} \tag{2.30}$$

2.4.1. Equilibrium constant K_H

If enough experimental data measured under single atmosphere are available, the equilibrium constants are more preferable and more accurate to be obtained. Unfortunately, few measurements of BCY conductivity over only hydrogen pressure ranges can be found so far. Many data about BCY conductivity were measured under wet atmosphere to investigate the effect of water on conductivity, equilibrium constant K_w has already been provided by Kreuer which is presented in Figure 2.16. In this case, an effective way of estimating hydrogen incorporation constant under mixture atmosphere is required as follows:

1) Rewriting two parallel reactions:

$$\frac{1}{2} H_2 + O_O^x \leftrightarrow OH^\bullet + e^{-1}$$
$$H_2O + V_O^{\bullet\bullet} + O_O^x \leftrightarrow 2OH_O^\bullet$$

With equilibrium constants:

$$K_H = \frac{C_{OH} C_e}{p_{H_2}^{1/2} C_O}$$
$$K_w = \frac{C_{OH}^2}{p_w C_V C_O} \tag{2.31}$$

By dividing K_w by K_H, we obtain:

$$\frac{K_w p_w}{K_H p_H} = \frac{C_{OH}}{C_V C_e}$$

Plus conservation: $$C_{OH} + C_O + C_V = 3 \tag{2.32}$$

And neutralization: $$S + C_e = 2C_V + C_{OH} \tag{2.33}$$

2) Naming another parameter $\lambda_{HW}=\lambda_H/\lambda_w$, we obtain following expressions:

$$\begin{aligned} C_{OH} &= \frac{\lambda_{HW} C_V (2C_V - S)}{1 - \lambda_{HW} C_V} \\ C_e &= \frac{(2C_V - S)}{1 - \lambda_{HW} C_V} \end{aligned} \tag{2.34}$$

In this case, two variables λ_{HW} and C_V are required to fit experimental data. Three available samples measured under wet hydrogen atmosphere were taken. The first one (BCY5) was investigated by J.Guan under 4.7%H_2O + 3.5%H_2 + N_2 from 600-800℃. The reason of validating this sample is due to not only total conductivity but also all part of contributions is provided. By fitting vacancy conductivity to experimental data, other conductivities were calculated by equation 2.34 the results of which are presented in Figure 2.9.

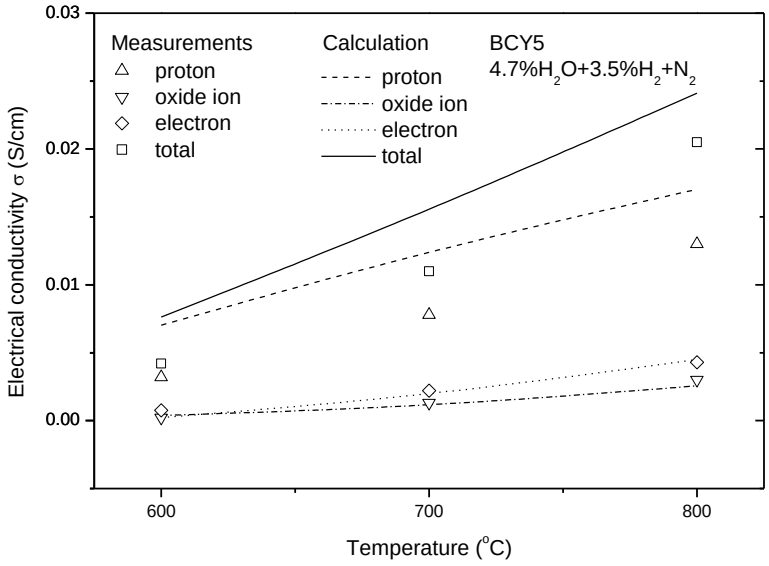

Fig. 2.9 Comparison of calculation with experimental results from J.Guan[14] on BCY5

The fitted K_H are 6.3×10^{-3}, 2.5×10^{-3}, 6.3×10^{-4} $atm^{-1/2}$ at 600,700,800℃ respectively. Under this atmosphere, proton conductivity is higher than conductivities of oxygen ion and electron since the effect of water on proton conductivity is much stronger than hydrogen. The second sample was taken from W.Suksamai who measured BCY10 conductivity under $2.3\%H_2O + 5\%H_2 + N_2$. The atmosphere is similar to first one but with different dopant concentration S. In this validation presented in Figure 2.10, the fitted K_H were still applied with 6.3×10^{-3}, 2.5×10^{-3}, 6.3×10^{-4} $atm^{-1/2}$ at 600, 700 and 800℃ respectively. The calculation on conductivity agreed better at 700 and 800℃ than at 500 ℃ while on ionic transport number it perfectly matched with measurements. The third sample was measured under 1.7% wet hydrogen. The ratio of hydrogen to water is much higher than previous two. At this high pressure ratio, total conductivity seems to be improved dramatically than the one under water pressure which is presented in Figure 2.11. In case of previous two samples, proton conductions still were majority of total conduction due to small amount of hydrogen was applied. In case of third sample, since majority of feeding gas was hydrogen leading to large number of electrons produced. The proton conductivity were drawn as dashed line which exhibited a maximum value around 600℃.

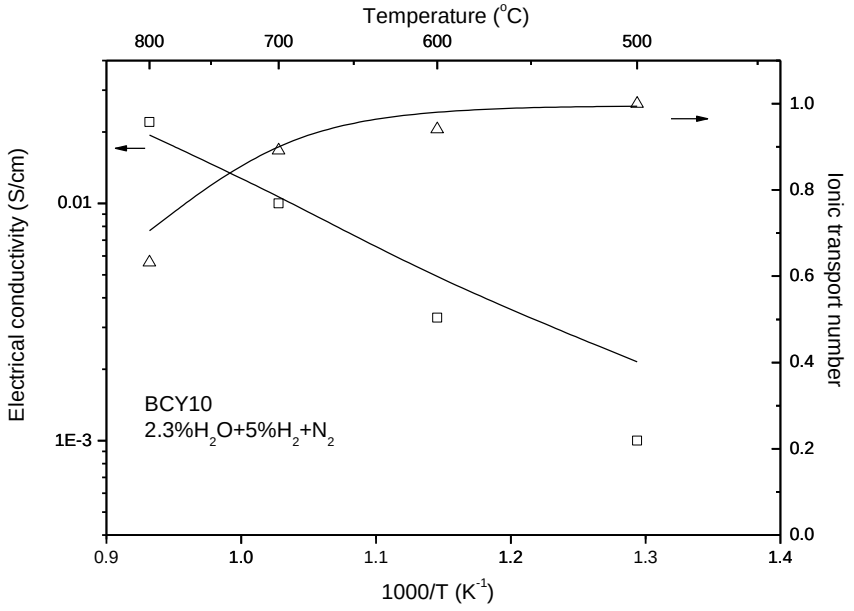

Fig. 2.10 Comparison of calculation with experimental results from W.Suksamai[18] on BCY10

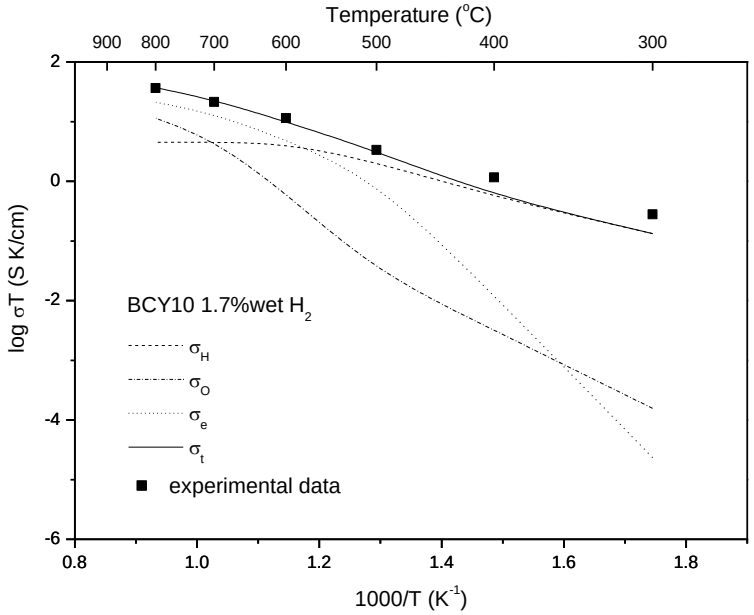

Fig. 2.11 Electrical conductivity of BCY10 from K. Katahira[15] as a function of temperatures

2.4.2. Equilibrium Constant K_O (K_O^+ and K_O^-)

There are two references about BCY conductivity under a range of oxygen pressures. A.N.Virkar[30] measured electrical conductivity of BCY10 as a function of oxygen pressure from 1atm down to 10^{-14} atm in the temperature from 600-800℃. The calculation based on chemical model agrees perfect with experimental data on both total conductivities and transport numbers in Figure 2.12 by setting effective doping concentration S' at 0.3 and equilibrium constants K_O^+ correspondingly are obtained as 1.3×10^{-3}, 2.5×10^{-4} and 6.3×10^{-5} $atm^{-1/2}$ at 600℃, 700℃, 800℃ respectively. Mixed conduction appears when oxygen pressure exceeds 1 Pa. Although total conductivity rises to twice of one at intermediate area (smaller than 10^{-3} Pa or 10^{-8} atm) during which it is believed to be pure oxygen ionic conduction, the transport number indicates ionic conductivity remains constant during high oxygen pressure area while the augment is almost attributed from electron hole conduction. The data of transport numbers obtained from reference are only one group, while calculation results shows the differences under 600-800℃ exist though minor. The small effective doping concentration implies that the sample was possibly fabricated coarsely.

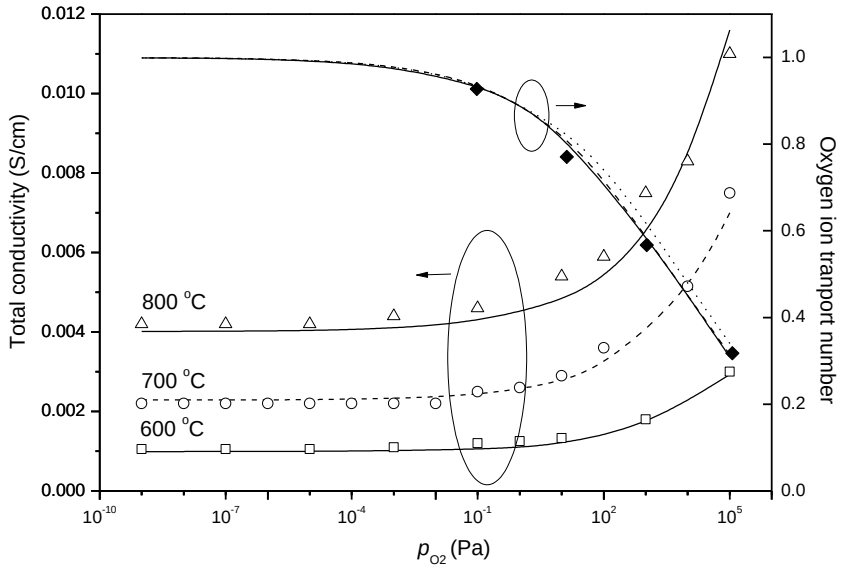

Fig. 2.12 Comparison of calculation (smooth lines) with experimental data[30] of BCY10 on total conductivity(solid dots) and transport numbers(hollow dots) as a function of p_{O2}

Unfortunately, limited experimental data of BCY conductivity measured under only oxygen atmosphere are available. M.Oishi [31] measured electrical conductivity of BCY10 under O_2/H_2O mixture atmospheres from 500-900℃. To effective validate chemical model under this case, it is necessary to derive following steps:

1) Rewriting two incorporations in parallel:

High p_{O2}:

$$\frac{1}{2}O_2 + V_O^{\bullet\bullet} \leftrightarrow O_O^x + 2h^{\bullet} \qquad (2.35)$$
$$H_2O + V_O^{\bullet\bullet} + O_O^x \leftrightarrow 2OH_O^{\bullet}$$

Equilibrium constants:

$$K_O^+ = \frac{C_O C_h^2}{p_{O_2}^{1/2} C_V} \qquad (2.36)$$
$$K_w = \frac{C_{OH}^2}{p_w C_V C_O}$$

Low p_{O2}:

$$\frac{1}{2}O_2 + V_O^{\bullet\bullet} + 2e^{-1} \leftrightarrow O_O^x \qquad (2.37)$$
$$H_2O + V_O^{\bullet\bullet} + O_O^x \leftrightarrow 2OH_O^{\bullet}$$

Equilibrium constants:

$$K_O^- = \frac{C_O}{p_{O_2}^{1/2} C_V C_e^2}$$
$$K_w = \frac{C_{OH}^2}{p_w C_V C_O} \tag{2.38}$$

By multiplying K_O^+ with K_w and K_O^- with K_w respectively, we can obtain:

$$K_O^+ p_{O_2}^{1/2} K_w p_w = (\frac{C_h C_{OH}}{C_V})^2$$
$$K_O^- p_{O_2}^{1/2} K_w p_w = (\frac{C_{OH}}{C_V C_e})^2$$

2) Naming one parameter $\lambda_{ow}=(K_O p_O^{1/2} K_w p_w)^{1/2}$, we obtain the relationship:

$$\lambda_{OW}^+ C_V = C_h C_{OH}$$
$$\lambda_{OW}^- C_V C_e = C_{OH} \tag{2.39}$$

Obviously, $\lambda_{OW}^+ / \lambda_{OW}^- = K_O^+ / K_O^- = K_{eh}$. By substituting the oxygen site conservation and neutralization constraints:

$$C_{OH} + C_V + C_O = 3$$

High p_{O2}: $$S = 2C_V + C_{OH} + C_h$$

Low p_{O2}: $$S + C_e = 2C_V + C_{OH}$$

In this case, concentrations can be written as following expressions:

High p_{O2}:

$$C_V = \frac{C_{OH}(S - C_{OH})}{\lambda_{ow}^+ + 2C_{OH}}$$
$$C_h = \frac{\lambda_{ow}^+ (S - C_{OH})}{\lambda_{ow}^+ + 2C_{OH}} \tag{2.40}$$

Low p_{O2}:

$$C_{OH} = \frac{\lambda_{ow}^- C_V (2C_V - S)}{1 - \lambda_{ow}^- C_V}$$
$$C_e = \frac{2C_V - S}{1 - \lambda_{ow}^- C_V} \tag{2.41}$$

Calculation on BCY10 conductivity under wet oxygen atmospheres were made based on M.Oishi's experimental data [31] who investigated BCY10 over extended oxygen pressure

range from 1 atm down to 10^{-18} atm, the results of which are presented in Figure 2.13. The calculation were divided into two steps, the first one was to calculate forward reaction constant K_O^+ at oxygen pressure area from 10^{-6} to 1 atm. The second one was to calculate backward reaction constant K_O^- at oxygen pressure area from 10^{-28} to 10^{-15} atm. Finally combining results at two areas we obtain a complete calculation results represented by smooth lines.

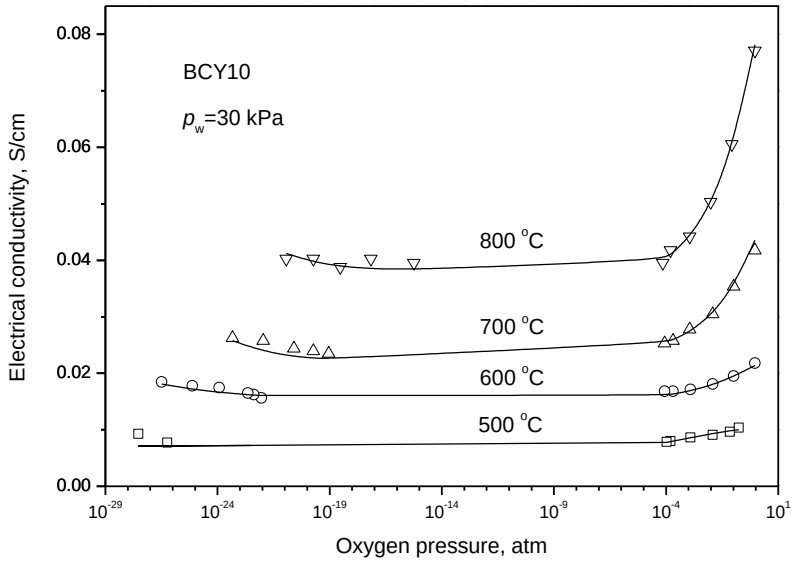

Fig. 2.13 Comparison of calculation with experimental data of BCY10 conductivity under wet oxygen atmosphere and 500-800℃, dots are taken from M.Oishi [31], smooth lines are calculation based on chemical defect model

The agreements between calculation with experimental data are very well at 500 and 600℃, where proton conduction is predominant. High temperatures (700 and 800℃) incite high mobilities of electron hole, which give rise of BCY10 total conductivity at high oxygen pressure areas. The transport numbers are also provided at high pressure areas, in which we presented calculations of all contributions to total conductivity in Figure 2.14. Apparently, the oxygen pressure dependence of proton defects and electrons are weak, while the oxygen ion conductivity is more related with oxygen partial pressures. The total conductivity could be matched very well although a few variations exist by oxygen ion contribution. In general, the fitted equilibrium constants are more accurate at low temperature and at high pressure area. It still requires more experimental data to validate these constants.

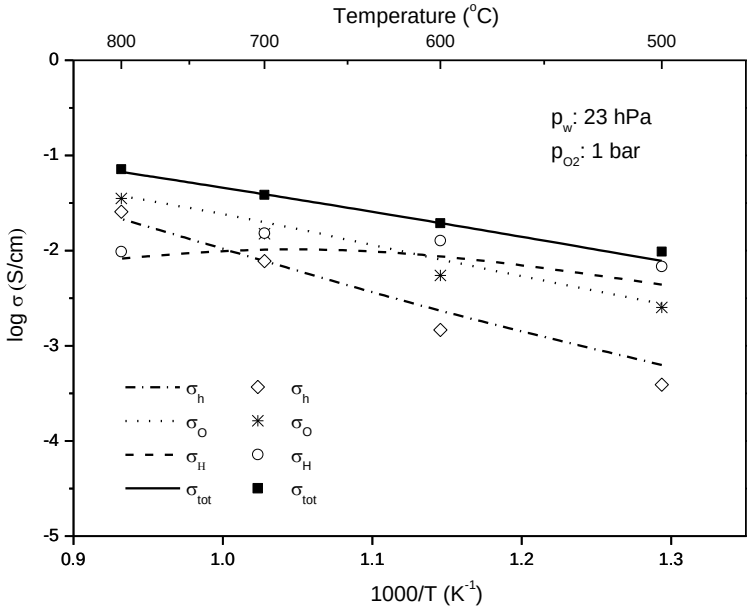
Temperature (°C)
800
700
600
500
0
-1
-2
-3
-4
-5
log σ (S/cm)
p_w: 23 hPa
p_O2: 1 bar
σ_h
σ_O
σ_H
σ_tot
0.9
1.0
1.1
1.2
1.3
1000/T (K^-1)

(a)

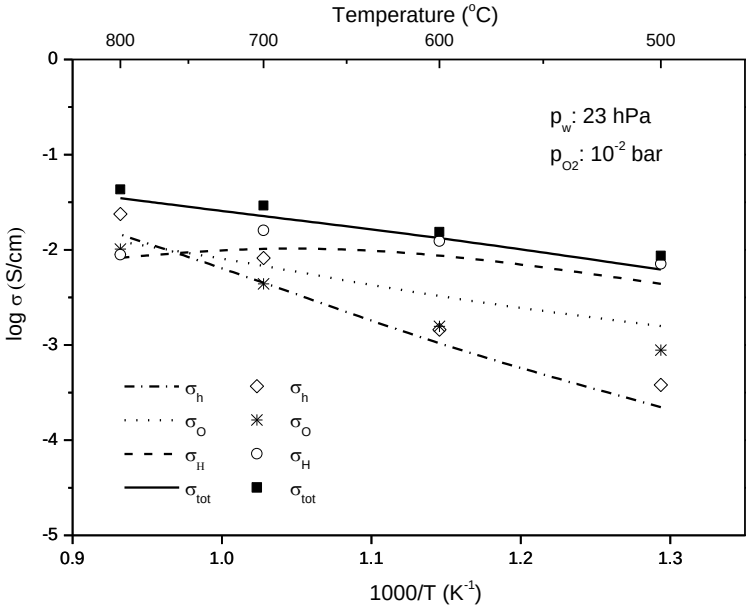
Temperature (°C)
800
700
600
500
0
-1
-2
-3
-4
-5
log σ (S/cm)
p_w: 23 hPa
p_O2: 10^-2 bar
σ_h
σ_O
σ_H
σ_tot
0.9
1.0
1.1
1.2
1.3
1000/T (K^-1)

(b)

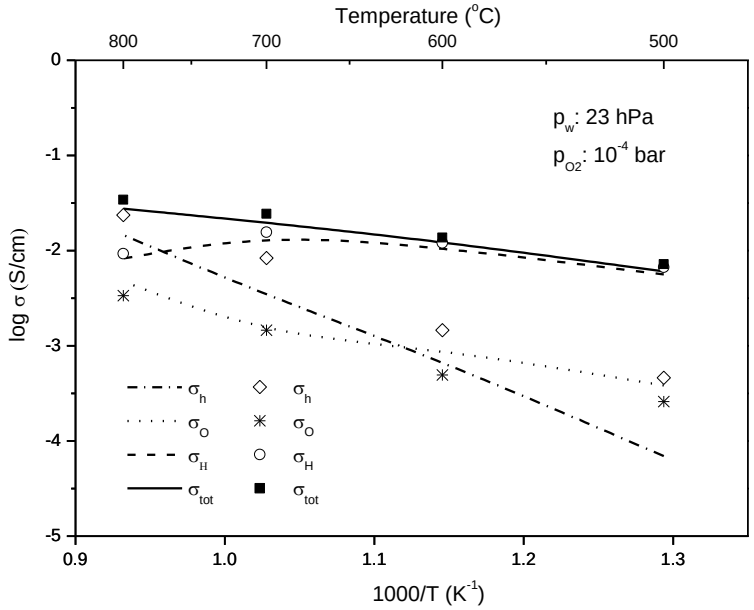

(c)

Fig. 2.14 Calculation of all contributions to total conductivity of BCY10 at a) wet p_{O2}=1 atm, b) wet p_{O2}=0.01 atm, c) wet p_{O2}=0.0001 atm

For YDC sample, the calculations agree perfect with experimental results at all oxygen partial pressure range (from 1 atm to 10^{-12} atm) which is presented in Figure 2.15. Observed from Figure, electronic conduction started to appear as oxygen pressure was below 10^{-5} Pa. During the range of 10^{-15}-10^{-23} atm, the total conductivity is proportional to $P_{O2}^{-1/6}$ - $P_{O2}^{-1/8}$. The equilibrium constant K_O^- were fitted with values of 4.7×10^{16} $atm^{-1/2}$ at 600℃ and 9.5×10^{14} $atm^{-1/2}$ at 700℃, which indicates that YDC under same oxygen pressure condition exhibits more electronic conduction at high temperature than low temperature. The calculation results also revealed that as long as oxygen pressure is above 10^{-8} atm, the YDC conductivity keeps as high as high oxygen pressure is applied. And the conducting specie is pure oxide ion. However, no electron hole conduction is observed from experimental results. In this case, the forward equilibrium constant K_O^+ of YDC has not been taken into account.

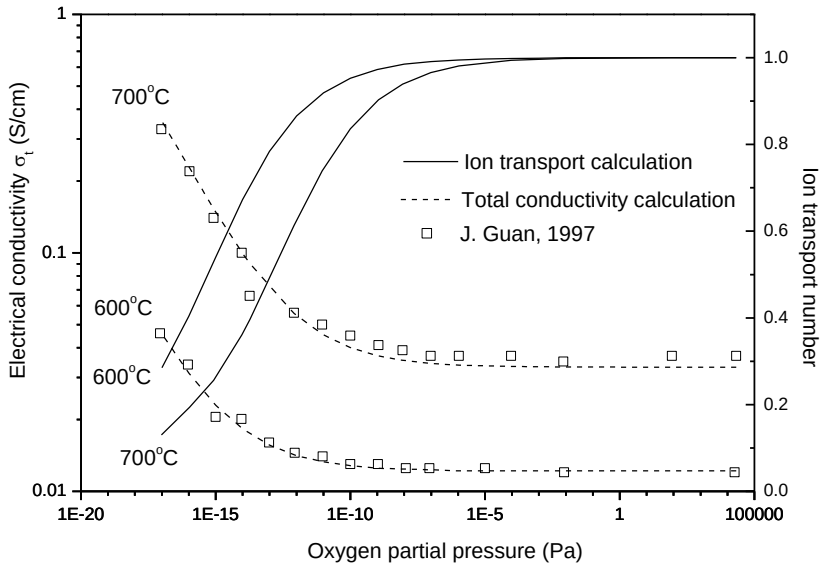

Fig. 2.15 Electrical conductivity of YDC20 as a function of oxygen partial pressure, cubic dots and triangle dots are experimental results from Ref[32], smooth lines are calculations.

2.4.3. Relationships between equilibrium constants

Rewriting three incorporations together with individual Gibbs free energy relevant to their equilibrium constants by Van't Hoff equation in table 2.2, it is found that twice of reaction 3 plus reaction 2 and minus reaction 1 is equivalent to a very common hydration between hydrogen and oxygen (equation 2.45).

Table 2.2 Gibbs free energies of incorporations expressed by Van't Hoff equations

(1)	$H_2O + O_O^x + V_O^{\bullet\bullet} \xleftrightarrow{K_w} 2OH^{\bullet}$	$\Delta G_w = -R_g T \ln K_w$
(2)	$\frac{1}{2}O_2 + V_O^{\bullet\bullet} + 2e^- \xleftrightarrow{K_O^-} O_O^x$	$\Delta G_O = -R_g T \ln K_O$
(3)	$\frac{1}{2}H_2 + O_O^x \xleftrightarrow{K_H} OH^{\bullet} + e^-$	$\Delta G_H = -R_g T \ln K_H$

By combination of above reaction (3) ×2 + reaction (2) - reaction (1):

$$H_2 + 2O_O^x + \frac{1}{2}O_2 + V_O^{\bullet\bullet} + 2e^- - H_2O - O_O^x - V_O^{\bullet\bullet} \leftrightarrow 2OH^{\bullet} + 2e^- + O_O^x - 2OH^{\bullet}$$

Simplifying this equation to obtain:

$$H_2 + \frac{1}{2}O_2 \leftrightarrow H_2O \tag{2.42}$$

According to thermodynamic law, the Gibbs free energy is only relevant to reactants and products, which indicate that the Gibbs free energies of four reactions have following relationship:

$$2\Delta G_H + \Delta G_O - \Delta G_w = \Delta G_{H_2O} \tag{2.43}$$

Therefore, we can obtain the following relationship of equilibrium constants:

$$\frac{K_H^2 K_O^-}{K_w} = K_{H_2O} \tag{2.44}$$

We can apply this relationship to validate our calculation on other equilibrium constants since K_{H2O} as a function of temperature is already known. This idea of validation calculation is originally proposed by this thesis. And we collect all of equilibrium constants in the range of 500-800℃, the results of calculated equilibrium constants are presented together with constants from references.

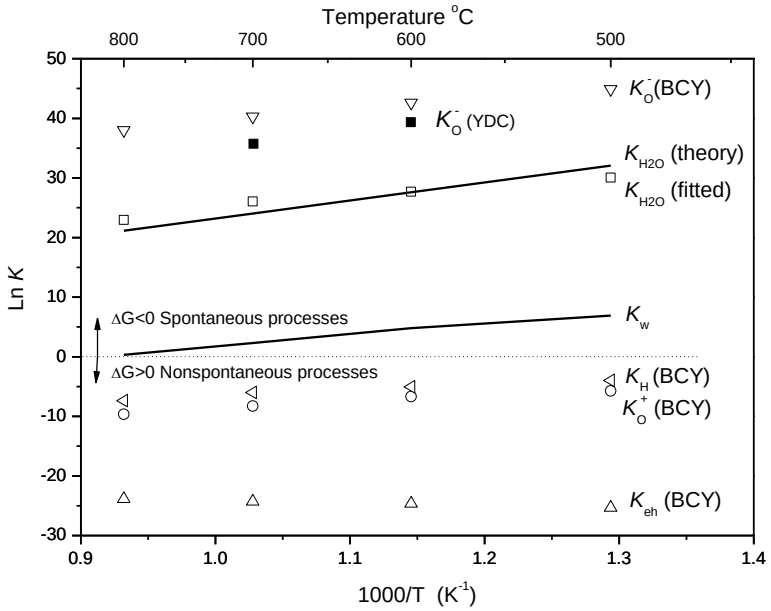

Fig. 2.16 Collection of all equilibrium constants as a function of temperatures, dots are obtained by fitting experimental data, smooth lines(K_w and K_{H2O}) are taken from references[2, 33]

Dots are obtained by fitting with experimental data as introduced before. K_w and K_{H2O} represented as smooth lines are taken from J.M.Smith and K.D.Kreuer respectively. The primary objective is to show the calculated K_{H2O} with the one from reference which is calculated on basis of Gibbs free energy. It is seen that calculated K_{H2O} is close to reference value with similar slope. However, due to equilibrium constants are calculated from available samples which were not uniformly fabricated, the variance between calculation and theory is still existing but acceptable. All other equilibrium constants in both BCY and YDC are also collected in Figure 2.16 to show their temperature dependent relationships. These parameters are very important for us to acknowledge the reaction properties which are tightly related with conductivities of materials. For example, the values of LnK in the Figure give us general information about Gibbs free energy of processes. During 500-800℃, the processes located below LnK=0 (dot line in Figure) such as hydrogen incorporation and oxygen incorporation are non-spontaneous processes which are required heat energy supply to occur. In contrary, the processes such as water incorporation and water formation by hydrogen and oxygen, oxygen ion desorption in both BCY and YDC are spontaneous in these temperature ranges, which indicates that they are exothermal processes.

2.4.4. Predictions

From this understanding of mass transfer phenomenon inside ceramic oxides, proton transportation can be viewed as transportation of proton defects which are formed by either hydrogen or water with perovskite material. The flux is related with proton defect concentration, hydrogen partial pressure, water partial pressure, oxygen partial pressure, vacancy concentration and oxide ion concentration. Based on the IDEAL cell design, BCY is supposed to work between wet hydrogen and water. Figure 2.17 schematically draws conducting species in different temperature areas. Provided the water pressure on the other side is not taken into account, conducting species and conductivities are completely decided by composition of fuels (i.e. H_2+H_2O). By fixing system pressure at 1 atm, partial pressure of water is varied from 0 to 1 atm, calculated protonic conductivity based on obtained equilibrium constants of BCY10 is presented in Figure 2.18.

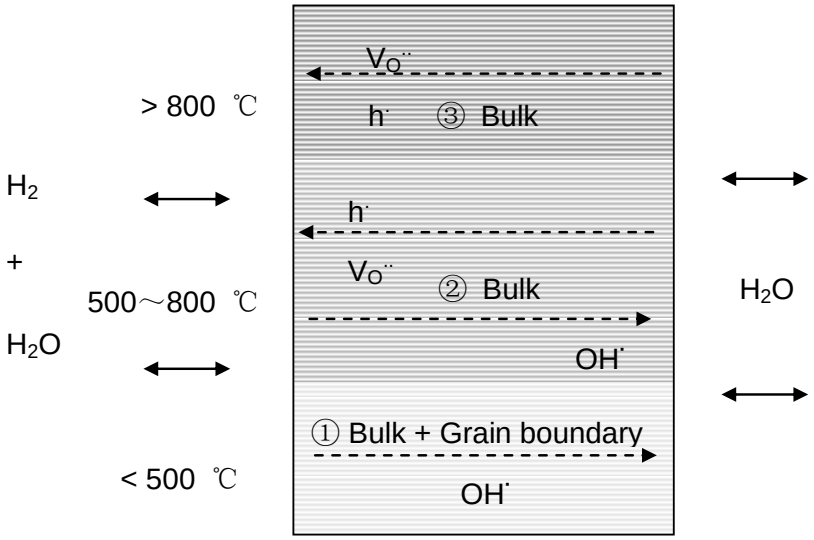

Fig. 2.17 Transport phenomenon in BCY: (1) only proton transfer at low temperature, (2) mix transfer of proton and vacancy, (3) vacancy transfer dominates

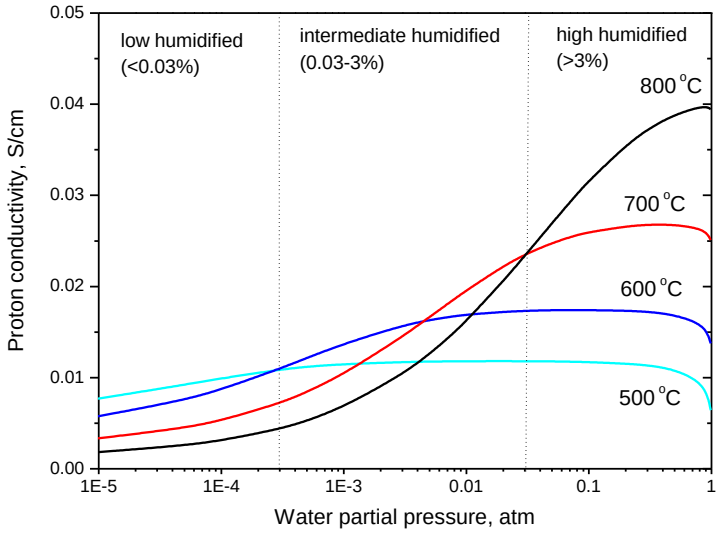

Fig. 2.18 Diagram of electrical conductivity of BCY10 as a function of fuel composition (H_2O/H_2) at intermediate temperatures

Obvious differences of these same type cerates can be observed. The variance of protonic conductivity in BCY10 can be classified into three kinds: low humidified hydrogen (<0.03%), intermediate humidified hydrogen (0.03-3%) and high humidified hydrogen (>3%). In the first case, higher temperature plays a negative role on protonic conductivity due to slower incorporation rate can be estimated from apparent KH. When water content is increased to intermediated level, water incorporation plus hydrogen incorporation take

effect simultaneously. Ultimate results rest on both temperature and humidity. In other words, if 1% wet hydrogen is supplied, maximum protonic conductivity can be achieved at 700℃. When humidify exceeds 3%, the role of water is superior to hydrogen, which is manifested higher temperature benefits higher protonic conductivity. The result presented in figure 11a also provides us the information for temperature oriented operation. For instance, if the cell is designed to work under 500, 600, 700 or 800℃, correspondingly, 0.1%, 3%, 40% and 90% humidified hydrogen are required for each case to obtain optimum protonic conductivity in BCY10.

The pressure produced water on the right, which is relevant with current density and CM morphology (introduce in the next chapter), also plays a significant negative role on proton conductions. The water pressure in CM is assumed to vary from vacuum to 1 atm, which is also supposed to take dissociation into BCY10 to counterbalance proton defect concentration. Based on the model introduced above, the conductivities were drawn in Figure 2.19. The larger pressure accumulated, the more negative effect on the conductivity could be expected. For instance, if water pressure accumulated in CM exceeds 10^4 Pa (0.1 atm), the effective conductivity could possibly fall to the half of original values when there is no effect by water.

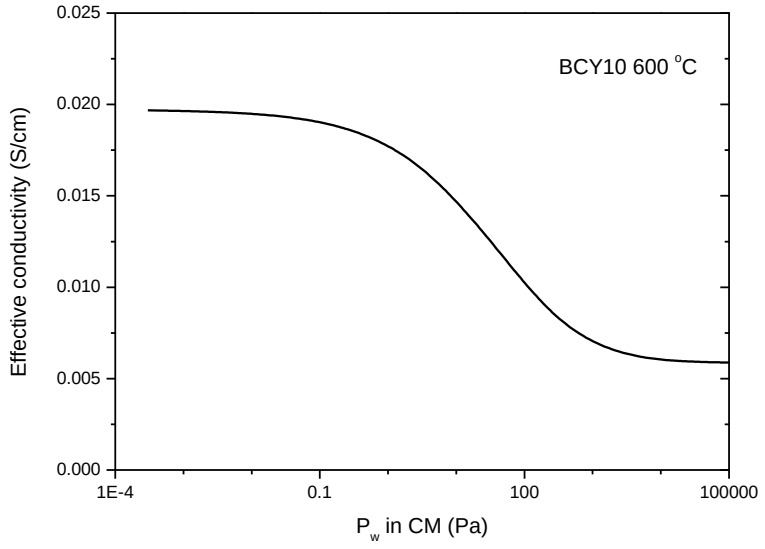

Fig. 2.19 Effect of water pressures in CM on total and proton conductivity in BCY10

2.5. Conclusions

In this chapter, material conductivities on the basis of chemical defect model have been studied as a function of temperature ranges (500-800℃) and atmospheres (hydrogen, oxygen and water). The equations applied in model are summarized in following table 2.3. Table 2.4 and 2.5 provide the analytical solutions to those equations when the membrane is exposed to single atmosphere and mixed atmospheres.

Table 2.3 Summary of equations in chemical defect model

Gas	Reaction	Equilibrium constant	Oxygen sites	Neutralization
p_{H_2}	$\frac{1}{2}H_2+O_O^x \Leftrightarrow OH^\bullet + e^{-1}$	$K_H=\frac{C_{OH}C_e}{p_{H_2}^{1/2}C_O}$	$C_{OH}+C_O+C_V=3$	$C_e=C_{OH}$
p_{H_2O}	$H_2O+O_O^x+V_O^{\bullet\bullet} \Leftrightarrow 2OH^\bullet$	$K_w=\frac{C_{OH}^2}{p_wC_VC_O}$	$C_{OH}+C_O+C_V=3$	$S=C_{OH}+2C_V$
high p_{O_2}	$\frac{1}{2}O_2+V_O^{\bullet\bullet} \Leftrightarrow O_O^x+2h^\bullet$	$K_O^+=\frac{C_OC_h^2}{p_{O_2}^{1/2}C_V}$	$C_O+C_V=\delta\begin{cases}=2 \text{ YDC}\\=3 \text{ BCY}\end{cases}$	$S=2C_V+C_h$
low p_{O_2}	$\frac{1}{2}O_2+V_O^{\bullet\bullet}+2e^{-1} \Leftrightarrow O_O^x$	$K_O^-=\frac{C_O}{p_{O_2}^{1/2}C_VC_e^2}$		$S+C_e=2C_V$

Table 2.4 Solution to chemical defect model in one atmosphere

Gas	Variables	C_V	C_{OH}	C_h	C_e
p_{H_2}	$\lambda_H=K_Hp_{H_2}^{1/2}$	$\frac{S}{2}$	$\frac{-\lambda_H+\sqrt{\lambda_H^2+4\lambda_H(3-S/2)}}{2}$	≈ 0	$\frac{-\lambda_H+\sqrt{\lambda_H^2+4\lambda_H(3-S/2)}}{2}$
p_{H_2O}	$\lambda_w=K_wp_w$	$\frac{S-C_{OH}}{2}$	$\frac{3\lambda_w-\sqrt{(3\lambda_w-S\lambda_w)^2+\lambda_w(24S-4S^2)}}{\lambda_w-4}$	≈ 0	≈ 0
high p_{O_2}	$\lambda_O^+=K_O^+p_{O_2}^{1/2}$	See 3.3	—		≈ 0
low p_{O_2}	$\lambda_O^-=K_O^-p_{O_2}^{1/2}$	See 3.3	—	≈ 0	

Table 2.5 Solution to chemical defect model in two mixed atmospheres

Gas	Variables	C_V	C_{OH}	C_h	C_e

$p_{H_2} + p_{H_2O}$	$\lambda_{HW} = \frac{\lambda_H}{\lambda_w},\ C_V$	—	$\frac{\lambda_{HW} C_V (2C_V - S)}{1 - \lambda_{HW} C_V}$	≈ 0	$\frac{(2C_V - S)}{1 - \lambda_{HW} C_V}$
high $p_{O_2} + p_{H_2O}$	$\lambda^+_{OW} = (\lambda^+_O \lambda_w)^{1/2},\ C_{OH}$	$\frac{C_{OH}(S - C_{OH})}{\lambda^+_{ow} + 2C_{OH}}$	—	$\frac{\lambda^+_{ow}(S - C_{OH})}{\lambda^+_{ow} + 2C_{OH}}$	≈ 0
low $p_{O_2} + p_{H_2O}$	$\lambda^-_{OW} = (\lambda^+_O \lambda_w)^{1/2},\ C_V$	—	$\frac{\lambda^-_{OW} C_V (2C_V - S)}{1 - \lambda^-_{OW} C_V}$	≈ 0	$\frac{2C_V - S}{1 - \lambda^-_{ow} C_V}$

For proton conducting material (Yttrium doped $BaCeO_3$), a comprehensive understanding of conducting mechanism plus a chemical defect model has been demonstrated, which has taken into account proton conduction not only by water but also by hydrogen especially at high hydrogen pressure and above 600℃. Several samples were taken to fit equilibrium constants (K_H and K_O) of hydrogen and oxygen incorporations. It was found that these constants decrease as temperature rise. At 600℃, BCY has the potential to provide 0.02 S/cm proton conductivity as fuel is fed with 10%wet hydrogen. However, the water accumulated in CM has been demonstrated in chapter 1 to be kept as lower pressure as possible to achieve highest theoretical EMF. In this chapter, the water pressure in CM is also considered to have a negative effect on proton conductivity. As demonstrated above, the proton conductivity could fall to half value if water pressure is accumulated to 0.1 atm.

For the oxygen ion conducting material (YDC), the phenomenon is much simpler than BCY. The relationship between oxygen ion conductivity with temperature and oxygen pressure were built. Although suggested applied in high temperature, oxygen ion conductivity still could be reached at 0.01 S/cm by YDC as long as oxygen pressure exceeds 1 Pa. It was also mentioned, although above 600℃, the grain boundary effect on total conductivity disappears as long as relative density of dense electrolyte is above 96%. It should become an issue when fabricating porous CM.

References

1. H. Iwahara, H.U., K. Ono, K. Ogaki, Journal of electrochemical society, 1988. 135.

2. Kreuer, K.D., *Proton-conducting oxides.* Annual Review of Materials Research, 2003. 33: p. 333-359.

3. Kreuer, K.D., *On the complexity of proton conduction phenomena.* Solid State Ionics, 2000. 136-137: p. 149-160.

4. Melnik, J., et al., *Distinguishing between apparent and authentic conductivity of protonic ceramic electrolytes using differential resistance analysis applied to conductivity measurements*. Journal of Power Sources, 2008. 185(2): p. 1101-1106.

5. Flint, S.D. and R.C.T. Slade, *Variations in ionic conductivity of calcium-doped barium cerate ceramic electrolytes in different atmospheres*. Solid State Ionics, 1997. 97(1-4): p. 457-464.

6. Gorbova, E., et al., *Influence of Cu on the properties of gadolinium-doped barium cerate.* Journal of Power Sources, 2008. 181(2): p. 292-296.

7. Fei Zhao, Q.L., Siwei Wang, et al, *Synthesis and characterization of* $BaIn_{0.3-x}Y_xCe_{0.7}O_{3-d}$ *(x = 0, 0.1, 0.2, 0.3) proton conductors.* International journal of hydrogen energy, 2010, 35.

8. Zhang, C. and H. Zhao, *Electrical conduction behavior of Sr substituted proton conductor* $Ba_{1-x}Sr_xCe_{0.9}Nd_{0.1}O_{3-\delta}$. Solid State Ionics, 2010. 181(33-34): p. 1478-1485.

9. Gopalan S, V.A.V., *Thermodynamic stabilities of* $SrCeO_3$ *and* $BaCeO_3$ *using a molten salt method and galvanic cells*. Journal of the Electrochemical Society, 1993. 140.

10. Matsumoto H, K.Y., Ito N, Enoki M, Ishihara T., *Relation between electrical conductivity and chemical stability of* $BaCeO_3$*-based proton conductors with different trivalent dopants*. Electrochmical and Solid-State Letters, 2007. 10.

11. Scholten M J, S.J., Miltenburg J C V, Oonk H A J., *Synthesis of strontium and barium cerate and their reaction with carbon dioxide.* Solid State Ionics, 1993. 61.

12. Zakowsky N, W.S., Irvine J T S., *Elaboration of CO_2 tolerance limits of $BaCe_{0.9}Y_{0.1}O_{3-\delta}$ electrolytes for fuel cells and other applications*. Solid State Ionics, 2005. 176.

13. Yingxin Guo, B.L., Qing Yang, et al, *Preparation via microemulsion method and proton conduction at intermediate-temperature of $BaCe_{1-x}Y_xO_{3-a}$*. Electrochemistry Communications, 2009, 11.

14. Guan, J., et al., *Transport properties of $BaCe_{0.95}Y_{0.05}O_{3-\alpha}$ mixed conductors for hydrogen separation*. Solid State Ionics, 1997. 100(1-2): p. 45-52.

15. Katahira, K., et al., *Protonic conduction in Zr-substituted $BaCeO_3$.* Solid State Ionics, 2000. 138(1-2): p. 91-98.

16. Fu, X.-Z., et al., *Y-doped $BaCeO_{3-\delta}$ nanopowders as proton-conducting electrolyte materials for ethane fuel cells to co-generate ethylene and electricity*. Journal of Power Sources, 2010. 195(9): p. 2659-2663.

17. Xie, K., R. Yan, and X. Liu, *Stable $BaCe_{0.7}Ti_{0.1}Y_{0.2}O_{3-\delta}$ proton conductor for solid oxide fuel cells.* Journal of Alloys and Compounds, 2009. 479(1-2): p. L40-L42.

18. Suksamai, W. and I.S. Metcalfe, *Measurement of proton and oxide ion fluxes in a working Y-doped $BaCeO_3$ SOFC.* Solid State Ionics, 2007. 178(7-10): p. 627-634.

19. Kreuer, K.D., *Proton Conductivity: Materials and Applications.* Chemistry of Materials, 1996. 8.

20. Chun-Keung Loonga, M.O., Ken Takeuchi, Koichi Ui, et al, *Neutron studies of rare earth-modified zirconia catalysts and yttrium-doped barium cerate proton-conducting ceramic membranes*. Journal of Alloys and Compounds, 2006. 408-412.

21. Yamamoto, O., *Solid oxide fuel cells: fundamental aspects and prospects.* Electrochimica Acta, 2000. 45(15-16): p. 2423-2435.

22. N. Q. Minh, T.T., ed. *Science and Technology of Ceramic Fuel Cells*. 1995, Elsevier: Amsterdam.

23. Tuller, H.L. and A.S. Nowick, *Doped Ceria as a Solid Oxide Electrolyte.* Journal of the Electrochemical Society, 1975. 122(2): p. 255-259.

24. Balazs, G.B. and R.S. Glass, *Ac-Impedance Studies of Rare-Earth-Oxide Doped Ceria.* Solid State Ionics, 1995. 76(1-2): p. 155-162.

25. Dudek, M., *Ceramic oxide electrolytes based on CeO2-Preparation, properties and possibility of application to electrochemical devices*. Journal of the European Ceramic Society, 2008. 28(5): p. 965-971.

26. Ishihara, T., H. Matsuda, and Y. Takita, *Effects of Rare-Earth Cations Doped for La Site on the Oxide Ionic-Conductivity of $LaGaO_{3-\delta}$ Based Perovskite-Type Oxide*. Solid State Ionics, 1995. 79: p. 147-151.

27. Shujun Li, L.G., Haitao Gu, et, al, *Sinterability and electrical properties of ZnO-doped $Ce_{0.8}Y_{0.2}O_{1.9}$ electrolytes prepared by an EDTA–citrate complexing method*. Journal of Alloys and Compounds, 2011. 509.

28. Yifeng Zheng, L.W., Haitao Gu, et al, *The effects of Sr on the properties of Y-doped ceria electrolyte for IT-SOFCs.* Journal of Alloys and Compounds, 2009. 486.

29. Van herle, J., et al., *Sintering behaviour and ionic conductivity of yttria-doped ceria.* Journal of the European Ceramic Society, 1996. 16(9): p. 961-973.

30. A.N.VIRKAR, H.S.M., *OXYGEN ION CONDUCTION IN PURE AND YTTRIA-DOPED BARIUM CERATE*. Journal of Power Sources, 1985. 14.

31. Oishi, M., et al., *Defect structure analysis of B-site doped perovskite-type proton conducting oxide $BaCeO_3$: Part 2: The electrical conductivity and diffusion coefficient of $BaCe_{0.9}Y_{0.1}O_{3-\delta}$*. Solid State Ionics, 2008. 179(39): p. 2240-2247.

32. X.F. Guan, H.P.Z., Y.N. Wang, J. Zhang, *Preparation and properties of Gd^{3+} and Y^{3+} co-doped ceria-based electrolytes for intermediate temperature solid oxide fuel cells*. Journal of Alloys and Compounds, 2008. 464.

33. J.M.Smith, H.C.V.N., M.M.Abbott, *Introduction to chemical engineering thermodynamics*. 7 ed. 2005, New York: McGraw-Hill. 493.

Chapter 3 Mathematic modeling of dual membrane: Part 2 effective conductivity

3.1. Binary Composite Central Membrane

Anticipated phenomenon in central membrane of IDEAL cell is supposed to consist of mass transfers (e.g. charged proton defects and oxygen ions) and recombination between protons and oxygen ions. In order to achieve high performance of CM, the experiences from fabricating electrodes suggest that as many as effective reactive sites together with sufficient porosity are required. The reactive sites are demonstrated in study of electrodes as three phase boundary which in CM is constituted by intersections among protonic conducting phase (shorted as PCP), anionic conducting phase (shorted as ACP) as well as void phase, where TPB length geometrically depicted as the perimeter of contact area between PCP and ACP (see Figure 3.1) is described quantitively for reaction sites. The longer TPB length formed during sintering process, the larger reactive sites could be expected leading to lower polarization resistance.

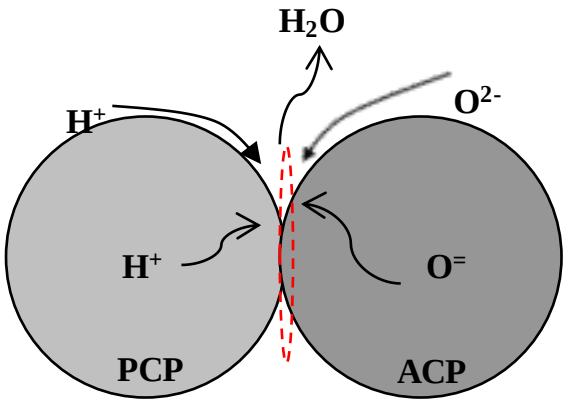

Fig. 3.1 Geometrical picture of reactive site (TPB) formed in CM

Nevertheless, to guarantee that protons meet with oxygen ions successfully at TPBs, non-interrupted conducting paths for both species from one extreme of electrolyte to reactive sites are the prerequisites. Figure 3.2 presents a cross sectional picture of dual membrane with two dense electrolytes placed on both sides and porous CM in the middle,

where black spheres represent protonic conducting particles (shorted as PCPs) while grey spheres are denoted to anionic conducting particles (shorted as ACPs). The potential conducting paths are emphasized by black curve arrows for ACPs and white curve arrows for PCPs.

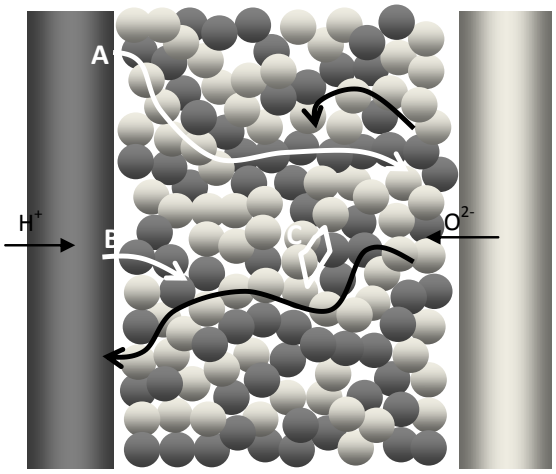

Fig. 3.2 Conducting paths in porous CM with randomly distributed PCPs (black spheres), ACPs (grey spheres) and pores (voids between PCPs and ACPs)

The conducting paths in CM are strongly influenced by morphology of membrane which is summarized as porosity, grain sizes and volume fractions of PCP and ACP respectively. To simplify the mathematical description of morphology, some characteristic aspects are summarized as follows:

a) All PCPs and ACPs are considered as rigid spheres although in reality flake like, plate like, needle like or any irregular shape particles might exist;

b) PCPs and ACPs are randomly distributed through membrane without any regularity;

c) Three types of connecting network by either PCPs or ACPs could be concluded: a fully connection by PCP or ACP from one extreme to the other extreme of CM is called A-cluster or percolating cluster, a half connection attached to only one extreme is named B-cluster, the one absolutely isolated from both extremes is belonged to C-cluster;

d) Tortuous conducting paths are observed, the effective (or apparent) conductivity which is the reciprocal of resistivity) is related with conducting path:

$$\frac{\sigma^0}{\sigma^{eff}} = \frac{L_{path}}{L_m} = \tau \tag{3.1}$$

Where σ^0 denote the conductivity of dense electrolyte, L_m is the thickness of membrane while L_{path} is the actual length of flow path. The ratio $L_{path,i}/ L_m$ is namely tortuosity τ which is normally larger than 1 and varies with morphologies of CM. Many researchers studied this tortuosity (linked with effective conductivities) of composite electrode based on percolation theory[1], which is a general mathematical theory of connectivity and transport in geometrically complex systems (in SOFCs binary system or at most ternary system if voids included). As mentioned, A-cluster is a percolating cluster which is twisted formed by same type of particles. All particles within this connection are potentially considered to be reactive sites as long as the other conducting specie successfully arrives at any site of this connected network. Hence, it is believed that A-cluster plays a predominant contribution to effective conductivity in the case of large ratio of membrane thickness to particle sizes which is normally the reality in composite electrodes where thickness is on order of 100μm and particle size is on order of 0.1-1μm. Additionally, in case of small ratio of membrane thickness to particle sizes, S.Sunde[2] found that the contribution of B-cluster outside the percolation thresholds decreased the polarization resistance as opposed to concerns on A-cluster only. The presences of C-cluster almost takes no effect on the conduction due to no ions could be transferred into C-cluster. Before entering mathematic description of these three clusters in composite membrane, we first introduce basic parameters which are involved in description:

1) Coordination number Z_i: the average particle numbers surrounding *i* particles. For binary mixtures, if the surround particles are belonged to same specie *i*, the coordination number can be written as Z_{ii}. If the surround particles are belonged to the other specie j, the coordination number is written as Z_{ij}. Apparently, $Z_i = Z_{ii} + Z_{ij}$.

2) Number fraction n_i: the ratio of specie i numbers to total particle numbers, $n_i + n_j = 1$ for binary mixtures.

3) Volume fraction Φ_i: the ratio of total volume of specie i to total volume which can be related with number fractions and radii: $\Phi_i = n_i r_i^3/(n_i r_i^3 + n_j r_j^3)$

Percolation theory proposes that the probability of A cluster could be formed during random packing system is a function of coordination number:

$$p_i = [1-(\frac{\alpha - Z_{ii}}{\beta})]^{\gamma} \tag{3.2}$$

Where α, β and γ are adjustable parameters without physical meanings. The values of these parameters are obtained from empirical fitting experimental data or discrete element modeling of microstructures. The expressions of coordination number could be found from Many papers [3-6] correlating its value with number fraction or volume fraction and particle radii among composite materials. In this thesis, we are applying the latest developed model from D.Chen [4] who provided a comprehensive expressions for coordination number which are written as follows:

$$Z_{ii} = S_i N_{ii} \tag{3.3}$$

$$S_i = \frac{\phi_i / r_i}{\phi_i / r_i + \phi_j / r_j} = \frac{\phi_i}{\phi_i + \phi_j P} \tag{3.4}$$

$$N_{ii} = Z \tag{3.5}$$

Where P is the particle radii ratio r_i/r_j, N_{ii} is the average contact number between *i* particles in a particular idealized medium[6] which is equal to average coordination number *Z* through composite membrane. From these equations, we can derive a general picture of coordination number as a function of volume fractions and particle radii.

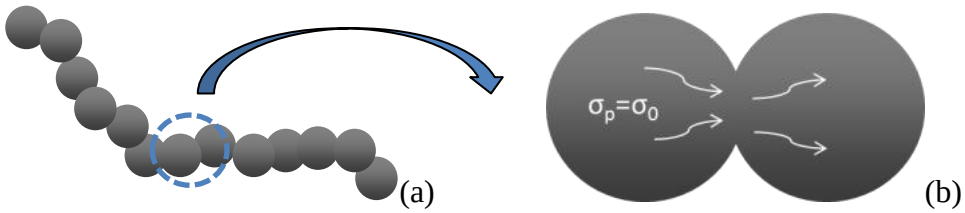

Fig. 3.3 Continuum medium approach: a) tortuous conducting particles formed in CM, b) uniform conducting medium through two adjacent particles in same type

$$\frac{\sigma^{eff}}{\sigma^{0}} = [(1-\phi_g)\psi_i p_i]^{\mu} \tag{3.6}$$

$$p_i = [1-(\frac{3.764 - Z_{ii}}{2})]^{0.4} \tag{3.7}$$

From equations 3.6 and 3.7, the normalized effective conductivity as a ratio of effective conductivity of one single conducting phase to the one in fully dense phase is analytically expressed against volume fraction ψ in Figure 3.4. This calculation has already contained the effect of porosity (Figure 3.4a) and particle radii ratio (Figure 3.4b) into conductivities. Since this calculation is based on percolation theory which considers the percolation threshold at 0.33 volume fraction of *i* particles in binary system, the results provided are also from thresholds. In other words, if volume fraction of *i* particles (e.g. PCPs) is only 0.2, it is basically believed that all PCPs have been isolated in binary system correspondingly to no contribution of protonic conduction is expected from *i* particles. Conversely, if volume fraction of *i* particles is superior to 0.7, it is also expected from percolation theory that all *j* particles (e.g. ACPs) in system would be isolated from oxygen ion conduction.

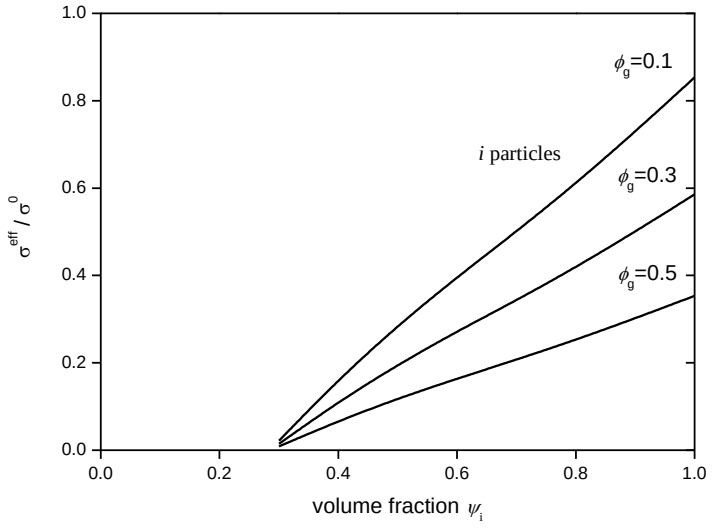

(a)

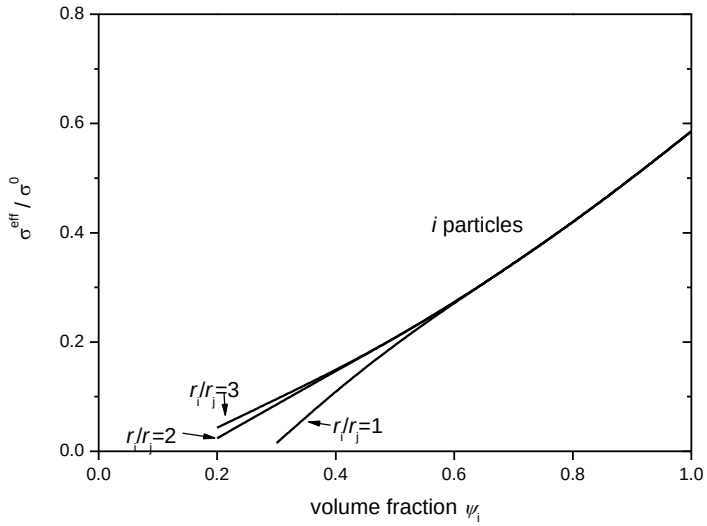

(b)

Fig. 3.4 Normalized effective conductivities of i particles as a function of volume fraction and (a) porosity and (b) particle radii ratio

On one hand, sufficient porosity in CM is the guarantee for successfully evacuation of water without significant influence on water formation reaction. On the other hand, large porosity brings problems of relative effective conductivity and mechanical stability of CM. The optimum porosity should be determined from the effect of water pressure accumulated correlating to the ratio of diffusion rate and reaction rate in CM. Figure 3.4b also provided the effect of particle radii ratio on conductivity, in which higher radii ratio (r_i/r_j) benefits effective conductivity of *i* particles near its percolation threshold. However, electrical conductivity improvement of *i* particles definitely causes decreasing electrical conductivity of the other particle species. In general, higher radii ratio (r_i/r_j) could be realized if $\sigma_i<\sigma_j$. Otherwise, it is not judicious to applying such morphology to fabricate CM. As demonstrated in Chapter 2, proton conductivity in BCY at 600℃ is 0.017 S/cm which is close to oxygen ion conductivity in YDC(0.016S/cm at same temperature). The proofs of concept IDEAL cells were fabricated with 50%BCY: 50%YDC plus a porosity of 30%-50%. For this kind of CM, expected effective conductivity of BCY and YDC could be 0.002-0.003 S/cm (0.12 proportion of dense electrolyte).

From above calculation, it is also indicated that normalized effective conductivity is only morphologically dependent. In other words, as morphology of binary system is same, no matter what kind of material and at what scale of temperature applied, normalized effective conductivity have a fixed value. This relation is true or close to fact when one considers electronic conduction or ionic conduction at high temperature (e.g. oxygen ion conduction in cathode above 800℃). When one deals with the situation that both proton and oxygen ion conduction are simultaneously present in porous CM at intermediate temperature ranges (500-700℃), one non-ignorable phenomenon that grain boundary blocking effect on ionic conduction should be taken into account. Since many cases proved that effective conductivity has temperature dependent behavior which could be significant in coarsely sintered porous binary composites.

3.2. Grain boundary effect

As introduced, above mentioned calculations are valid for inter particles which are actually electronic conductors or ionic conductors at high temperatures (e.g. above 800℃). When considering the case of ionic conduction below 800℃, grain boundary effect on the conductivity becomes non-ignorable factor. In a geometrical definition, grain boundary refers to a small contact area between two particles in same type (see Figure 3.5b). While in an electrical definition, electrical property in grain boundary is different from the one in bulk, which is dependent on external conditions such as temperature and atmospheres.

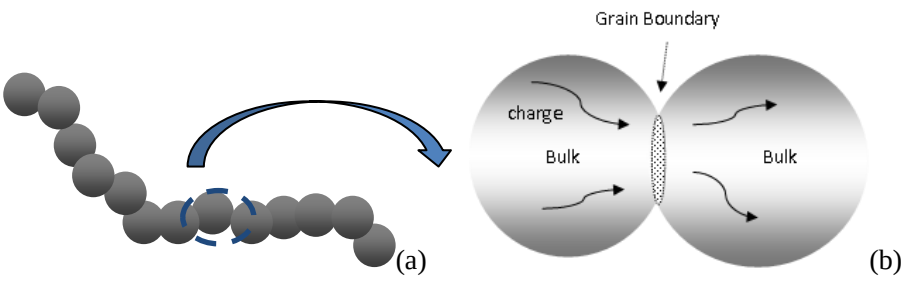

Fig. 3.5 non-continuum medium approach: a) tortuous conducting particles formed in CM, b) non-uniform conducting medium due to presence of grain boundary between two adjacent particles in same type

The possible reasons of forming grain boundary block effect on electrical conductivity on one hand might be attributed to 1) external effect: secondary phase or impurity phase (e.g.

siliceous phase) aggregation at intergranular boundary; 2) internal effect such as presence of charge space layer and grain boundary core at intergranular boundary which is believed as the essence of blocking effect. From geometric point of view, the internal effect of blocking resistance could be schematically showed in Figure 3.6a, which provides a simplified picture of charged species transporting through intergranular boundary of two adjacent particles. Rectangular are presenting bulk particle while in the middle the small channel represents the connecting neck formed during sintering. In a stead state of current flow, relative narrow neck behaves additional resistance to current flow, the process of which resembles somewhat fluid flow through an abrupt narrow channel. According to Navie-Stokes equation, the pressure of fluid is expected to increase in narrow channel under steady state flow. However, in the case of charged species transportation, the uprising resistance is embodied as the potential increasing which is schematically drawn in the Figure 3.6b.

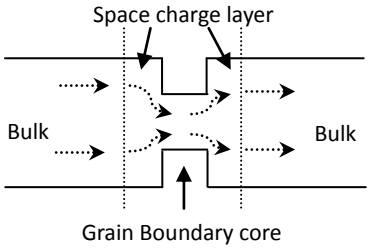

(a)

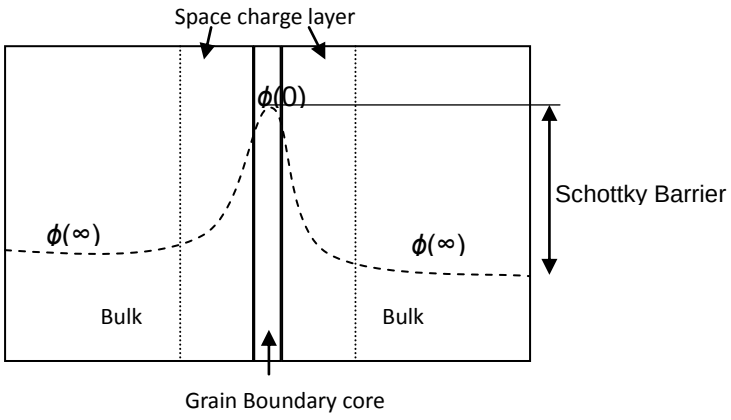

(b)

Fig. 3.6 Schematic picture of potential profile caused by grain boundary effect

In electrical point of view, potential of charged species start to increases from space charge layer which is actually a transition zone between bulk and grain boundary core. Consequently, generalized grain boundary consists of two space charge layers and one grain boundary core. The more detailed introductions about space charge layer and grain boundary can be found in references [7-10]. As demonstration by this charge space-grain boundary core theory, concentration of charged species sharply drops in charge space layer and reaches minimum in grain boundary core which leads to uprising of electrostatic potential ϕ in grain boundary (see Figure 3.6b). The difference between maximum potential $\phi(0)$ in grain boundary core and potential in bulk $\phi(\infty)$ is called Schottky Barrier, which is the intrinsic reason of grain boundary blocking effect. To mathematical derive the relationship of this potential increasing with conditions such as geometry, temperature and atmospheres, the electrochemical potential of charged species η_j as a function of concentration and electrostatic potential is expressed in equation 3.8 :

$$\eta_j(x) = \mu_j^0 + k_B T \ln C_j(x) + z_j e \phi_j(x) \tag{3.8}$$

Where μ_j is standard chemical potential, C_j is concentration of charged species j, z_j is carried charge number, ϕ_j is the electrostatic potential. In a steady state condition, electrochemical potential near grain boundary zone has following conservation:

$$\eta_j(0) = \eta_j(x) = \eta_j(\infty) \tag{3.9}$$

Where $\eta_j(0)$ and $\eta_j(\infty)$ denotes the electrochemical potential at grain boundary core and bulk respectively. If particle radius R is far larger than grain boundary thickness δ_{gb} which approximates to space charge width λ^*, it is sound to consider the position of bulk as infinitive. From the equation 3.9, it is possible to derive the expression of concentration as follows:

$$z_j e(\phi_j(x) - \phi_j(\infty)) = k_B T \ln \frac{C_j(\infty)}{C_j(x)} \tag{3.10}$$

Where electrostatic potential ϕ_j has a Poisson distribution form related with concentration as follows:

$$\frac{d^2(\phi_j(x)-\phi_j(\infty))}{dx^2} = -\frac{1}{\varepsilon}Q(x) = \frac{e}{\varepsilon}C_j(x) \tag{3.11}$$

Where ε is dielectric constant, Q(x) is the charge density. Constraints about this equation are expressed as:

$$\begin{aligned} &\phi_j(0)-\phi_j(\infty) = \text{const} \\ &\frac{d(\phi_j(0)-\phi_j(\infty))}{dx}\Big|_{\infty} = 0 \end{aligned} \tag{3.12}$$

By combining equation 3.11 with 3.12, the analytical solution of concentration is expressed as followings:

$$\begin{aligned} &0 \le x \le \lambda^* : C_j(x) = C_j(\infty)\exp\left[-\frac{z_j}{4}\left(\frac{x-\lambda^*}{L_D}\right)^2\right] \\ &\lambda^* \le x \le R: \quad C_j(x) = C_j(\infty) \end{aligned} \tag{3.13}$$

Where L_D and λ^* are characteristic lengths defined as Debye length[11] and space charge layer width expressed as follows, respectively:

$$L_D = \left(\frac{k_B T\varepsilon}{2e^2 C_j(\infty)}\right)^{\frac{1}{2}} \tag{3.14}$$

$$\lambda^* = 2L_D\left(\frac{e(\phi(0)-\phi(\infty))}{k_B T}\right)^{\frac{1}{2}} \tag{3.15}$$

Debye length L_D, in addition to materials, is related with temperature (because ε is a temperature dependent parameter) and concentration. Although high T enlarges Debye length, it also enhances gas incorporation ability to produce higher concentration of charged species. Hence, Debye length L_D varies very little with temperature and is on the magnitude of nanometer. However, space charge width λ^*, on the order of nanometer or tens of nanometers, relies much more on temperatures. According to Nernst-Einstein equation, conductivity of charged species is related to its concentration and diffusivity as:

$$0 \le x \le \lambda^* : \sigma_{sc} = \frac{z_j^2 F^2 D_j C_j(x)}{R_g T}$$
$$\lambda^* \le x \le R : \sigma_b = \frac{z_j^2 F^2 D_j C_j(\infty)}{R_g T} \tag{3.16}$$

As discussed in Chapter 2, bulk concentration of charged species is dependent on material, dopant concentration, temperature and atmospheres. Therefore, bulk conductivity is constant as those conditions are fixed. While the conductivity in space charge layer varies locally with concentration which is as a function of distance to grain boundary core. Under these description by grain boundary theory, overall Ohmic resistance R_t per single particle is attributed to two aspects: bulk resistance R_b, and grain boundary resistance R_{gb} (including space charge layer and grain boundary core), which can be directly obtained from the impedance results[12]:

$$R_t = R_b + R_{gb} \tag{3.17}$$

Each resistance is an integral of geometry as following equations:

$$\begin{aligned} R_b &= \int_{\lambda^*}^{R\cos\theta} \frac{dx}{\sigma_b \pi (R + R\cos\theta - x)(R - R\cos\theta + x)} \\ &= \frac{1}{2\pi R \sigma_b} \ln \frac{R + R\cos\theta - \lambda^*}{R - R\cos\theta + \lambda^*} \end{aligned} \tag{3.18}$$

$$\begin{aligned} R_{gb} &= \int_0^{\lambda^*} \frac{dx}{\sigma_{sc} \pi (R + R\cos\theta - x)(R - R\cos\theta + x)} \\ &= \frac{1}{\sigma_b} \int_0^{\lambda^*} \frac{dx}{\exp(-\frac{z_j}{4}(\frac{x-\lambda^*}{L_D})^2)\pi (R + R\cos\theta - x)(R - R\cos\theta + x)} \end{aligned} \tag{3.19}$$

$$\begin{aligned} \sigma_{gb} &= \frac{\lambda^*}{R_{gb} \pi R^2 \sin^2\theta} \\ &= \sigma_b \frac{\lambda^*}{\pi R^2 \sin^2\theta \int_0^{\lambda^*} \frac{dx}{\exp(-\frac{z_j}{4}(\frac{x-\lambda^*}{L_D})^2)\pi (R + R\cos\theta - x)(R - R\cos\theta + x)}} \end{aligned} \tag{3.20}$$

It is apparent that the ratio of grain boundary conductivity with bulk conductivity is related not only with Schottky Barrier $\Delta\phi(0)$ which is mainly as a function of temperature, but also

with grain size and contact angle. As grain radius R is far larger than space charge width λ^*(typically R exceeds 0.5 μm), the ratio of two conductivities is irrelevant with R and can be simplified to an approximation relation with Schottky Barrier $\Delta\phi(0)$ [13, 14]:

$$\frac{\sigma_{gb}}{\sigma_b} \approx \frac{2z_j e\Delta\phi(0)/k_B T}{\exp(z_j e\Delta\phi(0)/k_B T)} \tag{3.21}$$

Moreover, the effective conductivity per unit particle (containing contributions from both bulk and grain boundary) is written as a function of total particle resistance as follows:

$$\begin{aligned}\sigma^{eff} &= \frac{1}{R_t}\int_0^{R\cos\theta} \frac{dx}{\pi(R+R\cos\theta-x)(R-R\cos\theta+x)} \\ &= \frac{1}{2\pi RR_t}\ln\frac{R+R\cos\theta}{R-R\cos\theta} = \frac{1}{2\pi R(R_b+R_{gb})}\ln\frac{R+R\cos\theta}{R-R\cos\theta}\end{aligned} \tag{3.22}$$

3.3. Validation on dense electrolytes

First of all, contact angle between ionic contactor is a critical parameter for us to estimate the grain boundary conductivity. To acquire this information, we refer to the calculation results of densification of powder compact by Y.Hirata [15] who developed a numeric relations of contact angle in the terms of particle size and coordination number. One of his main conclusions on the relations of these parameters is presented in Figure 3.8.

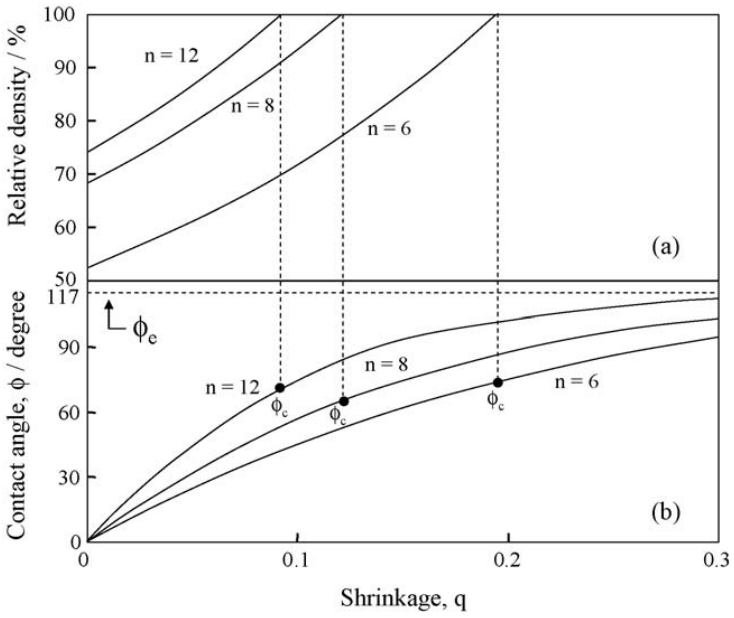

Fig.3.8 (a) Relative density of powder compacts for coordination number n = 6–12 as a function of shrinkage q, (b) The relation between contact angle ϕ and shrinkage q. Taken from Y. Hirata[15]

In the case of coordination number between 6-12 which is the fact for most compact systems (i.e. dense electrolyte), the average contact angel between two contacting particles in fully dense electrolyte (theoretical relative density is 100%, while in reality as relative density is larger than 95% it is reasonable to consider it as dense layer) could be expected to be around 32^{o}-36^{o} (the contact angle ϕ from Y.Hirata' paper is twice of our so called contact angle θ). Theoretical model provides us a basic guideline to estimate the ranges of contact angle. Due to the distribution of grain size in a real sample, the contact angle also has an extension which is presented by our statistic of contact angles by counting them one by one in Figure 3.9 and table 3.1.

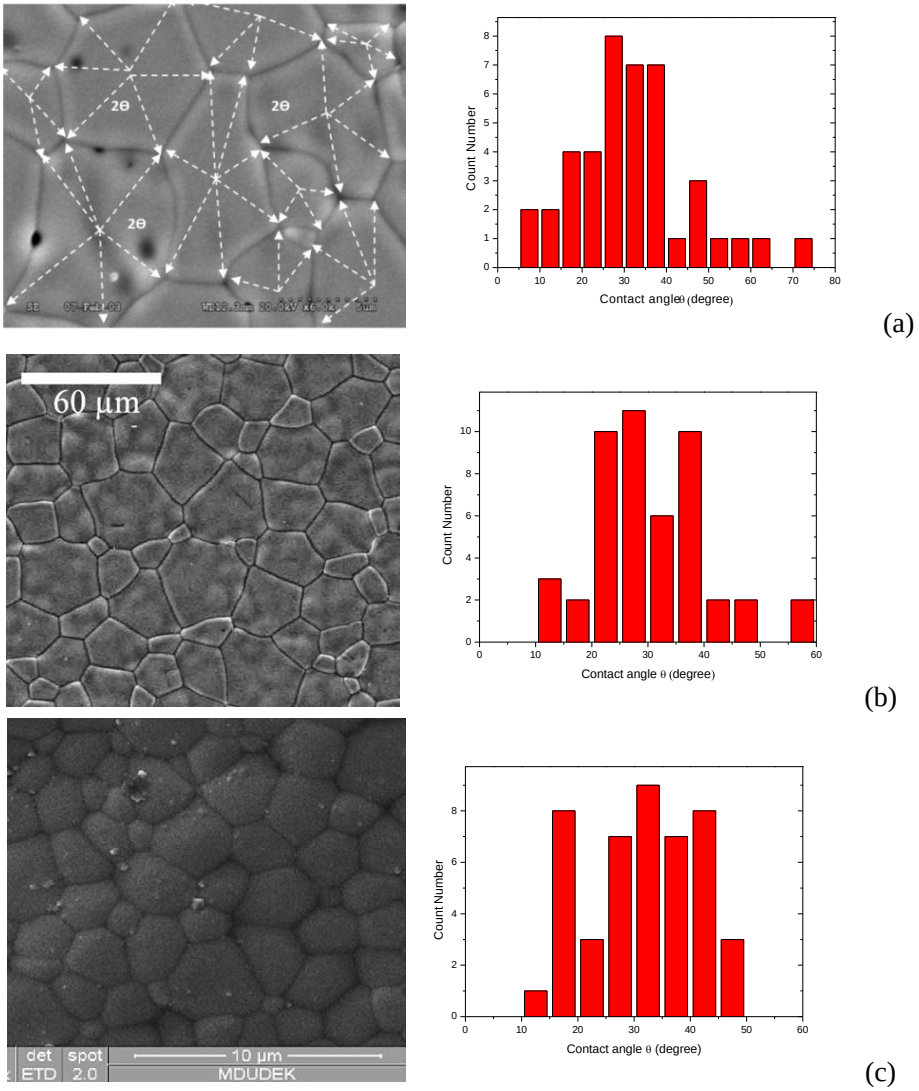

Fig. 3.9 Statistics count of contact angles from SEM images of typical dense ionic conducting electrolytes, more detailed information are listed in table 1

Table 3.1 material properties and mean contact angle counted from samples

Material	Relative density	Grain size (μm)	Contact angle θ (Standard Deviation)	Source
a) SDC	95.8%	3-7	31 (±13)	[16]
b) BCY	99.2%	5-36	30 (±9.7)	[17]
c) SDC	>97%	1-4	31 (±9.5)	[18]

The statistic results provided in table 3.1 reveal a fact that average contact angle in dense electrolyte is irrelevant with grain size and material which has an average value at around 30^o. It is quite close to theoretical value of $32\text{-}36^o$ obtained from Figure 3.8. For the sake of calculating effective conductivity and grain boundary resistance, it is necessary to state following assumptions in model:

a) Effective conductivity and grain boundary resistance are calculated on the basis of rigid spheres. We consider mono-contact angle distribution in either dense electrolyte or porous CM;

b) Grain boundary effect of only grain to grain contact (i.e. perpendicular to current flow) is taken into account, although limited effect of parallel grain boundary effect has also been mentioned by X.Guo's model[19];

c) Electronic accumulation at grain boundary is also not taken into account, which may be important in ceria when it is exposed to low oxygen pressure.

Since we don't know exact relations of Schottky Barrier $\Delta\phi(0)$ with temperature, we choose Schottky Barrier $\Delta\phi(0)$ as a variable to show how this variable affect the ratio of grain boundary conductivity with bulk conductivity in Figure 3.10, which provides us a legible picture of grain boundary effect under different temperatures and charged species (proton and oxygen ion). When the ratio approaches to unit, it indicates the disappearance of grain boundary effect. Generally speaking, grain boundary effect is more severe in oxygen ion conduction than proton conduction due to i) oxygen ion carries bi-valence compared to

mono-valence of proton, ii) oxygen ion carrier is oxygen vacancy which is depleted in space charge layer, but partial proton transport is via oxygen vacancy.

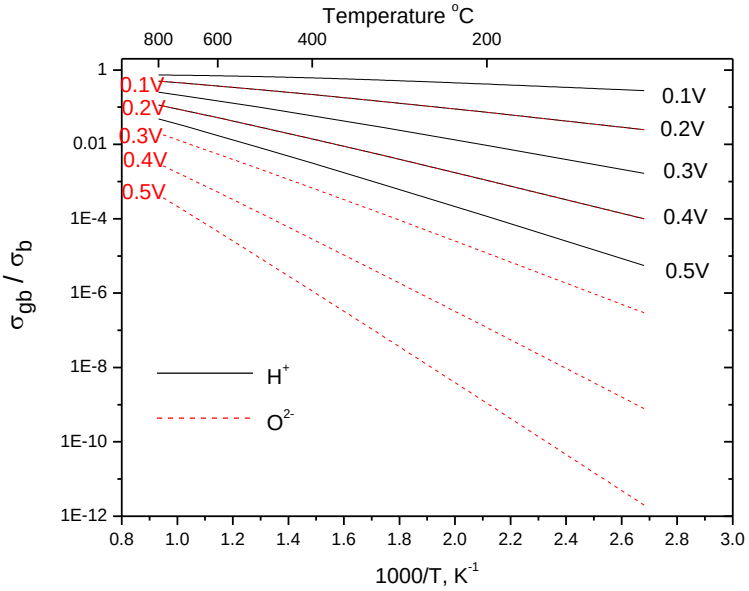

Fig. 3.10 Ratio of grain boundary conductivity to bulk conductivity as a function of temperatures

Figure 3.10 also gives us the clear picture that even for same material at high temperature (e.g. 800℃), grain boundary conductivity might still be 1 to 2 orders lower than bulk conductivity for ionic conduction. We are also aware that $\Delta\phi(0)$ varies with temperature, of which three ionic electrolytes: BZY, YDC and YSZ are presented in Figure 3.11. For oxygen ion conductions at low temperature ranges (below 500℃), the $\Delta\phi(0)$ increases with temperature rises. In fact, at high temperature ranges (e.g. above 800℃), the $\Delta\phi(0)$ is expected to drop sharply due to high diffusivity of oxygen ion. However, this drop is not experimentally observable since intercepts of grain boundary resistance in impedance plots are too small to discern.

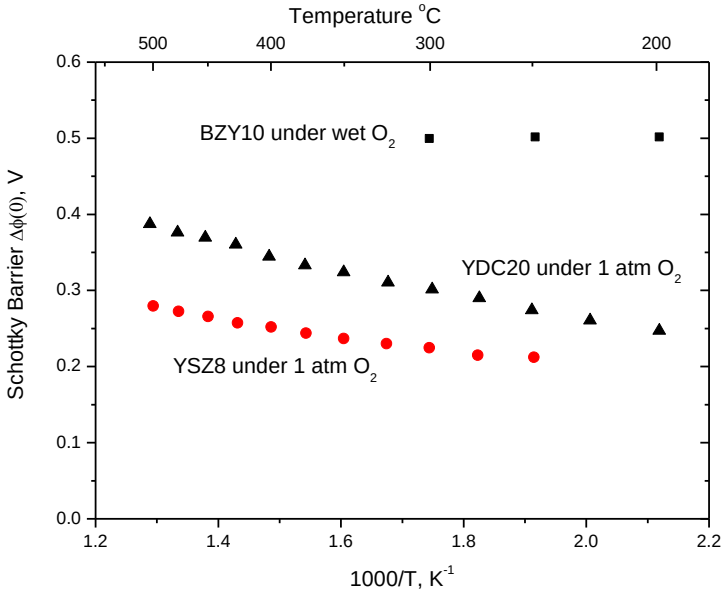

Fig. 3.11 Schottky Barrier of YDC20[20], YSZ8[19] and BYZ10[21] as a function of temperatures

For the application of space charge - grain boundary core theory into systems, available data on grain boundary conductivity and bulk conductivity of BCY10 and BCY20 have been used. As it is expected, high doped material (BCY20) exhibits relatively higher grain boundary conductivity due to its higher oxygen vacancy concentrations created. The Apparent Schottky Barrier $\Delta\phi(0)$ of both materials decrease as temperature is above 350℃. The difference is transparently observed below 350℃, where BCY20 has a small ascending curve with temperature. From Figure 3.12, it is applicable to estimate that grain boundary effects are almost diminished above 600℃.In case of BCY10, it is insufficient to judge the critical temperature where grain boundary disappears thoroughly since insufficient experimental data are provided. Nevertheless, we arbitrarily derived the Schottky Barrier potential of BCY10 between 400-600℃ according to the effective conductivity presented in Figure 3.13.

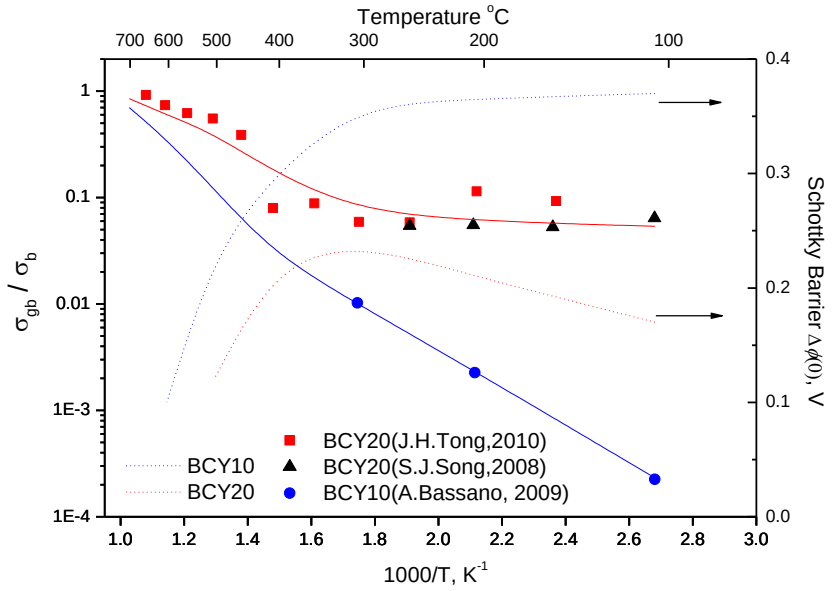

Fig. 3.12 Collection of ratio of grain boundary conductivity to bulk conductivity of BCY10[22] and BCY20[23, 24] as a function of temperatures, dots are calculated from measurements and fitted by smooth lines

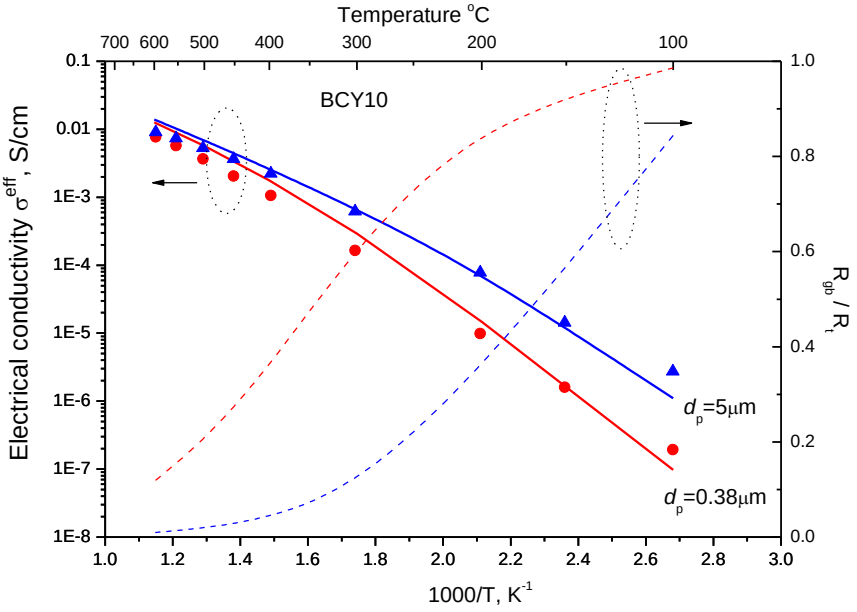

Fig. 3.13 Dependence of electrical conductivity of dense BCY10 on grain size 5 μm (blue) and 0.38 μm (red), dots are taken from Bassano[22], smooth lines are simulation results labeled with same color corresponding to same grain size

In Figure 3.13, we have evaluated the effective conductivity and grain boundary resistance of BCY10 under 2 different grain sizes: 5 μm and 0.38 μm respectively. Experimental data

about effective conductivities (dots in Figure 3.13) obtained from impedance results were validated with calculations (smooth lines) together with grain boundary resistances. Distinct differences of two samples emerges between 100-300℃, where grain boundary resistance counts for 50% of total resistance. Even for fine sintered electrolyte (5μm grain size), grain boundary effect is non-ignorable until temperature rises up to 600℃. Besides, effective conductivities of these two samples coincide above 600℃ indicating insignificant grain boundary effect at high temperature ranges. Theoretically speaking, grain boundary blocking effect should be more severe in oxygen ion conducting electrolytes. Since the material applied in dual membrane is yttrium doped ceria, we have collected some YDC samples with dopant concentration close to 15% in Figure 3.14. It is found that bulk conductivity of YDC under some dopant level keeps same activation energy E_a against temperatures (200-800℃). However, the grain boundary conductivities differ from samples (even for the same doping level) which are close related with their fabricating processes. And this difference could possibly be very high. For instance, results of grain boundary conductivities of YDC20 form Y.Zheng and X.Guo differentiate as large as 3 orders of magnitude.

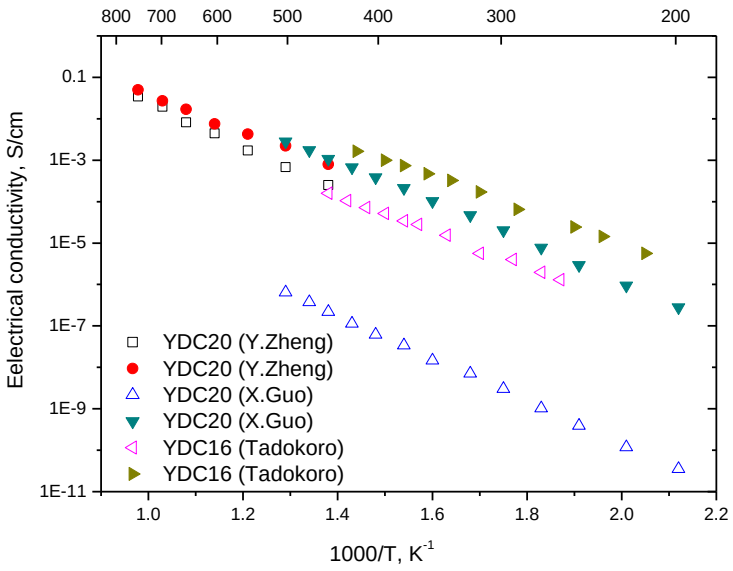

Fig. 3.14 Collection of bulk conductivity (solid symbols) and grain boundary conductivity (open symbols) of YDC [20, 25, 26] as a function of temperatures

This fact implies us that Schottky Barrier $\Delta\phi(0)$ should be considered as an apparent parameter which includes intrinsic effect and extinct effect (impurity and second phase). Among these two effects, we assume intrinsic effect is unchanged and charged species concentration satisfies equations 3.13. However, extinct effect is impossible to numerically quantify which might change with specific samples. For characterizing YDC15, samples from Van herle[27] were taken who provided effective conductivity and contribution of grain boundary resistance in Figure 15. Average grain size was estimated from SEM image which is around 0.7 microns. Contact angle as mentioned above is fixed at 30°, by fitting with effective conductivity (close dots in Figure 15), we obtained the $\Delta\phi(0)$ between 0.13-0.16V, based on which grain boundary resistance contribution was calculated and agreed very well with experiment results.

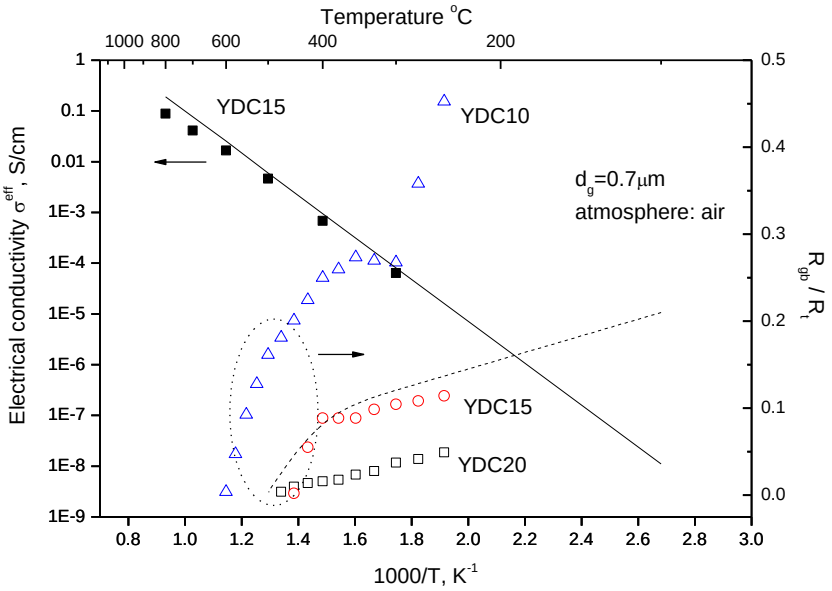

Fig. 3.15 Comparison of calculation results (smooth lines) with experimental data[27] on effective conductivity (solid symbols) and grain boundary resistance (open symbols) of YDC

3.4. Validation on Porous Electrolytes

In general sense, contact angles in porous membrane could potentially be ranging from 0 (i.e. point contact) - 30 (i.e. fully dense) which are difficult to measure and statistic count since irregular geometries of grains and necks are expected through porous membrane. However, it is commonly plausible to consider mean contact angle be smaller than 30°. For

the consideration of porous composite electrodes in conventional SOFCs, typical value frequently used in calculation is presumably set 15^{o}. The variance of contact angle in porous membrane is deemed to be only geometrical aspect as opposed to dense electrolytes due to more advanced processing techniques are required. The purpose of this paragraph is to introduce the concept that, in addition to tortuous conducting path in binary mixtures, how important role could be played on effective conductivity of ionic conductor by contact angle in porous membrane. Unfortunately, very few data from experiments about contact angle is available. First of all, by numeric calculating the effective conductivity and grain boundary resistance as a function of contact angle, we need to add extra following assumptions on the basis of previous ones:

a) Debye length L_D varies little with temperatures. In the processes of calculation, we fix L_D of BCY at 2nm and of YDC at 4 nm.

b) Schottky Barrier $\Delta\phi(0)$ is irrelevant with contact angles.

Figure 3.16 presents numeric calculation of effect by contact angle on electrical conductivities of BCY10 and YDC15 respectively. In these calculations, contact angles from 5^{o} to 30^{o} have been attempted. Schottky Barrier $\Delta\phi(0)$ were used by same values with the ones in dense electrolytes. For both samples, grain size independent bulk conductivities were also added to compare with effective conductivities. The more disparity between bulk conductivity and effective conductivity signifies more severe grain boundary effect existing. When this two conductivities overlap, it indicates elimination of grain boundary effect. From this understanding, critical temperature of eliminating grain boundary effect (grain boundary resistance approaches zero) for dense electrolytes ($\theta=30^{o}$) is around 600℃ for both BCY10 and YDC15. While for porous membrane (with typical $\theta=15^{o}$), critical temperature of eliminating grain boundary effect might reaches up close to 700℃. In the case of working temperature setting at 600℃, grain boundary resistance contributes about 6% and 8% to total resistance in BCY10 and YDC15 respectively. It is also interesting to notice that grain boundary resistances in BCY10 below 300℃ are irrelevant with contact angles and almost dominate total resistance. While for YDC15 electrolyte, contact angle plays a significant role on contribution percentage from grain boundary resistance ranging from

0.3-0.8. As temperature enters 300-600℃ ranges, grain boundary effect drops fast both in BCY10 and YDC15. In addition to temperature, contact angle is another crucial parameter for evaluating grain boundary effect. Taking BCY10 and YDC15 at 600℃ for instances, fine sintered grains($\theta=30^o$) can potentially exhibit more than 1 order higher ionic conductivity than coarsely sintered grains(small θ).

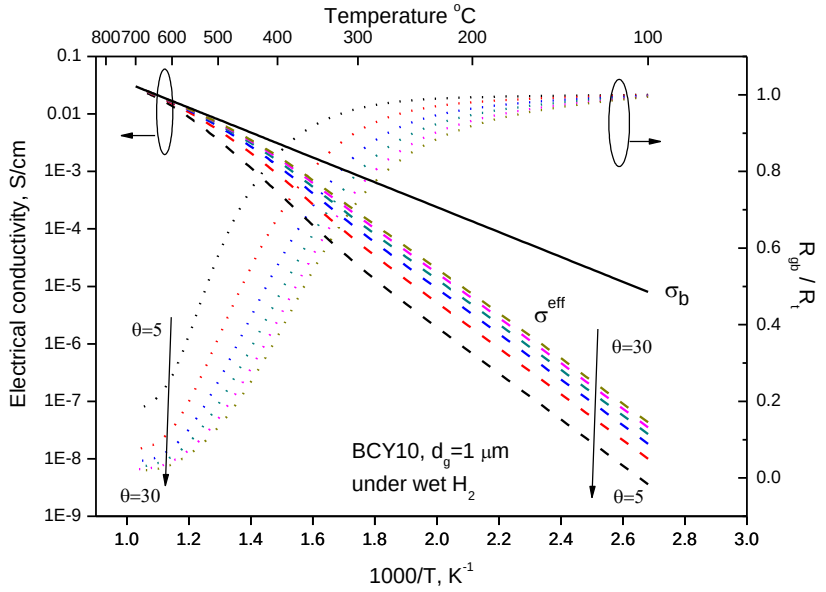

(a)

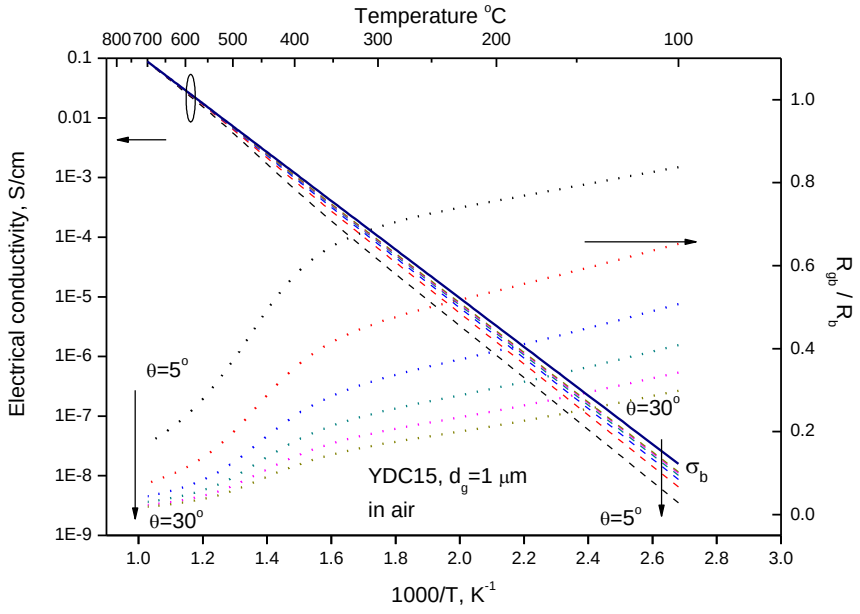

(b)

Fig. 3.16 Numerical calculation of effective ionic conductivity and grain boundary resistance in BCY10 (a) and YDC15 (b)

At last, we attempted to apply this grain boundary model in a real sample with porous membranes sample to validate its validity. In IDEAL cell project, two available CMs with 50%BCY15+50%YDC15 and porosities of 30% and 45% have been fabricated and measured by impedance spectroscopy. In order to characterize effective ionic conductivity in CM, low humidified H_2 atmosphere and air atmosphere were applied on two sides. The measurements under humidified low H_2 atmosphere fed could properly provide the effective protonic conductivity attributed by BCY15 due to almost protonic insulating property in YDC15. However, the measurements under oxygen atmosphere fed are impossible to deliver proper oxygen ion conductivity in YDC15 since oxygen ion could also be conducted in BCY15. Under these considerations, only protonic conductivity of BCY15 has been taken to validate. Instead of YDC, we chose another material-Samaria doped ceria (SDC) to study although SDC samples investigated were only porous membrane rather than porous composite membrane. As a consequence, ultimate effective protonic conductivity of BCY15 is expected to be from two aspects: i) tortuous conducting path in binary system, ii) grain boundary effect. While for the case of SDC, it is much simpler which it only requires to consider grain boundary effect in porous mono-system. Table 3.2 gives morphological data (including volume fraction, grain size, porosity and atmospheres) of materials we used.

Table 3.2 Morphological data of samples used in validations

Material	Contact angle	Volume fraction	Grain size	Porosity	Atmosphere	Ref
BCY15	Small	0.5	<0.5 μm	30%	Wet H_2	[28]
			<0.5 μm	45%		
SDC10	30^0	1	7 μm	4.2% dense	Air	[16]
	Small	1	<0.5 μm	51.2%		
	Large	1	1-2 μm	31.2%		
	Large	1	1-2 μm	39.7%		
	Large	1	1-2 μm	54.8%		

In the processes of validation, contact angles of BCY15samples with 30% porosity and 45% porosity have been found to be 15^o and 5^o respectively by fitting with experimental data. The former one is the typical value in porous membrane, but the latter one has a rather smaller contact angle resulting in extremely low total conductivity.

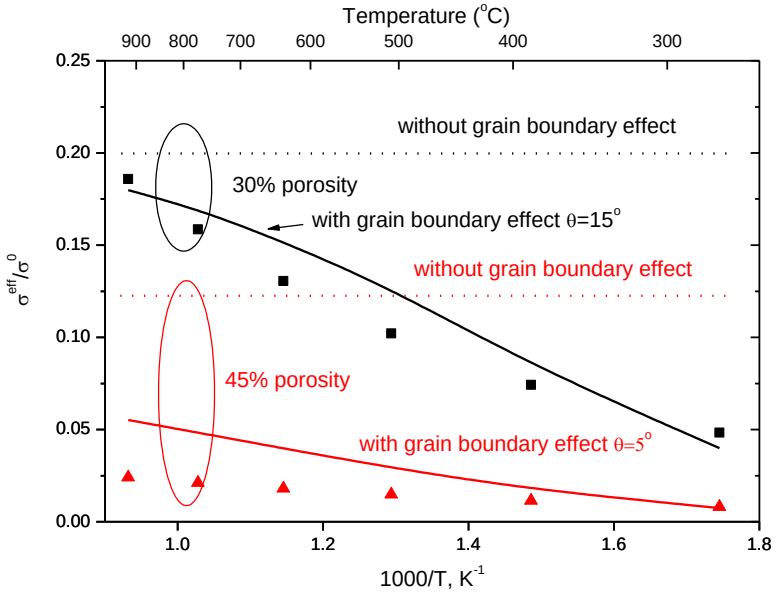

(a)

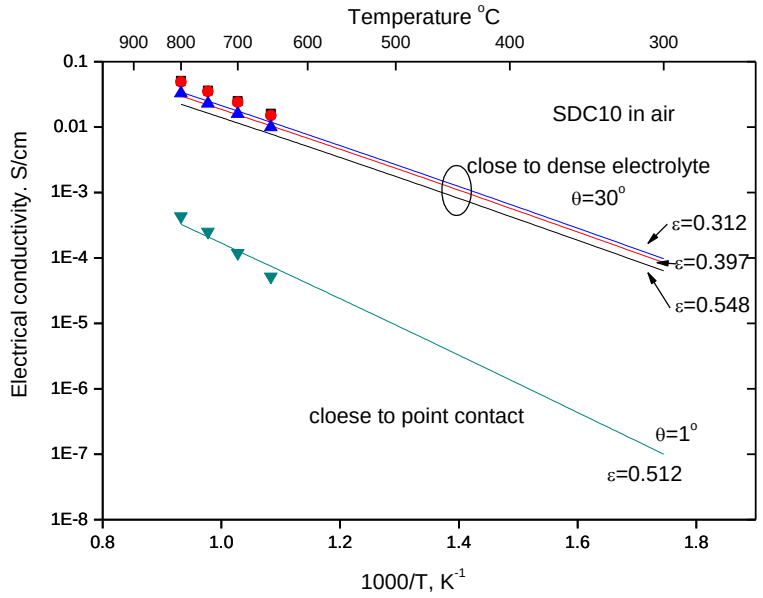

(b)

Fig. 3.17 Effective conductivities validation on BCY15 in porous composite CM (a) and SDC10 in porous membrane (b)

In addition, effective conductivities without grain boundary consideration were calculated by percolation theory and drawn (dot lines) in Figure 3.17a as well. Apparent temperature dependences of ratio of effective conductivity to pure conductivity in dense electrolyte have been observed. For the sample with 30% porosity, its effective conductivity approached to upper limit at 900℃where there is no grain boundary effect. However, for another sample with 45% porosity, grain boundary resistance dominated overall resistance through all temperature ranges. With respect to SDC10 samples, the first group of samples with fitted contact angle at 30^o were fabricated by special processing method in comparison with the sample with fitted contact angle $\theta=1^o$ fabricated by conventional method. Here we are attempting to pay more attention on the role of contact angle on effective conductivity without special attention on techniques. If intergranular necks are controlled very well (close to dense electrolyte), the effective conductivity is only reduced by voids. Nonetheless, if intergranular necks (contact angles) are not controlled well (as one of SDC sample fabricated by conventional method), extra drop of effective conductivity could possibly reach 3 orders of magnitude.

3.5. Conclusions

In this chapter, we discussed the effective conductivities of ionic conduction in either dense electrolyte or porous central membrane. For characterizing effective conductivities caused by tortuous percolating conducting path in random packing binary composites, percolation theory is an effective approach to apply and effective conductivity in CM for both BCY and YDC (with 0.5 volume fraction and porosity between 0.3-0.5) could be likely from 12% to 20% (e.g. 0.002-0.003 S/cm at 600℃) of pure conductivity in dense electrolyte at same temperatures.

Reduced effective ionic conductivity, in addition to a result of tortuous conducting path in binary composites, could also be attributed from grain boundary effect since fuel cell is aimed to operate at intermediate temperature ranges. The significance of intergranular boundary that is produced during powders sintering introduces grain boundary block effect to ionic conduction even in fully dense electrolyte at low temperatures due to heterogeneous

morphology exists at this boundary. The internal block effect of grain boundary can be mathematical described by space charge-grain boundary core model which relates the increasing resistance with geometry (grain size and contact angle) and atmospheres (bulk concentration). In general, the blocking effect level is simply summarized with following sequences:

i. Oxygen ion > proton;
ii. Low temperature > high temperature;
iii. Small grain size > large grain size;
iv. Small contact angle > large contact angle;
v. Low dopant concentration >high dopant concentration.

Validations of porous SDC samples demonstrate that controlling desired morphology (e.g. contact angle) in porous composite CM is crucial for realizing high performance IDEAL cell and certainly introduces challenges for material production. If grain boundary effect of ionic conduction can be successfully forbidden at 600℃, optimum effective protonic conductivity and oxygen ion conductivity in CM according to current knowledge (with 30% porosity and 0.5 volume fraction) are expected to be around 0.0034 S/cm.

Reference

1. Dietrich Stauffer, A.A., ed. *Introduction to percolation theory*. 2 ed. 1992, Taylor&Francis: London.

2. Sunde, S., *Monte Carlo simulations of polarization resistance of composite electrodes for solid oxide fuel cells*. Journal of The Electrochemical Society, 1996. **143**(6): p. 1930-1939.

3. Bouvard, D. and F.F. Lange, *Relation between percolation and particle coordination in binary powder mixtures.* Acta Metallurgica et Materialia, 1991. **39**(12): p. 3083-3090.

4. Chen, D., et al., *Percolation theory to predict effective properties of solid oxide fuel-cell composite electrodes*. Journal of Power Sources, 2009. **191**(2): p. 240-252.

5. Suzuki, M. and T. Oshima, *Estimation of the Co-ordination number in a Multi-Component Mixture of Spheres*. Powder Technology. **35**(2): p. 159-166.

6. Suzuki, M. and T. Oshima, *Comparison between the computer-simulated results and the model for estimating the co-ordination number in a three-component random mixture of spheres*. Powder Technology, 1985. **43**(1): p. 19-25.

7. Yan, M.F., R.M. Cannon, and H.K. Bowen, *Space-Charge Distributions near Interfaces during Kinetic Processes.* Journal of Applied Physics, 1983. **54**(2): p. 779-791.

8. Maier, J., *Space charge regions in solid two-phase systems and their conduction contribution--I. Conductance enhancement in the system ionic conductor-inert phase and application on AgC1:Al_2O_3 and AgC1:SiO_2*. Journal of Physics and Chemistry of Solids, 1985. **46**(3): p. 309-320.

9. Mukhopadhyay, S.M. and J.M. Blakely, *Ionic Double-Layers at the Surface of Magnesium-Doped Aluminum-Oxide - Effect on Segregation Properties.* Journal of the American Ceramic Society, 1991. **74**(1): p. 25-30.

10. Jiang, S. and J.B. Wagner, *A theoretical model for composite electrolytes--I. Space charge layer as a cause for charge-carrier enhancement*. Journal of Physics and Chemistry of Solids, 1995. **56**(8): p. 1101-1111.

11. Available from: http://en.wikipedia.org/wiki/Debye_length.

12. Vladikova, D. *THE TECHNIQUE OF THE DIFFERENTIAL IMPEDANCE ANALYSIS Part I: BASICS OF THE IMPEDANCE SPECTROSCOPY*. Advanced Techniques for Energy Sources Investigation and Testing. 2004. Sofia, Bulgaria.

13. Fleig, J., S. Rodewald, and J. Maier, *Microcontact impedance measurements of individual highly resistive grain boundaries: General aspects and application to acceptor-doped $SrTiO_3$*. Journal of Applied Physics, 2000. **87**(5): p. 2372-2381.

14. Guo, X. and J. Maier, *Grain boundary blocking effect in zirconia: A Schottky barrier analysis*. Journal of The Electrochemical Society, 2001. **148**(3): p. E121-E126.

15. Hirata, Y., A. Hara, and I.A. Aksay, *Thermodynamics of densification of powder compact*. Ceramics International, 2009. **35**(7): p. 2667-2674.

16. Zhao, F. and A.V. Virkar, *Effect of morphology and space charge on conduction through porous doped ceria*. Journal of Power Sources, 2010. **195**(19): p. 6268-6279.

17. Fu, X.-Z., et al., *Y-doped $BaCeO_{3-\delta}$ nanopowders as proton-conducting electrolyte materials for ethane fuel cells to co-generate ethylene and electricity*. Journal of Power Sources, 2010. **195**(9): p. 2659-2663.

18. Dudek, M., *Ceramic oxide electrolytes based on CeO2--Preparation, properties and possibility of application to electrochemical devices*. Journal of the European Ceramic Society, 2008. **28**(5): p. 965-971.

19. Guo, X. and R. Waser, *Electrical properties of the grain boundaries of oxygen ion conductors: Acceptor-doped zirconia and ceria*. Progress in Materials Science, 2006. **51**(2): p. 151-210.

20. Guo, X., W. Sigle, and J. Maier, *Blocking grain boundaries in yttria-doped and undoped ceria ceramics of high purity.* Journal of the American Ceramic Society, 2003. **86**(1): p. 77-87.

21. Kjølseth, C., et al., *Space-charge theory applied to the grain boundary impedance of proton conducting $BaZr_{0.9}Y_{0.1}O_{3-\alpha}$*. Solid State Ionics, 2010. **181**(5-7): p. 268-275.

22. Bassano, A., et al., *Synthesis of Y-doped $BaCeO_3$ nanopowders by a modified solid-state process and conductivity of dense fine-grained ceramics*. Solid State Ionics, 2009. **180**(2-3): p. 168-174.

23. Tong, J., et al., *Proton-conducting yttrium-doped barium cerate ceramics synthesized by a cost-effective solid-state reactive sintering method*. Solid State Ionics, 2010. **181**(33-34): p. 1486-1498.

24. Song, S.J., et al., *Space charge potential of proton conducting BaCe0.8Y0.2O2.9-delta.* Journal of Ceramic Processing Research, 2008. **9**(4): p. 376-380.

25. Yifeng Zheng, L.W., Haitao Gu, et al, *The effects of Sr on the properties of Y-doped ceria electrolyte for IT-SOFCs.* Journal of Alloys and Compounds, 2009. **486**.

26. Tadokoro, S.K., et al., *Synthesis, sintering and impedance spectroscopy of 8 mol% yttria-doped ceria solid electrolyte*. Journal of Power Sources, 2004. **130**(1-2): p. 15-21.

27. Van herle, J., et al., *Sintering behaviour and ionic conductivity of yttria-doped ceria.* Journal of the European Ceramic Society, 1996. **16**(9): p. 961-973.

28. THOREL, A., *mid-term report on IDEAL-Cell project*. 2009, ARMINES-Mines ParisTech.

Chapter 4 Mathematic modeling of dual membrane: Part 3 reaction kinetics

4.1. General Introduction

Mass transport phenomenon and transport coefficients have been analyzed in previous two chapters. We proceed in this chapter on mathematic modeling about kinetic recombination reaction in central membrane which appears in a new system (heterogeneous reaction in solid state phase at high temperature) that has never been investigated. In comparison with charge transfer reaction occurring in porous electrodes of conventional SOFCs, a group of similarities can be classified between them:

1) Type of phases of reactants and products involved in reactions: three general reactions in three different compartments of SOFCs are written in equations 4.1-4.3. No matter what type of reaction occurs, it always involves reactants and products from three phases: gas phase (H_2, O_2 and H_2O), electronic conducting phase (e^-) and ionic conducting phase (H^+ and O^{2-}). To point out, the presence of H^+ and O^{2-} simultaneously in reaction is separated into two solid phases due to its different carriers. This common feature indicates that sufficient pores are required for mass transport of gases, sufficient reaction sites (intersects of three phases) are demanded for adequate reactions.

Charge transfer reaction in cathode (PCFC):

$$2H^+(\text{ion}) + \frac{1}{2}O_2(\text{gas}) + 2e^-(\text{electron}) \Leftrightarrow H_2O(\text{gas}) \tag{4.1}$$

Charge transfer reaction in anode (ACFC):

$$H_2(\text{gas}) + O^{2-}(\text{ion}) \Leftrightarrow H_2O(\text{gas}) + 2e^-(\text{electron}) \tag{4.2}$$

Ionic recombination in CM (IDEAL cell):

$$2H^+(\text{proton}) + O^{2-}(\text{oxygen ion}) \Leftrightarrow H_2O(\text{gas}) \tag{4.3}$$

2) Driving force for all processes: Ionic and electronic transfer are easy to comprehend which are driven by potential gradient in solid phase. But for mass transfer of gas, it also consumes electrochemical potential as a result of namely concentration polarization. Figure 4.1 schematically shows a five layers IDEAL cell, among which a global potential distribution through five layers as driving force for all processes is anticipated.

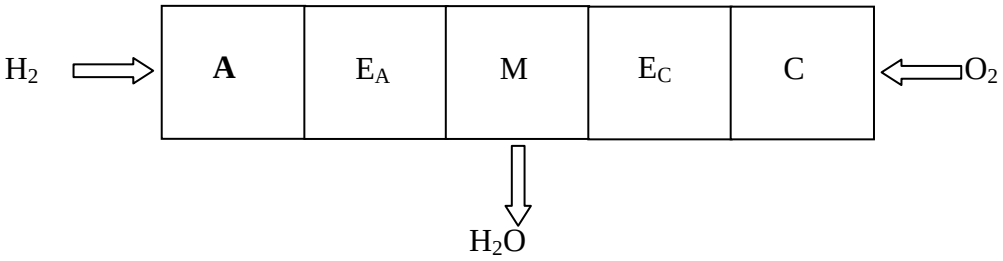

Fig. 4.1 The five-layer IDEAL-Cell: A: anode; E_A: anodic electrolyte; M: dual-phase membrane; E_C: cathodic electrolyte; C: cathode. These five layers share the same radius R but with different thickness δ_A, δ_{Ea}, δ_M, δ_{Ec} and δ_C, separately

Firstly, electric potential at cathode is deliberately defined to zero as comparative electric potential and correspondingly cell output voltage is equal to the potential difference between cathode and anode:

$$E_{cell} = \phi_A - \phi_C \tag{4.4}$$

Under an unpolarized IDEAL cell, three ladders of potential are expected in profile due to three reactions take place at interfaces of cathode/anionic electrolyte, anode/protonic electrolyte and at CM (see Figure 4.2a). Electric potential ϕ_{ACP} and ϕ_{PCP} are horizontal straight lines since no Ohmic losses in unpolarized condition, where the output cell voltage is nominated as open circuit voltage (OCV). Theoretical value of OCV for H_2 and O_2 feeding gases at 600℃ can be thermodynamically calculated which is around at 1.23 V (see Chapter 1).

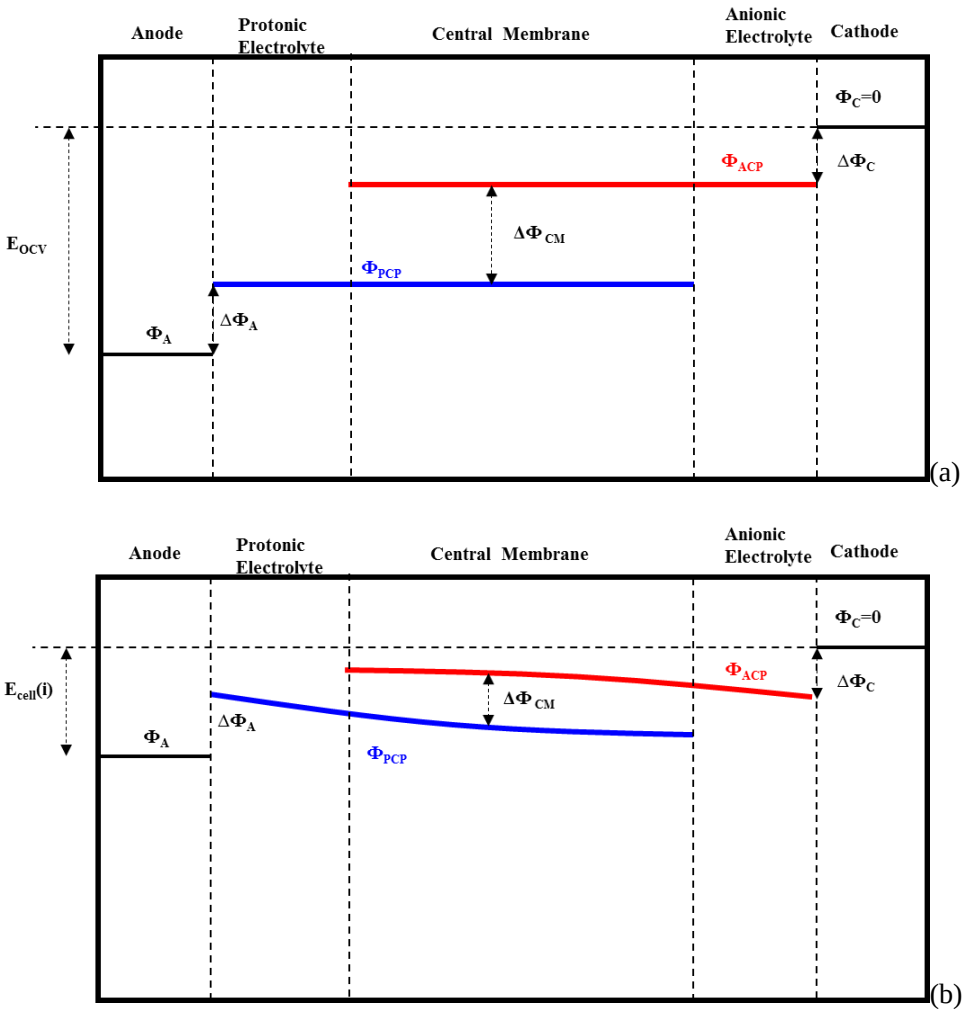

Fig. 4.2 Schematic potential distribution in unpolarized IDEAL cell (a) and polarized IDEAL cell (b), Figures after C.Nicolella [1]

As the IDEAL cell is loaded with current (i.e. polarized), all three potential ladders become reduced (see Figure 4.2b) attributed to activation polarization and ohmic polarization aroused by reaction and ionic transport respectively:

$$\eta_{A+C} = \Delta\phi_A^0 - \Delta\phi_A + \Delta\phi_C^0 - \Delta\phi_C \tag{4.5}$$

$$\eta_{AE+CE} = (\phi_{\mathrm{PCP}}\big|_{x=\delta_1} - \phi_{\mathrm{PCP}}\big|_{x=\delta_2}) + (\phi_{\mathrm{ACP}}\big|_{x=\delta_3} - \phi_{\mathrm{ACP}}\big|_{x=\delta_4}) \tag{4.6}$$

$$\eta_{\mathrm{CM}} = \Delta\phi_{\mathrm{CM}}^0 - (\phi_{\mathrm{ACP}}\big|_{x=\delta_2} - \phi_{PCP}\big|_{x=\delta_3}) \tag{4.7}$$

Where superscript 0 means the potential at unpolarized condition, $\Delta\phi_{\mathrm{CM}}{}^0$ is described for the potential difference through CM at unpolarized condition, which can be given by Nernst Equation as:

$$\Delta\phi_M^0 = -\frac{\Delta G^0}{2F} - \frac{RT}{2F}\ln\left(\frac{a(\mathrm{H_2O})}{a^2(\mathrm{H^+_{PCP}})a(\mathrm{O^{2-}_{ACP}})}\right) \tag{4.8}$$

Where ΔG^0 is the Gibbs free energy of reaction and *a* represents the chemical activity of species involved in reaction, the polarizations (equation 4.5-4.7) can be interpreted as driving force consumed during processes. Ultimately, this consumption is embodied as the reduction of output cell voltage:

$$\begin{aligned} E_{cell} &= \phi_C - \phi_A \\ &= \Delta\phi_C - IR_{CE} + (\phi_{ACP}\big|_{x=\delta_2} - \phi_{PCP}\big|_{x=\delta_3}) - IR_{AE} + \Delta\phi_A \\ &= (\Delta\phi_C^0 - \eta_C) - \eta_{CE} + (\Delta\phi_{CM}^0 - \eta_{CM}) - \eta_{AE} + (\Delta\phi_A^0 - \eta_A) \\ &= (\Delta\phi_C^0 + \Delta\phi_{CM}^0 + \Delta\phi_A^0) - (\eta_C + \eta_{CE} + \eta_{CM} + \eta_{AE} + \eta_A) \\ &= E_{cell}^0 - \eta_C - \eta_{CE} - \eta_{CM} - \eta_{AE} - \eta_A \end{aligned} \tag{4.9}$$

When the complete IDEAL-Cell is modelled, it is important to use consistent thermodynamic data for calculating ΔG^0 in the Nernst equation 4.8. As combined with two half-cell reactions, the model is thermodynamically consistent and yields the open-circuit cell voltage[2].

4.2 Steady state model in CM

To successfully model and predict IDEAL cell performances, numeric relations of each polarizations (4.5-4.7) as a function of operating conditions (i.e. temperatures and current densities) are prerequisites. As mentioned above, CM is frontier system that has never been studied. Main work of this chapter is concentrated on mathematical modelling built in CM and kinetic phenomenon comprehension based on the model. For the first period development of IDEAL cell, it is designed as cylindrical and homocentric five layers. For the sake of simplicity, it is sufficient to build a two dimensional model under cylindrical coordination in following Figure 4.3:

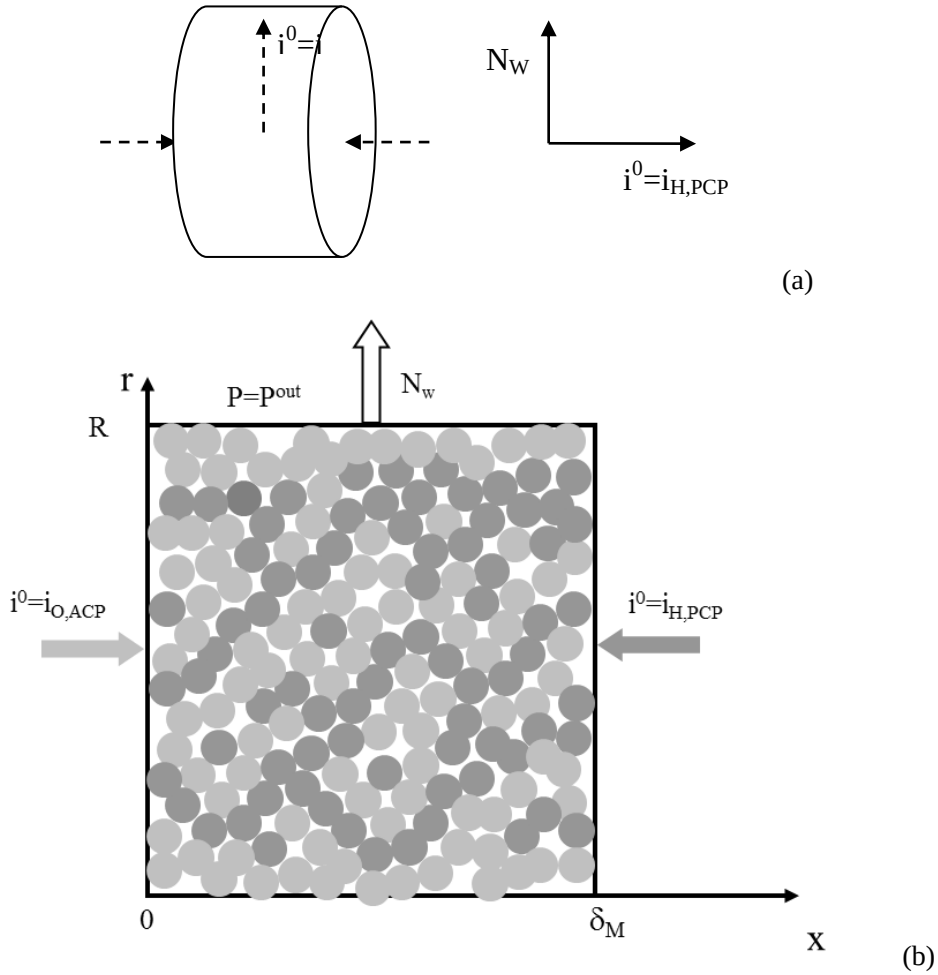

Fig. 4.3 a) Cylindrical geometry of CM with mass transfer inside, b) 2 D cylindrical coordination built on a slice of CM

From a macroscopic view of CM by Figure 4.3a, ionic transport (including proton and oxygen ion) only considered in x coordination is perpendicular to water transport which is only considered in r coordination as well. However, in a microscopic view (Figure 4.3b), ionic conducting paths are twisted and partially continuous. Even water evacuation routes are impossible to function as straight channel. Under these realizations, some basic assumptions are made before entering into model derivations:

- Steady-state conditions;
- Uniform temperature distribution throughout CM;
- Mono-size spherical particles and randomly packed composite CM;
- Continuum conducting phases and evacuation channels by applying effective transport coefficients;

- Oxygen ion conductivity of BCY in composite CM is not taken into account;

To estimate the polarization resistance, the potential distribution in the CM is related to the flux of protons and oxygen ions in the conducting phases by including kinetic and transport equations into charge balances. Since water pressure may affect the overall rate of water formation in the CM, water mass balances across the CM and transport equations are also considered. For stationary conditions, the continuity equations for the ionic species in the central membrane follow as:

$$\nabla \cdot N_{H,PCP} = -2 i_M^V / F \tag{4.10}$$

$$\nabla \cdot N_{O,ACP} = -i_M^V / F \tag{4.11}$$

Where N denotes flux rate with unit of mol/(cm^2 s), $i_M{}^V$ (follow the name of parameter investigated in electrodes) is apparent current volumetric density with unit of A/cm^3 corresponding to the volumetric reaction rate of water formation, F is faraday constant. The negative signs on right side of equation 4.10 and 11 (source terms) represent that ionic species are consumed during reaction, in which water is produced and subsequently have positive sign on source term. The pressure of water in the membrane pores is calculated through a mass balance in the gas phase. This gradient can be readily characterised through differential mass balances on infinitesimal volumes:

$$\nabla \cdot N_w = i_M^V / F \tag{4.12}$$

This current volumetric density $i_M{}^V$ is local variable depending concentrations and voltage difference (driving force) which is assumed to have a classic Butler-Volmer expression[3] as follows:

$$i_M^V = i_0^V \left[\exp\left(\alpha_M \frac{F}{R_g T} \eta_M \right) - \exp\left(-(1-\alpha_M) \frac{F}{R_g T} \eta_M \right) \right] \tag{4.13}$$

Where α_M is transfer coefficient factor with typical value of 0.5, η_M is the activation polarization which can be expressed as $\Delta\phi_{CM}{}^0$-$\Delta\phi_{CM}$, $i_o{}^V$ is specific current volumetric density with same unit with $i_M{}^V$ and it is considered to be linked with two aspects: i)

reaction area: three phase boundary length, L_{TPB} (introduced in chapter 3) and ii) intrinsic reaction rate i_0^{L}. The relationship is written as follows:

$$i_0^V[\frac{\mathrm{A}}{\mathrm{cm}^3} \text{ or } \frac{\mathrm{mA}}{\mathrm{cm}^3}] = L_{\mathrm{TPB}}^{\mathrm{eff}}[\frac{\mathrm{cm}}{\mathrm{cm}^3}] \times i_0^L[\frac{\mathrm{A}}{\mathrm{cm}} \text{ or } \frac{\mathrm{mA}}{\mathrm{cm}^3}] \tag{4.14}$$

Where intrinsic reaction rate i_0^{L} is considered as (except materials) only temperature dependent parameter for ionic recombination in CM, in other words, this parameter remains the same no matter what morphology possessed by CM. The three phase boundary length L_{TPB} is geometric parameter which is dealt with its morphology. Based on these definitions, the specific volumetric current density $i_{\mathrm{M}}^{\mathrm{V}}$ has already included the effect from morphology L_{TPB} which is dependent on sample (e.g. volume fraction, grain size, contact angle), driving force $\Delta\phi_{\mathrm{M}}$ which is function of mass transfer (effective conductivity, thickness of CM), and intrinsic reaction rate i_0^{L} which is decided by temperatures. Equation 4.13 and 4.14 helps us to understand the expression of source term (right part) in equation 4.10-12. The definition of ionic and water flux terms (left part) can be associated to current densities in conducting phases, which are related to potentials through the Ohm law at steady state:

$$N_{H,PCP} = \frac{i_{H,PCP}}{F} = -\frac{\sigma_{PCP}^{eff}}{F}\nabla\phi_{PCP} \tag{4.15}$$

$$N_{O,PCP} = \frac{i_{O,ACP}}{2F} = \frac{\sigma_{ACP}^{eff}}{2F}\nabla\phi_{ACP} \tag{4.16}$$

Where $i_{\mathrm{H,PCP}}$ and $i_{\mathrm{O,ACP}}$ refer to ionic current density in its conducting phase, σ^{eff} denotes effective conductivity of charged species which has already included all factors (e.g. tortuosity in binary composite, grain boundary effect if there is). A gradient of partial pressure of water vapor is expected because of the resistance to flow in the membrane pores. The water flux can be calculated by following equation:

$$N_w = -\frac{P_w}{R_g T}\frac{B}{\mu}\nabla P_w \tag{4.17}$$

Where μ is the vapour viscosity in porous channel, permeability B can be calculated as a function of the morphological properties of CM by using empirical expressions given by Blake-Kozeny[4]:

$$B = \frac{d_p^2}{72\tau}\frac{\varepsilon^3}{\left(1-\varepsilon\right)^2} \tag{4.18}$$

Where d_p is the mean particle size, ε is CM porosity, τ is the tortuosity of composite material. With reference to the integration domain represented in Figure 3b, let the interface between the protonic electrolyte and the CM be at x =0, and the interface between the CM and the anionic electrolyte be at x =δ_M. Boundary conditions upon above equations are listed as follows:

x=0: $\phi_{ACP} = 0$ (potential reference)

$$i_{O,ACP} = 0, i_{H,PCP} = i_{tot}$$

x=δ_M: $$i_{H,PCP} = 0, i_{O,ACP} = -i_{tot}$$

r=0: $$\frac{\partial P}{\partial r} = 0; \frac{\partial \phi_{PCP}}{\partial r} = 0; \frac{\partial \phi_{ACP}}{\partial r} = 0$$

r=R: $$P_w = P^{out}; \frac{\partial \phi_{PCP}}{\partial r} = 0; \frac{\partial \phi_{ACP}}{\partial r} = 0$$

Where i_{tot} refers to total current density which can be obtained from measurement, P^{out} refers to pressure outside IDEAL cell. Normally, we appoint this pressure as 1 atm.

4.3 Numeric Simulation

Mathematic model is computed by CMSOL Multiphysics software with suitable geometric, morphological and kinetic parameters which have been summarized in table 4.1. We consider scale of some parameters (e.g. porosity, CM thickness) to check their sensitivities on total polarizations attributed from CM. Last of all, since we have no idea about the ionic recombination rate, kinetic parameter: specific current volumetric density i_v^0 is also calculated with estimated ranges from 10^{10} -10^{13} A/cm^3.

Table 4.1 Parameters used in simulations

	Value	Units
Operating conditions		
Temperature, T [a]	600	℃
Outside pressure, P_{out} [a]	1	atm
CM design parameters		
Thickness of CM [b]	10-1000	μm
Diameter of CM [a]	10	mm
Volume ratio of PCP/ACP [a]	1	
PCP and ACP grain size [b]	1	μm
Porosity, ε [b]	0.3	
Tortuosity, τ [b]	2-4	
Material properties		
σ_{PCP} (dense, BCY15) [c]	0.017	S/cm
σ_{ACP} (dense, YDC15) [c]	0.018	S/cm
σ_{PCP}^{eff} (CM, BCY15) [c]	0.002-0.0034	S/cm
σ_{ACP}^{eff} (CM, YDC15) [c]	0.002-0.0034	S/cm
Kinetic parameters		
i_v^0 [b]	10^{10} -10^{13}	A/cm^3
Variable		
i_{tot}		A/cm^2

[a] Objectives

[b] Estimations

[c] Calculation from chapter 2 and 3 (grain boundary effect excluded)

In reality, effective conductivities of PCP and ACP are interdependent on morphology properties such as grain size, volume fraction, porosity and tortuosity which especially tortuosity are interdependent on other three parameters. In this chapter, effective conductivities are estimated from percolation theory which is not necessary to consider tortuosity. The suggested ranges of tortuosity (more precise to say pore channel tortuosity) here has influence on water pressure corresponding to concentration polarizations. One independent variable in numeric simulations is total current density which has been introduced in boundary conditions. All of our interests on dependent variables (e.g. local activation polarization, total polarization from CM, etc.) are presented as a function of total current densities. Figure 4.4 shows activation polarization distribution through CM. x coordinate denotes dimensionless thickness of CM, in which way activation polarization distribution in CMs with different thicknesses can be compared in one Figure. Under same morphology and given total current density, every reactive site in thinner CM is responsible for more products. Correspondingly it needs larger driving force to accomplish this requirement. From this point of view, local activation polarization in thinner CM is comparative higher. Another characteristic aspect can be noticed is that in the middle of CM, driving force is less than ones at two extremes of CM due to more reactants are expected to accumulate there. The thicker CM applied, more chances for ionic recombination could happen in the middle.

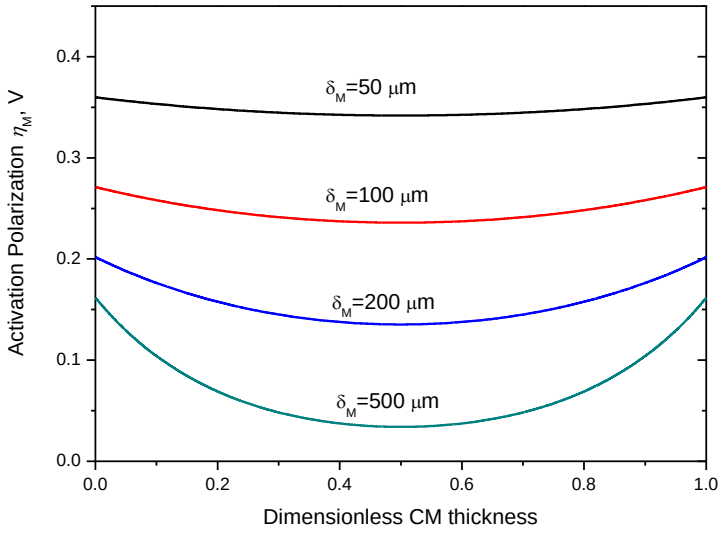

Fig. 4.4 Local activation polarization distribution through CM with different thicknesses, parameters used in calculation are: ε=0.3, i_V^0=10^{12} A/cm^3, i_{tot}=0.05 A/cm^2

Figure 4.4 shows as well that activation polarization η_M is local variable (here we only consider one dimensional variable. In cross-sectional area of CM η_M may actually also changes with positions). Overall polarizations as integration of ohmic polarization and activation polarization is depending on reaction rate and current density loaded, the relations of which are plotted in Figure 4.5 under consideration of 30% porosity and 100 μm thick CM. Upper limit of overall polarization is 1 V. Possible reaction rate i_V^0 varies from 10^{10}-10^{13} A/cm^3 resulting that different maximum current density reaches at same upper limit.

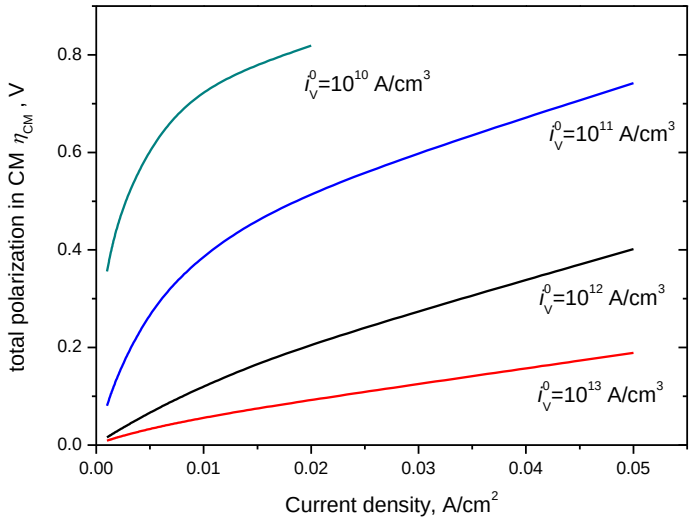

Fig. 4.5 Overall polarizations in CM as a function of current densities, parameters used in calculation are: ε=0.3, δ_M=100 μm

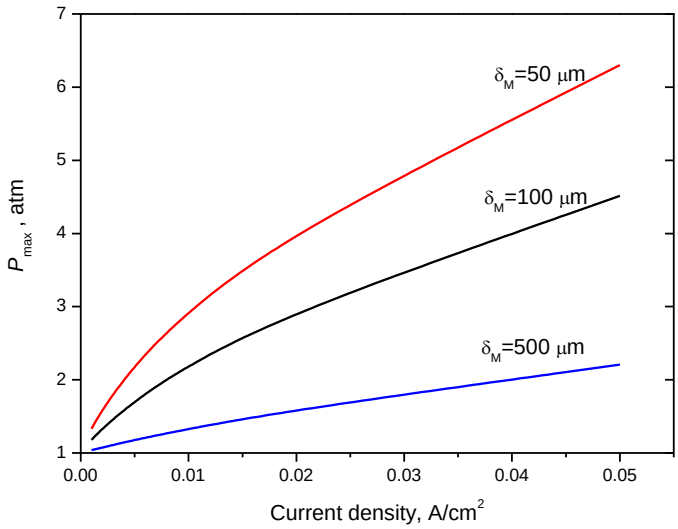

Fig. 4.6 Maximum water pressure accumulated in CM, parameters used are: ε=0.3, i_V^0=10^{12} A/cm^3

Under a steady state, water evacuation is expected to be driven by pressure gradient accumulated in CM. High kinetic rate/water diffusivity leads to high pressure gradient. The disadvantages of this accumulation may be attributed to reverse effect on ionic recombination and concentration polarizations. Hence, the scale of pressure formed and maximum concentration polarization which is expressed as follows are also our concerns:

$$\eta_{conc} = \frac{R_g T}{2F} \log(\frac{P}{P^{out}}) \tag{4.19}$$

Figure 4.6 presents numeric calculation of maximum pressure as a function of current density. Since in calculation reaction rate considered is relative faster than evacuation, in case of thin CM (50μm), expected pressure is as high as 6 atm under 0.05 A/cm^2. In a real working CM, it is not preferable to reach such a high pressure level due to strong reverse effect on ionic recombination. However, this situation with fixed reaction rate under consideration is more ideal. Based on the calculated pressures in Figure 4.6, we also can develop concentration polarization as a function of current density in Figure 4.7. Although overall concentration polarization increases with current density, its fraction to total polarization in CM drops under same conditions.

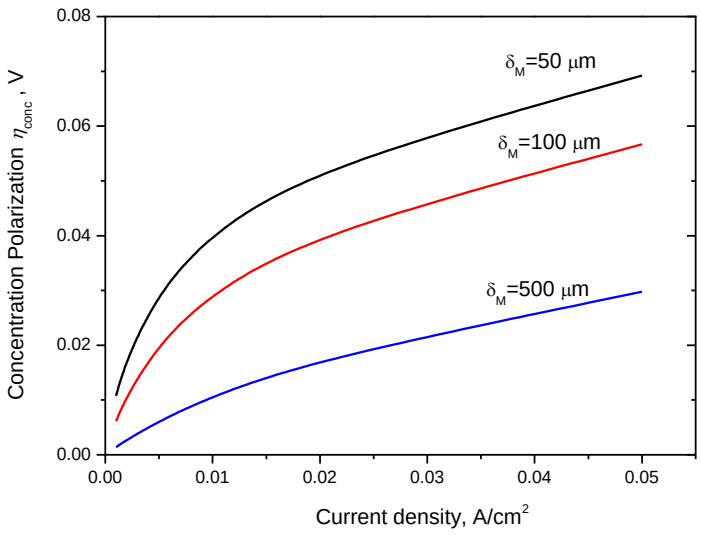

Fig. 4.7 Concentration polarizations in CM with different thicknesses, parameters used are: ε=0.3, i_V^0=10^{12} A/cm^3

The numeric simulation on basis of model presented in this paragraph is to show general relations between polarization losses in CM and its geometric and morphological properties, and above all estimated ionic recombination rate. By applying these numeric relations to fit available experimental data, we can finally obtain intrinsic kinetic parameter which we believe it is mechanism of reaction and only temperature dependent. To this end, developed

model with determined parameters enables us to explain and predict CM performances and also helps to optimize and design IDEAL cell.

4.4 Validations and Discussions

In validation sections, a series of Proof of Concept (PoC) cells were fabricated within this project by collaborators. For the sake of emphasizing CM performances, all PoC samples were made with simplified electrodes which were brushed with platinum ink (in some samples Ag was also tried) on both sides of dual membrane (two electrolytes plus central membrane, see Figure 8a). Materials for electrolytes were always BCY15 for protonic conducting electrolyte and YDC15 for anionic conducting electrolyte. In this design, polarization losses from electrodes and electrolytes are easy to characterize which are proportional to total current densities.

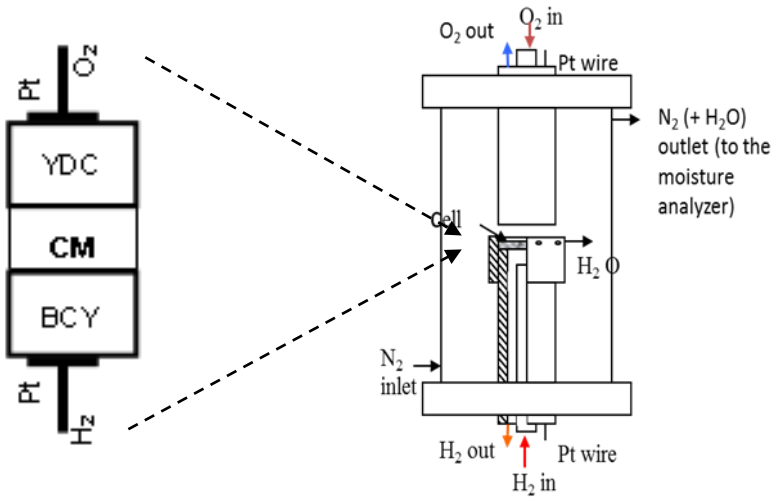

Fig. 4.8 Schematic Figure of PoC sample (left) and experiment set ups (right)

PoC sample is placed in the middle of furnace along with hydrogen fed upwards and oxygen fed downwards which is drawn on the right part of Figure 4.8. The water produced in the middle compartment of cell is evacuated perpendicularly to the flow of fuels by flowing nitrogen gas to the moisture analyser. The required temperature is provided by the furnace and preserved by third chamber made of quartz. The measurement is electrochemical impedance spectra. Three PoC samples with sufficient geometrical and morphological data (see Figure 9) which were processed by method of cold pressing, spark plasma sintering and tape casting respectively were taken into account. Cold pressing is

common method to possess multilayers with different thicknesses. However, it is not convenient to control grain sizes distribution in CM. As observed from SEM image of CM, agglomerates of particles are severe with scale of sizes from 30 to 90 μm. Although agglomerates don't influence conductivities of PCP or ACP, its presence indeed reduces effective TPB lengths which as mentioned are disadvantageous of minimization of polarization losses.

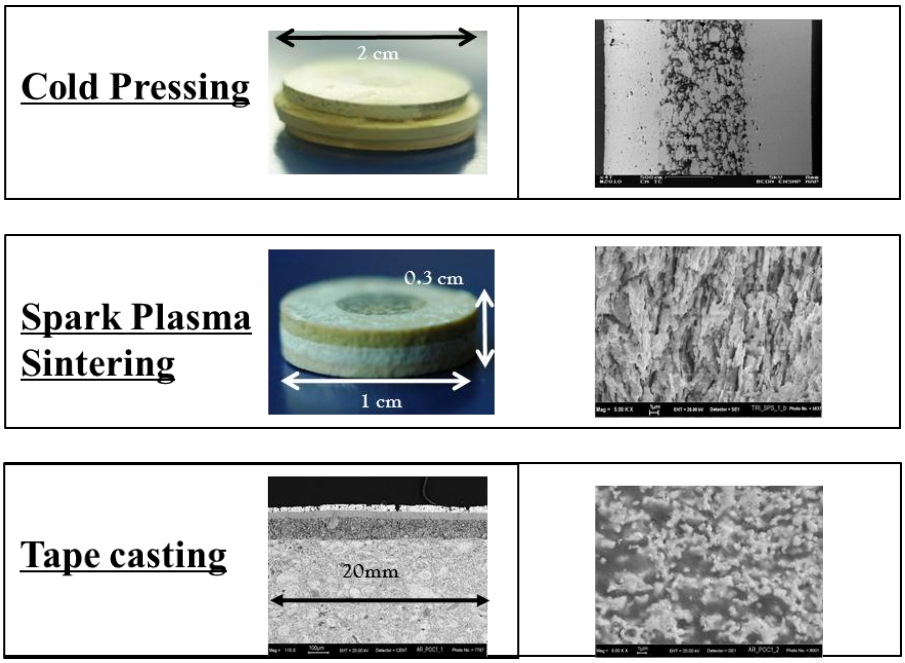

Fig. 4.9 SEM images of Proof of Concept samples fabricated by different techniques, left Figures are geometric dimension of PoC cells, right Figures are amplifications of CM

SPS is powerful for controlling morphology of CM. By this technique, the pores possess the elongated shape given by the graphite with major axis oriented transversally to the pressure direction. This can be expected to be a favorable condition for water vapor elimination from the central membrane; this is also highly favorable from the morphology viewpoint since the percolation perpendicular to the membrane axis will be attained then much more easily. Although grain size is quite smaller than CP sample but with a distribution from 2-20 μm are taken into account in simulation due to the grain shapes. Tape casting is benefit for fabricating thin CM (with 50 μm) with narrow grain size distribution from 0.5-1 μm. This scale of grain size and distribution could be expected more active TPB lengths inside. More detailed data about these PoC samples are presented in table 4.2.

Table 4.2 Collection of PoC samples

		CP sample	SPS sample	TC sample
Geometry	Radius	10 mm	4 mm	10 mm
	AE thickness	600 μm	930 μm	600 μm
	CM thickness	700 μm	750 μm	50 μm
	CE thickness	600 μm	610 μm	31 μm
CM Morphology	Grain size	30-90 μm	2-20 μm	0.5-1 μm
	Volume fraction	0.25:0.25	0.25:0.25	0.35:0.35
	Porosity	0.5	0.5	0.3
Effective conductivity, σ^{eff}	PCP	0.002 S/cm	0.002 S/cm	0.0034 S/cm
	ACP	0.002 S/cm	0.002 S/cm	0.0034 S/cm
Electrode resistance, R_p	Anode/Electrolyte		3.9 $\Omega \cdot cm^2$	
	Cathode/Electrolyte		3.4 $\Omega \cdot cm^2$	

The measured I-V and P-V characteristic plots are summarized in Figure 4.10a, from which poor performances of PoC cells have been observed. Among three samples, relative higher cell performance was contributed by TC sample, which has been mentioned to have thin CM compartment and smaller grain size and its distribution than other two samples. Maximum power density of TC sample was only 4.7 mW /cm^2, which is rather smaller than 200-900 mW /cm^2 of conventional SOFCs. From characteristic I-V curves of all samples (quite straight), it is presumably due to high ohm loss dominating total polarization loss.

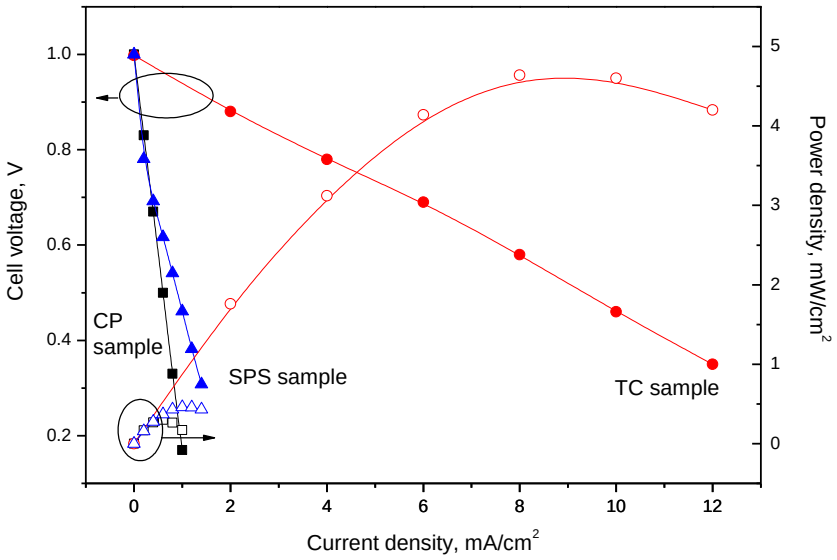
Cell voltage, V
Power density, mW/cm^2
Current density, mA/cm^2
CP sample
SPS sample
TC sample

(a)

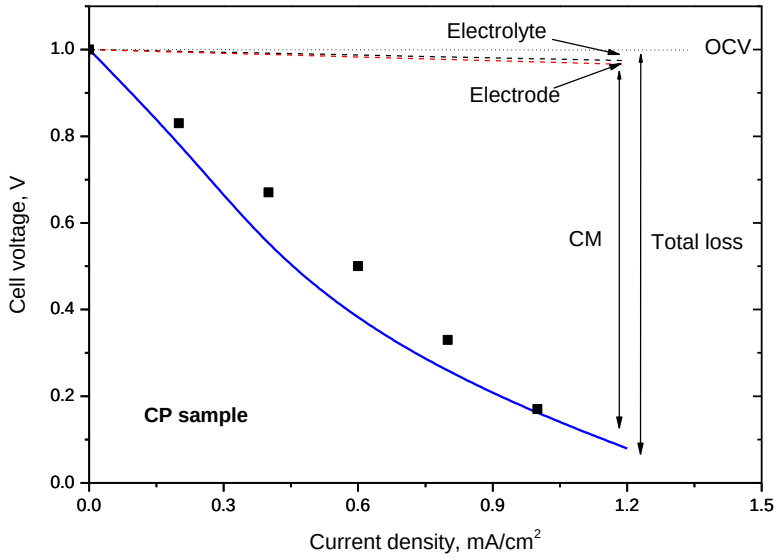
Electrolyte
OCV
Electrode
CM
Total loss
CP sample
Cell voltage, V
Current density, mA/cm^2

(b)

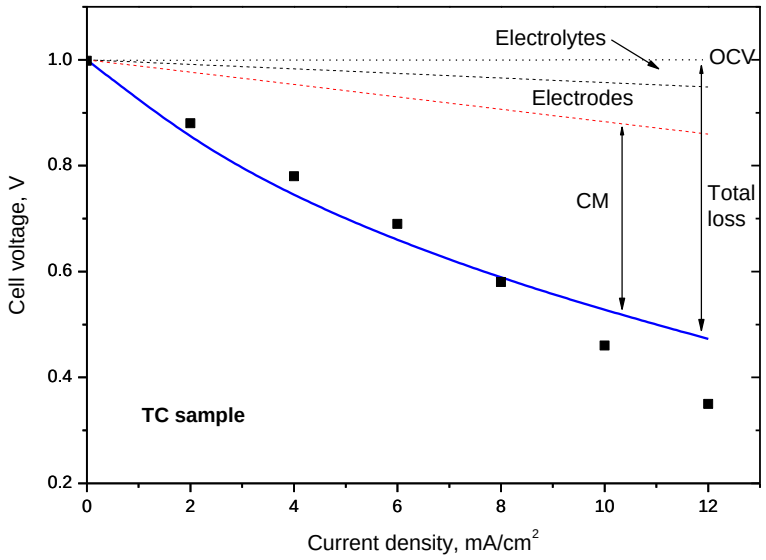

(c)

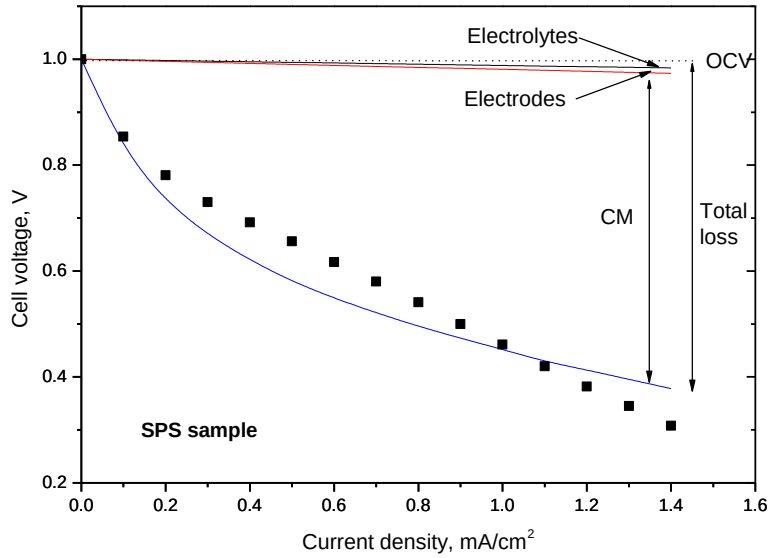

(d)

Fig. 4.10 a) Experimental data on IV curves of 3 PoC samples, validations of model on (b) CP sample, (c) TC sample and (d) SPS sample

In process of validation, unknown parameter i_0^V varies to fit simulation results with experimental data under current densities. Polarization losses from other compartments such as electrodes and electrolytes as mentioned are linear with current densities. By deducting polarization losses from these compartments, the rest one is considered to be contributed from CM. To admit, no extra effects from attachment of layers or gas leak have been taken

into account. Nevertheless, validation results of three PoC samples in Figure 4.10b-4.10d demonstrate anticipated results that total polarizations losses are dominated by CM. In CP and SPS samples with thick CMs, the fractions of CM contribution exceed 90% which results extreme low performances. Although the suitable in TC sample is better, it still accounts for 80% of total polarization losses. By least square minimization between simulation results and experimental results, determined i_0^V from validations are 0.17, 100 and 0.5 mA /cm^3 belonging to CP, TC and SPS samples separately. Grain size distributions are estimated from SEM images, which (especially CP and SPS samples) are quite irregular than normal distribution. With this point of view, we apply equation 4.20 [5] to calculate effective (or active) TPB length in all ranges of possible grain size distribution, results of which are presented in Figure 4.11:

$$L_{\mathrm{TPB}}^{\mathrm{eff}} = [\frac{3}{2}\frac{\min(r_i, r_j)}{r_i^3}(1-\varepsilon)\sin\theta]\psi_i Z_{ii} p_i p_j \tag{4.20}$$

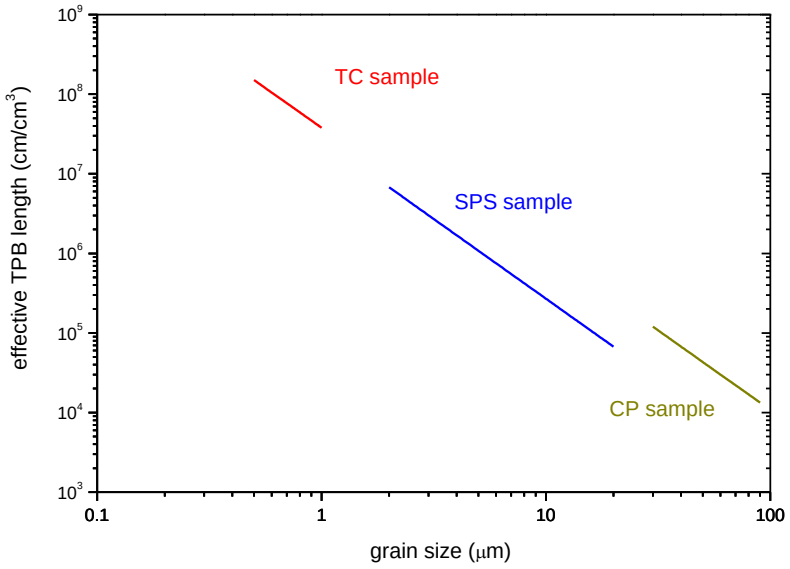

Fig. 4.11 Effective TPB lengths under possible grain size distribution of three PoC samples

Results from Figure 4.11 clearly illustrate that large grain size sample is extremely unfavorably to active reaction sites-TPB lengths. For instance, TC sample with 0.5-1 μm grain size is expected to have 3-4 orders of magnitude higher TPB lengths than CP sample. However, as concluded in Chapter 3, grain size of ionic conductor is better to maintain at 1

μm level so as to obtain ignorable grain boundary effect on ionic conductions. These contradicting statements could be balanced (as suggested) at around 1 μm grain size which on one hand could minimize grain boundary effect, on the other hand guarantee active TPB lengths within one order less than the one with nanometer grain sizes. As demonstrated in equation 4.14, intrinsic kinetic parameter i_0^{L} can be estimated from ratio of i_0^{V}/L_{TPB}^{eff}. Since several orders differences of TPB length and i_0^{V}, we need to rearrange equation 4.14 by taking logarithm on both sides to yield:

$$\log i_0^V = \log L_{\mathrm{TPB}}^{\mathrm{eff}} + \log i_0^L \tag{4.21}$$

In this way, log i_0^{V} is proportional to log L_{TPB}^{eff} with unit slope. As log L_{TPB}^{eff} equals to zero, the interception of relation 4.21 on the vertical coordinate is equal to desired parameters. Following this way, parameters of log i_0^{V} and logL_{TPB}^{eff} are plotted in Figure 4.12, in which we schematically add two dashed lines with unit slop to cover all possible TPB length ranges of samples as symbolized with colorful dots. In other words, if there is any other samples made by same materials and operated at same temperature, the ratio of log i_0^{V} / logL_{TPB}^{eff} should also locate somewhere in the area between two dashed lines. To the end, the intercepted values as marked by double arrow are between -5 and -7 corresponding to 10^{-7} – 10^{-5} mA/cm values of i_0^{L}.

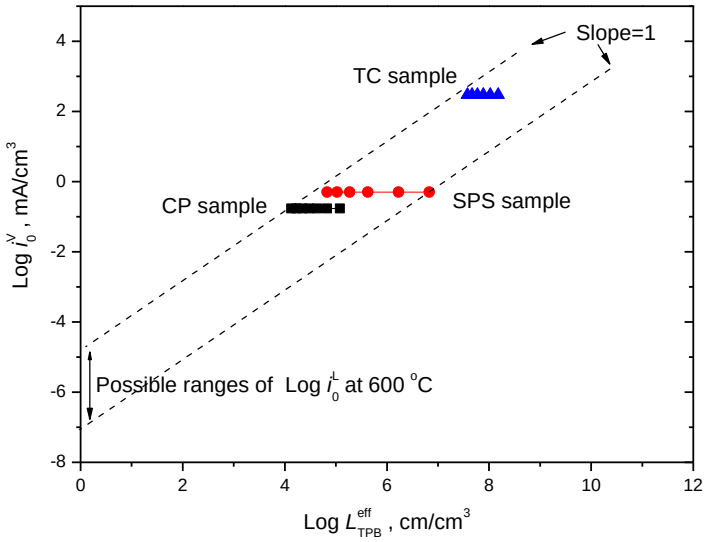

Fig. 4.12 Possible ranges of kinetic parameter i_0^{L} determined from three PoC samples

In order to understand scale of this kinetic parameter for ionic recombination, we collect some available kinetic data of anodic reaction and cathodic reaction in Figure 4.13 and table 4.3.

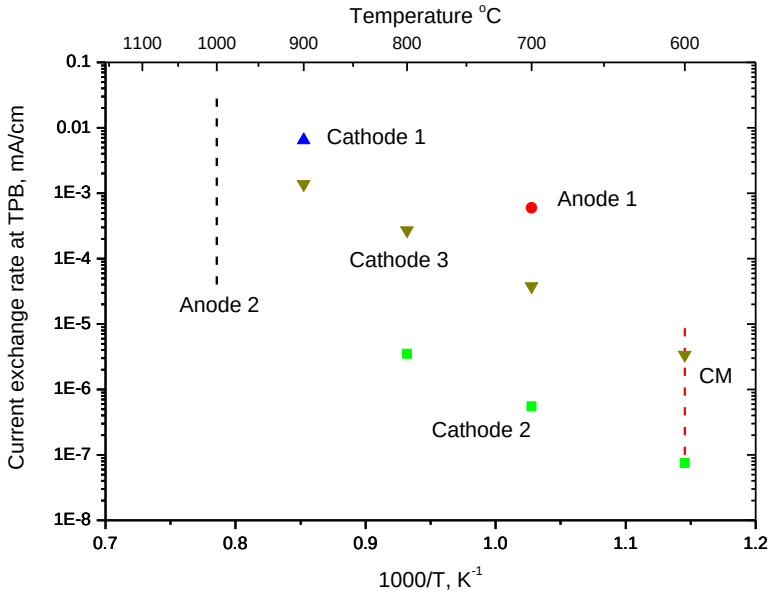

Fig. 4.13 Comparison of intrinsic kinetic parameters of anodic and cathodic reactions with ionic recombination in CM, dashed lines represent possible ranges of parameters

Table 3 more detailed information of reaction systems

Reactions	materials	Temperature	Uniformed i_0^L mA/cm	Ref
$H_2 + O^{2-} \Leftrightarrow H_2O$	Ni/YSZ	700℃	6×10^{-4}	[6]
	Ni/YSZ	1000℃	10^{-5}–10^{-2}	[7]
$\frac{1}{2}O_2 + 2e^- \Leftrightarrow O^{2-}$	LSM/YSZ	600℃	7.5×10^{-8}	[8]
		700℃	5.5×10^{-7}	
		800℃	3.5×10^{-6}	

	Pt/EDB	900℃	6.5×10^{-3}	[9]
	LSM/YSZ	600℃	3.4×10^{-6}	[10]
		700℃	3.8×10^{-5}	
		800℃	2.7×10^{-4}	
		900℃	1.4×10^{-3}	
$2H^{+}+O^{2-}\Leftrightarrow H_2O$	BCY/YDC	600℃	10^{-7}–10^{-5}	This study

Some values were estimated by author (displayed by dashed line) while some values provided by authors with other format of units have been rearranged to the one with uniformed unit mA/cm. Observed from Figure 4.13, kinetic rate of ionic recombination is comparable with cathodic reaction at same temperature. However, anodic reaction rate is quite a complex process which has been studied to split overall reaction into several elementary reaction steps [11-15]. Plus anode supported SOFCs have been widely applied, diffusion effect is suggested to taken into account together with reaction under different anode designs. Generally speaking, current exchange rate at TPB i_0^{L} in anodic reaction is larger than cathodic reaction (e.g. one order higher at 500 and 600℃ in anode supported SOFC[16]) at intermediate temperature ranges, which is the reason that anode supported SOFC is preferable in SOFC developments at intermediate temperature ranges. In short, the sequence of current exchange rate at TPB is as i_0^{L} (anodic reaction) > i_0^{L} (cathodic reaction) ≈ i_0^{L} (ionic recombination). Under this realization, the first idea about IDEAL cell design also follow as anode supported IDEAL cell.

4.5 Conclusions

In this chapter, a two dimensional steady state model has been built to characterize mass transfer and reaction phenomenon inside CM. The objectives of this modeling work are to numerically link polarization losses with CM properties such as effective conductivities of

ionic conductors, geometrical dimensions and morphologies. In addition to that, mathematic model also enable us to distinguish partial polarizations relating with above aspects.

Three PoC samples with simplified electrodes have been made on one side to measure produced water from CM, on the other side to provide V-I plots for validation. Performances of PoC samples have been found to be poor due to high limited TPB lengths formed during processes. Probable reason for high limited TPB lengths formed in CM is attributed to agglomerates formed which is demonstrated to have no influence on conductivity but have strong effect on TPB length (no pores existing in agglomerates). This leads to major polarization loss of PoC samples are attributed from CM.

In addition, effective ranges of intrinsic reaction rate i_0^{L} have been determined through three PoC samples which are considered to maintain in same order with oxygen reduction rate in cathode. This found leaves a preliminary concept that complete IDEAL cell should be anode supported type due to anodic reaction rate is highest.

Appendix

Derivation of Nernst Equation for CM reaction

The CM reaction is given by:

[A-1] $$2H^{+}_{PCP} + O^{2-}_{ACP} \leftrightarrow H_2O$$

In electrochemical equilibrium, the electrochemical potentials of the participating species must sum up to zero:

[A-2] $$\tilde{\mu}(H_2O) - 2\tilde{\mu}(H^{+}_{PCP}) - \tilde{\mu}(O^{2-}_{ACP}) = 0$$

The concentration and potential dependence of the electrochemical potential is given by:

[A-3] $$\tilde{\mu}_i = \mu_i^0 + RT \ln a_i + zF\phi_i$$

Where μ^0 is the chemical potential at an activity of unity, by inserting Eq. A-3 into Eq. A-2 yields:

$$\mu^0_{H2O} + RT \ln a_{H2O} - 2\mu^0_{H^{+}_{PCP}} - 2RT \ln a_{H^{+}_{PCP}} - 2 \cdot 1 \cdot F\phi_{PCP} - \mu^0_{O^{2-}_{ACP}} - RT \ln a_{O^{2-}_{ACP}} - 1 \cdot (-2) \cdot F\phi_{ACP} = 0$$

$$\mu^0_{H2O} - 2\mu^0_{H^{+}_{PCP}} - \mu^0_{O^{2-}_{ACP}} + RT \ln a_{H2O} - 2RT \ln a_{H^{+}_{PCP}} - RT \ln a_{O^{2-}_{ACP}} = 2F\phi_{PCP} - 2F\phi_{ACP}$$

$$\mu^0_{H2O} - 2\mu^0_{H^{+}_{PCP}} - \mu^0_{O^{2-}_{ACP}} + RT \ln \frac{a_{H2O}}{a^2_{H^{+}_{PCP}} a_{O^{2-}_{ACP}}} = 2F(\phi_{PCP} - \phi_{ACP})$$

$$\frac{\Delta G}{2F} + \frac{RT}{2F} \ln \frac{a_{H2O}}{a^2_{H^{+}_{PCP}} a_{O^{2-}_{ACP}}} = \phi_{PCP} - \phi_{ACP}$$

[A-4] $$\Delta\phi_{CM,\,equil} = \phi_{ACP} - \phi_{PCP} = -\frac{\Delta G}{2F} - \frac{RT}{2F} \ln\left(\frac{a(H_2O)}{a^2(H^{+}_{PCP}) a(O^{2-}_{ACP})}\right)$$

Finally, with the definition of potential difference given in Eq. A-4., we arrive at the Nernst equation 5:

[A-5] $$\Delta\phi_{CM,\,equil} = \phi_{ACP} - \phi_{PCP} = -\frac{\Delta G}{2F} - \frac{RT}{2F} \ln\left(\frac{a(H_2O)}{a^2(H^{+}_{PCP}) a(O^{2-}_{ACP})}\right)$$

Reference

1. Cristiano Nicolella, N.V., Wolfgang G. Bessler, *A mathematical model of mass and charge transport and reaction in the central membrane of the IDEAL-Cell*. 2009, Pisa University: Pisa.

2. Bessler, W.G. and S. Gewies, *Gas concentration impedance of solid oxide fuel cell anodes*. Journal of The Electrochemical Society, 2007. **154**(6): p. B548-B559.

3. Allen J.Bard, L.R.F., ed. *Electrochemical Methods: fundamentals and applications*. 2nd ed. 2000, Wiley: New York. 856.

4. Bird R.B., S.W.E., Lightfoot E.N., ed. *Transport Phenomena*. 1960, Wiley: New York.

5. Chen, D., et al., *Percolation theory to predict effective properties of solid oxide fuel-cell composite electrodes*. Journal of Power Sources, 2009. **191**(2): p. 240-252.

6. David G. Goodwin, H.Z., Andrew M. Colclasure, Robert J. Kee, *Modeling Electrochemical Oxidation of Hydrogen on Ni–YSZ Pattern Anodes*. Journal of The Electrochemical Society, 2009. **156**(9): p. B1004.

7. S.Sunde, *Simulations of Composite Electrodes in Fuel Cells*. Journal of Electroceramics, 2000. **5**(2).

8. Nicolella, C., et al., *Morphology and electrochemical activity of SOFC composite cathodes: II. Mathematical modelling*. Journal of Applied Electrochemistry, 2009. **39**(4): p. 503-511.

9. P.Costamagna, P.C., V.Antonucci, *Micro-modelling of solid oxide fuel cell electrodes*. Electrochimica Acta, 1998. **43**(3-4): p. 375.

10. X.J.Chen, S.H.C., K.A.Khor, *Simulation of a composite cathode in solid oxide fuel cells*. Electrochimica Acta, 2004. **49**.

11. A.Bieberle, L.J.G., *State space modeling of the anodic SOFC system Ni, H_2-H_2O/YSZ*. Solid State Ionics, 2002. **146**.

12. H.Y.Zhu, R.J.K., V.M.Janardhanan,O.Deutschmann,D.G.Goodwin, *Modeling Elementary Hetergeneous Chemistry and Electrochemistry in Solid Oxide Fuel Cells*. Journal of The Electrochemical Society, 2005. **152**(12).

13. D.G.Goodwin, H.Y.Z., A.M.Colclasure, R.J.Kee, *Modeling Electrochemical Oxidation of Hydrogen on Ni-YSZ Pattern Anodes*. Journal of The Electrochemical Society, 2009. **156**(9).

14. M.Vogler, A.B.H., L.Gauckler, J.Warnatz, W.G.Bessler, *Modeling Study of Surface Reactions, Diffusion, and Spillover at a Ni/YSZ Patterned Anode*. Journal of The Electrochemical Society, 2009. **156**(5).

15. A.Bieberle, L.J.G., *Reaction mechanism of Ni pattern anodes for solid oxide fuel cells*. Solid State Ionics, 2000. **135**.

16. D.Cui, Q.L., F.Chen, *Modeling of anode supported SOFCs with samaria doped-ceria electrolytes operating at 500-600 ^{o}C*. Journal of Power Sources, 2010. **195**.

Chapter 5 General Conclusions

5.1. Conclusions on Modeling Simulation Results

This thesis mainly concerns about mathematic modeling and simulation on complex mass transfer phenomenon and ionic recombination in central membrane. In detail, content of modeling works include following aspects:

1) Theory support of efficiency improvements in case of removing water from electrodes in conventional SOFCs by thermodynamic analysis (Chapter 1). It is indicated from calculation that IDEAL-Cell can potentially provide 15% higher Nernst potential than PCFC and 30% higher Nernst potential than ACFC at intermediate temperature ranges and high fuel utilizations.

2) Calculation of mixed conductivities in BCY and YDC as a function of temperature and atmospheres, among which BCY behaves bi-ionic conductor both for protons and oxygen ions (Chapter 2). Maximum proton conductivity in BCY10 varies with temperature and atmospheres. For objective of IDEAL-Cell, 3% humidified hydrogen fed could satisfy maximum proton conductivity.

3) Theoretically consideration and simulation of grain boundary effects which are very common in ionic conduction at low temperature ranges and coarsely sintered dense or porous membrane (Chapter 3). Grain boundary effect disappear in BCY or YDC when grain size exceeds 1 μm and working temperature is superior to 600℃.

4) Membrane level modeling on ionic recombination in CM to determine apparent intrinsic kinetic parameter, which is found to be on same order with cathodic reaction at 600℃ (Chapter 4).

5.2. Conclusions within the IDEAL-Cell Project

IDEAL-Cell project originally attempts to design a new way of separating water from electrodes to improve cell efficiency of SOFC. This design can theoretically increase 15-30% potential. However, this design as drawn in Figure 1.5 has a risk of introducing two extra

layers: one electrolyte and one central membrane. The ohmic loss in electrolyte can be solved by fabricating thin layer. However, the challenges from central membrane have been confronted and proved both experimentally and theoretically (Chapter 4), which is specified as ohm loss due to effective ionic conductivity in porous central membrane and extra activation polarization of ionic recombination. Whether the increased potential could be balanced by adding new polarization in CM is the crucial for this project development.

5.3. Advices for Further Modeling Work

Mass transfer: 1) as stated in Chapter 2, proton conductivity in BCY is easy to be influenced by pressure of water. In case of CM where a large amount of water is produced, the relation between water pressures in CM with final proton conductivity in BCY is still required to demonstrate by experiment and model; 2) in composite CM, the oxygen conducting ability of BCY which has been demonstrated in Chapter 2 is not taken into account. If in real operating CM, BCY indeed contribute to oxygen ion conduction, this will lead to a more complicate consideration of effective conductivities and also changes effective TPB lengths current used.

The continuum membrane model applied for kinetic reaction description although has successfully applied in composite electrodes explanation (normally cathode), has its limitation which is based on several basic assumptions and with some adjustable parameters. One of the assumption is concentration gradient of charged species is negligible which is normally valid for thin membrane. As illustrated by current model, reaction is possible to occur through whole CM. This demonstration is probably not correct in case of very thick membrane, which is more suitable to consider a general diffusion-reaction model.

Steady state model generally satisfy the description for V-I characteristic plots which is insufficient to explain oscillation humidity measurements indicating water production is in addition to other factors, also a function of time. In this way, a dynamic model based on study on impedance results is suggested.

Scientific Activities

I have been involved in this IDEAL cell project (European Commission FP7) since the beginning of 2008. My personal scientific experience and knowledge have grown along with research activities in project. Several important aspects are necessary to indicate the processes and reasons of my activities, which are summarized as follows:

- 01/2008-07/2008: Acquainted myself with the background in SOFC and modeling work. Focused modeling work on central membrane which was believed as peculiar feature with regard to convention SOFCs. At same time, studied the modeling tool: COMSOL Multiphysics;
- 09/2008-07/2009: Followed experimental sections in Council National Research (CNR) and Genoa University in Genoa and collected available experimental data to validate in CM and found apparent kinetic reaction rate;
- 2009: Several importance scientific participation in international conferences:
    1) 24/03/2009-27/03/2009: Participation in 6th Symposium on Fuel Cell Modeling and Experimental Validation, Bad Herrenalb/Karlsruhe, Germany
    2) 05/2009-05/2009: Oral Presentation in Icheap 9 conference in Rome, Italy
    3) 04/10/2009-09/10/2009: Poster Presentation in 216th ECS meeting, Vienna, Austria
- 2010: Through two years developments, available experimental data were limited due to many difficulties have been confronted during sample processing. And uncertainties existed in mass transfer phenomenon which is the basis for further modeling. Under this consideration, modeling activities concerning mass transfer in both dense electrolyte and porous CM have been emphasized.
- 06/29/2010-03/07/2010: Oral Presentation in European SOFC forum 2010 in Lucerne, Switzerland

List of Publications

During last three years, two conference papers have been published which are:

i. T. Ou, F. Delloro, C. Nicolella, W. G. Bessler, A. S. Thorel, Mathematical model of mass and charge transport and reaction in the central membrane of the IDEAL-Cell, ECS Transactions, 25(2009)1295-1304

ii. T.Ou, C.Nicolella, F.Delloro, W.Bessler, N.Bundschuh, A.S.Thorel, Mathematical modeling and experimental validation for the proof of concept of IDEAL cell, Proceedings of 9th European Solid Oxide Fuel Cell Forum, 2010, p6-16

And one paper has been collected and will be submitted in weeks:
A simplified approach to analyze mixed conduction in doped cerates at intermediate temperatures (To be submitted)

List of Symbols

Abbreviation	Meaning
ACP	Anion Conducting Phase (Particle)
ASR	Area Specific Resistance
BCY	Yttrium doped Barium Cerate
BCY10	$BaCe_{0.90}Y_{0.10}O_{2.95}$
BCY15	$BaCe_{0.85}Y_{0.15}O_{2.925}$
CM	Central Membrane
CP	Cold Pressing
DC	Direct Current
DIA	Differential Impedance Analysis
DM	Dual Membrane
EIS	Electrochemical Impedance Spectroscopy
FP	Framework Program
HP	Hot Pressing
IDEAL Cell	Innovative Dual mEmbrAne fueL Cell
OCV	Open Circuit Voltage
PCFC	Protonic Conducting Fuel Cell
PCP	Proton Conducting Phase (Particle)
PoC	Proof of Concept
PS	Plasma Spraying
SEM	Scanning Electron Microscopy
SOFC	Solid Oxide Fuel Cell
SPS	Spark Plasma Sintering
TC	Tape Casting
TEM	Transmission Electron Microscopy
TPB	Three Phase Boundary
YDC	Yttrium doped Ceria
YDC15	$Ce_{0.85}Y_{0.15}O_{1.925}$

YSZ	Yttria-Stabilized Zirconia ($Zr_{1-x}Y_xO_{2-\delta}$)	
Symbol	**Meaning**	**Common Units**
a	Specific area	m^{-1}
a	Activity	-
A	Pre-exponential factor	mol m^{-2} s^{-1}
B	Permeability	m^2
C	Nominal mole concentration	-
D	Diffusivity	cm^2 s^{-1}
	Diameter	mm
E_a	Activation energy	kJ mol^{-1}
E	Cell voltage	V
d_P	Particle size	μm
F	Faraday constant	C mol^{-1}
G	Gibbs enthalpy	kJ mol^{-1}
H	Enthalpy	kJ mol^{-1}
k	Rate constant	mol m^{-2} s^{-1}
K	Equilibrium constant	atm^{-n}
k_B	Boltzmann constant	J K^{-1}
i	Current density	A cm^{-2} or mA cm^{-2}
N	Flux	mol cm^{-2} s^{-1}
P	Pressure	Pa or atm
q	Charge	C
R_g	Gas universal constant	J mol^{-1} K^{-1}
R	Resistance	Ω
S	Nominal dopant concentration	-
T	Temperature	K or ℃
t	Transport number	
u	Mobility	cm^2 s^{-1} V^{-1}
x	Depth	cm

Greek symbol	**Meaning**	**Common Units**
α	Transfer coefficient	-
δ	Thickness	m
ε	Porosity	-
Φ	Electrical potential	V
	Volume fraction	-
Δ	Change in parameter	-
∇	Laplace operator	-
∂	Derivative	-
L_{TPB}	TPB length	cm cm^{-3}
η	Overpotential	V
μ	Viscosity	Pa s
	Chemical potential	J mol^{-1}
$\tilde{\mu}$	Electrochemical potential	J mol^{-1}
θ	Surface coverage fraction	-
	Contact angle	-
λ	Kp^{-n}	
δ	Stoichiometric oxygen number	
ρ	Resistivity	Ω cm
σ	Conductivity	S cm^{-1}
τ	Tortuosity	-

Superscript	**Meaning**
o	Initial, boundary
eff	Effective
V	Volume specific
L	Length specific
+	Forward
-	Backward
$'$	Effective

Subscripts	**Meaning**
ACP	Anion Conducting Phase
ADS (ads)	Adsorption
act	Activation
A	Anode
b	Bulk
BCY	BCY15 (see abbreviations)
C	Cathode
cell	Cell
CM (or M)	Central Membrane
e	Electron
eh	Electron plus electron hole
E	Electrolyte
equil	Equilibrium
GAS (gas; g)	Gas
gb	Grain boundaries
H	Hydrogen ion
h	Electron hole
HW	Hydrogen plus water
M	Membrane
MT	Mass Transfer
O	Oxygen ion
OH	Hydroxyl group
OW	Oxygen plus water
P	Particle
sint	Sintering
TPB	Three Phase Boundary
V	Vacancy
w	Water
YDC	YDC15 (see abbreviations)

List of Collaborators

*Beneficiary N°	Beneficiary short name	Country	Beneficiary logo
1(Coordinator)	**ARMINES**	France	
2	**UB**	France	
3	**CNR**	Italy	
4	**DLR**	Germany	
5	**IEES**	Bulgaria	
10	**MT**	France	
7	**NAXAGORAS**	France	
8	**AGH**	Poland	
11	**VISIMBEL**	Germany	

Acknowledgements

Firstly, I am sincerely grateful to my supervisor: Professor Cristiano Nicolella, who gave me this chance to study in this most beautiful country-Italy. During last three years, he has provided me countless helps in every aspect of my scientific activities. Since I have limited experiences in modeling and in field of SOFC, it took me almost one year to be familiar with background and strategies of modeling works. Professor Cristiano Nicolella showed many patience and advices to me when I was frustrated and almost lost my motivations. Another supervisor Professor Nicolaos Vatistas is well experienced in fuel cell and he selfless gave me many valuable explanations and advices for searching a breakthrough when I had bottleneck in research.

Some other colleagues also provided me helps during these three years. They are Ing. Sara Montomoli who helped me to apply COMSOL Multiphysics Software in 2008, Ing. Antonio Bertei from Pisa University, Prof. Antonio Barbucci, Dr. Paola Carpanese from Genoa University, Prof. Massimo Viviani, Dr. Sabrina Presto and Dr. Francesco Delloro from CNR in Genoa who have worked and had constructive discussions during last three years. At last, I also would like to thank Ing. Gabriele Landucci, Ing. Martina Sabatini, Ing. Mina Roudgar. They are doctoral students who used to work in same office with me. We had a good time working together.

I am sure that I will miss this period of stay not only because impressive experience in scientific researches but also because this lovely country and lovely persons I met in Italy.